

D^0 PRODUCTION RATE MEASUREMENT IN NEUTRINO INTERACTIONS
AND A LIMIT ON MUON NEUTRINO TO TAU NEUTRINO OSCILLATIONS

A THESIS SUBMITTED TO
THE GRADUATE SCHOOL OF NATURAL AND APPLIED SCIENCES
OF
THE MIDDLE EAST TECHNICAL UNIVERSITY

BY

ALİ MURAT GÜLER

IN PARTIAL FULFILLMENT OF THE REQUIREMENTS FOR THE DEGREE OF
DOCTOR OF PHILOSOPHY
IN
THE DEPARTMENT OF PHYSICS

OCTOBER 2000

CERN-THESIS-2002-027
24/10/2000



ABSTRACT

D^0 PRODUCTION RATE MEASUREMENT IN NEUTRINO INTERACTIONS AND A LIMIT ON MUON NEUTRINO TO TAU NEUTRINO OSCILLATIONS

Güler, Ali Murat

Ph.D., Department of Physics

Supervisor: Prof. Dr. Perihan Tolun

October 2000, 134 pages.

The CHORUS experiment was designed to search for $\nu_\mu \rightarrow \nu_\tau$ oscillation. Recently Phase I analysis has been completed and no τ^- candidate is found. We have participated in the Phase I analysis, doing the analysis of 2043 1μ and 352 0μ events in Ankara. Using the eye-checked sample, a limit on $\nu_\mu \rightarrow \nu_\tau$ oscillation probability is extracted; $P_{\nu_\mu\nu_\tau} < 1.14 \times 10^{-2}$ at 90 % C.L. and large Δm^2 . The second phase of the CHORUS analysis was recently started with new scanning systems. The big improvements in the scanning system and methods allow the CHORUS experiment to study also charm physics with large statistics. In this work, D^0 production rate in neutrino interactions has been evaluated using 122 D^0 candidates found in 8028 located ν_μ charged-current interactions in the collaboration, as:

$$\frac{\sigma(\nu_\mu N \rightarrow D^0 \mu^- X)}{\sigma(\nu_\mu N \rightarrow \mu^- X)} = 1.998 \pm 0.223\%$$

The achieved precision of the production rate exceeds that of the previous experiments.

Keywords: Neutrino, Neutrino mass, Neutrino oscillations, Production rates, Oscillation limits

ÖZ

NÖTRİNO ETKİLEŞİMLERİNDEKİ D^0 ÜRETİM ORANININ ÖLÇÜLMESİ VE MUON NÖTRİNONUN TAU NÖTRİNOYA SALINIMININ LİMİTİ

Güler, Ali Murat

Doktora , Fizik Bölümü

Tez Yöneticisi: Prof. Dr. Perihan Tolun

Ekim 2000, 134 sayfa.

CHORUS deneyi $\nu_\mu \rightarrow \nu_\tau$ salınımlarını araştırmak için planlanmıştır. İlk aşama analizi tamamlanmış ve $\nu_\mu \rightarrow \nu_\tau$ salınımı gözlenememiştir. İlk aşama analizinde 2043 1μ and 352 0μ olay Ankara' da analiz edilmiştir. Analiz edilen olaylar kullanılarak salınım olasılığının limiti $P_{\nu_\mu\nu_\tau} < 1.14 \times 10^{-2}$ (90 % C.L ve büyük Δm^2 ' de) olarak hesaplanmıştır. İkinci aşama analizi yeni tarama sistemi ile başlatılmıştır. Tarama sistemindeki önemli gelişmelerden dolayı CHORUS deneyinde charm analizi daha büyük istatistikle yapılabilir hale gelmiştir. Bu çalışmada, nötrino üretim oranı 122 tane D^0 adayı kullanılarak ölçülmüştür:

$$\frac{\sigma(\nu_\mu N \rightarrow D^0 \mu^- X)}{\sigma(\nu_\mu N \rightarrow \mu^- X)} = 1.998 \pm 0.223\%$$

Ölçülen üretim oranı daha önceki deneylerde bulunan üretim oranlarından daha hassastır.

Anahtar Sözcükler: Nötrino, Nötrino kütlesi, Nötrino salınımı, Üretim oranı, Salınım limiti

ACKNOWLEDGMENTS

I am grateful to my supervisor Prof. Dr. Perihan Tolun for giving me opportunity to participate High Energy Physics and for motivation and constant support.

I would like to express my gratitude to Prof. Dr. Kimio Niwa for giving me opportunity to work at F-lab and for his valuable guidance and support.

My special thanks go to Osamu Sato for many sparkling ideas, discussions and his interest in my work.

I would like to specially thank to Masahiro Komatsu and Yoshihisa Obayashi for stimulating discussions and their help.

Many thanks go to Tülün Ergin for a nice cooperation and useful tips while writing the text.

I would like to thank also Gazi Menteş for giving me technical help during the manual check of module 68B in Ankara.

Many great thanks go to my family specially my sisters: Derya and Zehra for their outstanding support and understanding.

Finally, I would like to thank TÜBİTAK for giving me a scholarship (BDP) to work on the CHORUS experiment.

TABLE OF CONTENTS

ABSTRACT	iii
ÖZ	v
ACKNOWLEDGMENTS	vi
TABLE OF CONTENTS	vii
CHAPTER	
1 INTRODUCTION	1
2 PHENOMENOLOGY OF NEUTRINO INTERACTIONS	4
2.1 Standard Model	4
2.2 Quantum Chromodynamics	7
2.3 Higgs Mechanism	9
2.4 Neutrino Mass	12
2.4.1 Dirac Mass Term	13
2.4.2 Majorana Mass Term	14
2.5 Neutrino Oscillations	16
2.5.1 Two Flavour Oscillation	18
2.5.2 Neutrino Oscillations Experiments	18
2.6 Evidence for Neutrino Oscillations	19
2.6.1 LSND Experiment	19
2.6.2 Atmospheric Neutrino Experiments	20
2.7 Neutrino Charged Current Interaction	22
2.7.1 Parton Model	23
2.7.2 Charm Production by Neutrino Charged Current Interaction	24

3	THE EXPERIMENTAL APPARATUS	26
3.1	Emulsion Target	26
3.1.1	Nicon Microscope	28
3.2	Target Tracker	32
3.3	Hadron Spectrometer	32
3.4	Calorimeter	33
3.5	Muon Spectrometer	34
3.6	Trigger	34
3.7	Neutrino Beam	35
4	THE $\nu_\mu \rightarrow \nu_\tau$ OSCILLATION SEARCH ANALYSIS	37
4.1	CHORUS Phase I Analysis	37
4.2	Event Selection	37
4.2.1	Selection Criteria for 1μ Sample	39
4.2.2	Selection Criteria for 0μ Sample	40
4.2.3	Selection Criteria for 2μ Sample	40
4.3	Emulsion Scanning	43
4.3.1	Changeable Sheet Scanning	43
4.3.2	Special Sheet Scanning	44
4.3.3	Vertex Location	44
4.3.4	Decay Search	45
4.3.5	Method I	46
4.3.6	Method II	46
4.3.7	Method III	46
4.3.8	Method IV	47
4.4	Decay Confirmation	48
4.5	Emulsion Scanning in Ankara	51
4.5.1	Monte Carlo Simulation	59
4.5.2	Reconstruction Efficiency $1\mu^-$ Events	60
4.5.3	Reconstruction Efficiency $0\mu^-$ Events	61
4.5.4	Scanning Efficiency	62
4.6	Kink Finding Efficiency	65

4.7	Computation of Δm^2 Dependence of $\sin^2 2\theta$	67
4.7.1	Systematic Errors	69
4.8	Background Sources	70
4.9	A Limit on $\nu_\mu \rightarrow \nu_\tau$ Oscillation	71
5	D^0 PRODUCTION RATE MEASUREMENT IN NEUTRINO INTERACTIONS	75
5.1	CHORUS Phase II Analysis	75
5.2	Net Scanning	76
5.2.1	Alignment and Tracking	77
5.2.2	Fine Alignment and Vertex Reconstruction	77
5.2.2.1	Fine Alignment	77
5.2.2.2	Vertex Reconstruction	79
5.2.3	Selection for Charm Search	80
5.2.3.1	Selection A	80
5.2.3.2	Selection B	82
5.3	Manual Check and Results	85
5.4	Final Sample	90
5.5	MC Simulation	91
5.5.1	The MC Sample	91
5.5.2	Net Scanning Efficiency Estimation	92
5.6	Background Estimation	94
5.6.1	Electron-pair Check	94
5.6.2	Background Due to K_s^0 and Λ Decay	95
5.7	Systematic Errors	99
5.8	D^0 Production Rates	99
5.9	Dimuon Production Rate	100
5.10	Comparison with E531 Experiment	100
6	CONCLUSION AND SUMMARY OF ANALYSIS	115
	REFERENCES	116

APPENDICES	121
A INTERESTING EVENTS FOUND IN ANKARA	121
A.1 Event 15764430	121
A.2 Event 16553623	122
A.3 Event 20401968	122
A.4 Event 27913325	123
A.5 Event 33800256	124
A.6 Event 34081069	125
A.7 Event 34361592	125

LIST OF TABLES

2.1	Weak Isospin and Hypercharge quantum numbers for leptons and quarks in the Standard Electroweak Model	8
2.2	Basic Standard Model parameters measured at LEP and SLC [18].	12
2.3	Charmed hadron properties [75].	25
3.1	Emulsion experiments in which semi-automatic or automatic scanning was used	29
3.2	Steps in the development of Track Selector systems. The scanning speed expressed in view per second (a view corresponding to an area of $\sim 0.018 \text{ mm}^2$) [49]	32
3.3	Relative composition of CHORUS neutrino beam.	35
3.4	The composition of CHORUS Fuji ET-7B emulsion	36
3.5	Decay modes producing neutrino beam.	36
4.1	Data flow chart	49
4.2	Scanning results of modules 28b, 28t (1994 data)	53
4.3	Scanning results of modules 68b, 68t (1995 data)	53
4.4	Track finding efficiencies.	54
4.5	Reconstruction efficiency of 1μ events.	61
4.6	Reconstruction efficiency of 0μ events.	62
4.7	Scanning efficiency of 1μ events.	63
4.8	Scanning efficiency of 0μ events.	63
4.9	Kink finding efficiencies	67
4.10	Estimated acceptance and kink finding efficiency for each decay mode	71
4.11	Quantities used in estimation of limit on oscillation probability .	72
5.1	Runcard parameters of "ecvtxa"	80
5.2	Data set 96	89
5.3	Data set 97	89
5.4	Found charm candidates	90

5.5	D^0 sample used in analysis.	90
5.6	MC charm sample	92
5.7	Applied cuts	92
5.8	Applied cuts for dimuon charm events.	101
5.9	Found charmed particles in E531 experiment [57]	101
A.1	Kink decay Topology of K^+, π^+ and D^+ and corresponding Branching ratios and maximum transverse momentum.	126

LIST OF FIGURES

2.1	Diagram shows neutrino D.I.S. interaction with nucleon.	23
2.2	Charmed hadron production by neutrino charge current (left) and neutral current (right) interactions.	24
3.1	Schematic diagram of CHORUS detector	27
3.2	Schematic diagram of CHORUS target: Bulk emulsion, interface sheets and fiber tracker	28
3.3	Automatic track recognition hardware.	30
3.4	Track selector efficiency.	30
3.5	Block diagram of Nikon microscope equipped with TS2.	31
3.6	Neutrino beam energy spectrum	34
4.1	Top: decay topology of τ lepton, Bottom: flight length and kink angle of τ lepton from MC simulation.	38
4.2	Applied momentum cut to the 1μ sample.	40
4.3	Event reconstructed as 0μ (Top), 1μ (Middle) and 2μ (Bottom) in the electronic detectors	41
4.4	We have seen mainly, ν_μ CC or ν_μ NC interaction in emulsion	42
4.5	Event location	45
4.6	Parent search	47
4.7	Kink angles above the line can be detected by eye.	48
4.8	Decay types: a) short large type, b) Long Large type, c) Long small type.	50
4.9	The analyzed modules in Ankara is 28B, 28T, 68B, 68T as shown in Figure.	52
4.10	Top: measured-predicted CS angle in y and z. Bottom: measured-predicted CS angle in y and z (scanned in Ankara)	55
4.11	Top: measured-predicted CS angle in y and z. Bottom: measured-predicted CS angle in y and z (scanned in Nagoya Laboratory)	56
4.12	Top: measured-predicted SS angle in y and z. Bottom: measured-predicted SS angle in y and z (scanned in Nagoya Laboratory)	57

4.13	Plots show location efficiency versus SB momentum, top: 1μ sample, bottom: 0μ sample.	58
4.14	Vertex position in the emulsion target from MC simulation.	64
4.15	Angle difference between MC truth and TT reconstructed track for 1μ (top) and 0μ (bottom) events.	66
4.16	Limit on $\nu_\mu \rightarrow \nu_\tau$ obtained using data scanned in Ankara (right) (we would get the limit (most left) if all data were analyzed in the same way as in Ankara)	73
4.17	Present limit of CHORUS on $\nu_\mu \rightarrow \nu_\tau$ oscillation	74
5.1	Residuals RMS distribution in position y and z	78
5.2	Residuals RMS distribution in slope y and z	79
5.3	Fiducial volume for Net Scanning	81
5.4	e-pair cut: $\Delta\theta > 10\text{mrad}$	82
5.5	Global angle difference of 2-segment (Top) and 3-segment (Bottom) tracks	83
5.6	TT angle difference of 2-segment (Top) and 3-segment (Bottom) tracks	84
5.7	Top: minimum distance between muon track and other tracks versus vertex depth, bottom: minimum distance between muon track and other tracks.	85
5.8	a)Number of tracks after first level alignment and tracking. b) Number of tracks which stop in fiducial volume (at least 2-segment connected) after low-momentum rejection.	86
5.9	a)Number of TT track. b) Number of tracks that stops in fiducial volume and reconstructed at TT and pass the global angle cut	87
5.10	Top: All tracks in fiducial volume, bottom: after rejecting passing through and low momentum particles we get "Vee" event	88
5.11	The scanned modules for D^0 production rate measurement.	91
5.12	Co-planality ckeck.	95
5.13	Scatter plot of e-pair transverse momenta from MC.	96
5.14	Top: e-pair conversion length and opening angle distribution from MC, bottom: K^0 flight length and opening angle distribution from MC.	97
5.15	Top: ϕ angle vs. dip angle (explained in tex) for K^0 from MC simulation, bottom: same distribution for D^0 candidates.	98

5.16	Comparison between distributions from data (point) and MC simulation (histogram) for located CC ν_μ events.	102
5.17	Top: DATA/MC ratio for located events without E_{cal} cut, bottom: with $E_{cal} > 4GeV$ cut	103
5.18	Top: $(correction\ factor)^{-1}$ for "Vee" and "4Vee" bottom: production rate for Vee and 4Vee events.	104
5.19	D^0 production rate in ν_μ CC interaction.	105
5.20	Dimuon production rate	106
5.21	D^0 production rate in ν_μ CC interaction from E531 experiment.	107
5.22	Bjorken x dependence of D^0 production rate.	108
5.23	Bjorken y dependence of D^0 production rate.	109
5.24	Q^2 dependence of D^0 production rate.	110
5.25	Comparison between distributions from the simulation (histograms) and the data (points) for D^0 events top: visible energy, bottom: momentum transfer.	111
5.26	Comparison between distributions from the simulation (histograms) and the data (points) for D^0 events top: Bjorken x , bottom: Bjorken y.	112
5.27	Comparison between distributions from the simulation (histograms) and the data (points) for D^0 events top: flight length , bottom: opening angle.	113
5.28	Comparison of the number of shower tracks at primary vertex, simulation (histograms) and the data (points) for D^0 events.	114
A.1	Event 15764430, Kink Topology	127
A.2	Event 16553623, 4Vee Topology	128
A.3	Event 20401968, Vee Topology	129
A.4	Event 27913325, Kink Topology	130
A.5	Event 33800256, Trident Topology	131
A.6	Event 34081069, Trident Topology	132
A.7	Event 34361069, Kink Topology	133

CHAPTER 1

INTRODUCTION

Neutrinos and their interactions are of great interest in theoretical and experimental particle physics, resulting in many theoretical models and experiments in order to resolve their properties.

The discovery of radioactivity by H. Becquerel in 1886 constitutes the first experimental manifestation of weak interaction phenomena.

The physics of neutrinos [1-8] began with the studies of radioactivity and the problematic spectrum of beta decay. In 1914 Chadwick discovered that the beta ray spectra is continuous rather than unique. The observed electrons had different energies and decay products did not emerge back to back as expected in a two-body decay. Therefore, it seemed that energy and momentum were not conserved in that process. To explain this observation, W. Pauli proposed a neutral massless particle of spin half. Later it was called "neutrino".

In 1933 E. Fermi developed his theory of beta decay [14] using the neutrino, electron, neutron and proton. A new field of theoretical physics came into existence -the field of weak interactions. In analogy to quantum electrodynamics he wrote down an interaction Lagrangian for the beta decay

$$L_f = -\frac{G_f}{2^{1/2}} \bar{\psi}_p \gamma^\mu \psi_n \bar{\psi}_e \gamma_\mu \psi_\nu \quad (1.1)$$

where G_f is a coupling constant. In 1934, Bethe and Peierls using Fermi's theory, calculated the cross section of inverse beta decay. They found that the cross section for a few MeV $\bar{\nu}_e$ was about 10^{-43}cm^2 . In order to detect such a rare process with this low cross-section, both a large target and an enormous flux was required. It was realized the nuclear reactors might provide a flux sufficient to override the background.

In 1953, F. Reines and C. Cowan [30] detected neutrinos experimentally for the first time from the Savannah River nuclear reactor.

In 1947, with the discovery of the pion by C.F. Powell, it was found that nuclear beta decay is not the only source of neutrinos. The related weak decays of pions and kaons also produce neutrinos. A question naturally arose whether this ν_μ was identical as ν_e . In 1962, L. Lederman, J. Steinberger and M. Schwarz [15] showed using the Brookhaven AGS accelerator that these ν_μ did not interact to produce e^- as did ν_e but rather the reaction observed was $\nu_\mu n \rightarrow p\mu^-$.

In 1975, M. Perl [16] at the Stanford Linear Accelerator Center (SLAC) discovered τ^- lepton, for which he shared the 1995 Nobel prize with F. Reines. Recently, the neutrino associated with the τ^- lepton, has been observed in the DONUT (Fermilab E872) experiment [71] which was designed to detect ν_τ charge current (CC) interactions. The ν_τ beam is obtained by the interaction of the 800 GeV proton beam on a tungsten dump, producing D_s which decay into $\tau\nu_\tau$. The main principle of analysis is to detect ν_τ CC interactions and subsequent decay of τ lepton in the ECC (Emulsion Cloud Chamber). After this observation, it can be now said that all the leptons and quarks predicted by the Standard Model (which describes the properties and interactions of all particles in nature) have been observed experimentally.

In the Standard Model neutrinos are treated as massless, neutral, left-handed particles with spin half. The possibility of non-zero mass for neutrinos is one of the challenging question of particle physics. A massive neutrino implies physics beyond the Standard Model. If the neutrinos are massive several phenomena can occur such as mixing between different eigenstates. As a consequence of mixing, a massive neutrino may be seen as a different eigenstates at some distance from source. This phenomenon is called neutrino oscillation, was introduced by B. Pontecorvo. Many experiments are performed in order to detect neutrino oscillations. One of them is the CHORUS experiment which was designed to search for $\nu_\mu \rightarrow \nu_\tau$. In chapter 4 the analysis method implemented in the CHORUS

experiment will be presented and using the analyzed events in Ankara, a limit on the $\nu_\mu \rightarrow \nu_\tau$ oscillation will be extracted.

The other interesting subject to study in CHORUS is charm production by neutrino interactions. Due to its mass, charm quark is of special interest for theories. For chiral symmetry methods its mass scale is too large. On the other hand, its mass may be not large enough for heavy quark effective theory. Therefore a measurement of charm production in neutrino interactions provides a test for perturbative QCD (Quantum Chromodynamics) which describes the strong interactions between the particles as a part of the Standard Model. Several experiments have been done in the past to study charmed particle production such as E531[57], CDHS[53], CHARM II[69] and CCFR [52]. After the great improvement in scanning systems, the CHORUS experiment has provided high statistics for the charm study. In this work using largest statistics in the world at present, D^0 production rate measurement has been done. In chapter 5, this analysis will be presented.

In the following chapter, the theoretical background relevant to analysis which follows will be summarized.

CHAPTER 2

PHENOMENOLOGY OF NEUTRINO INTERACTIONS

Standard Model [6, 10, 17, 18] which describes interactions among elementary particles within the framework of gauge theories with symmetry group $SU(3)_c \times SU(2)_L \times U(1)_Y$ is widely accepted among high energy physicists. Its predictions are in agreement with all experimental observations up to currently available energies of about one TeV.

In the theory of elementary particles the dynamics of free and interacting particles are described in terms of the Lagrangian density. Calculations of physical observables are expressed as a perturbation expansion in increasing numbers of point like couplings and are represented by Feynman diagrams. Every vertex contributes an interaction coupling constant to the corresponding term in the series. In the Standard Model all elementary particles are arranged in discrete multiplets of the symmetry groups representing the symmetries of the interactions involved. The central principle of the Standard Model is the invariance of the Lagrangian density under gauge transformations which will be discussed in the following section.

2.1 Standard Model

The fundamental interactions among particles considered in Standard Model (S.M.) are the Strong the Electromagnetic, the weak interactions.

S. Glashow [19], A. Salam [20] and S. Weinberg [21] unified weak and electromagnetic interactions: they are introduced as different components of single gauge theory. The underlying gauge transformations are those of the direct

product

$$SU(2)_L \times U(1)_Y$$

where $SU(2)_L$ is the group of weak-isospin and $U_Y(1)$ is the group of hypercharge transformations. Under this local gauge transformation group, fermions transform as left-handed doublets and right-handed singlets.

$$\begin{pmatrix} e^- \\ \nu_e \end{pmatrix}_L e_{\bar{R}}, \quad \begin{pmatrix} \mu^- \\ \nu_\mu \end{pmatrix}_L \mu_{\bar{R}}, \quad \begin{pmatrix} \tau^- \\ \nu_\tau \end{pmatrix}_L \tau_{\bar{R}}$$

$$\begin{pmatrix} u \\ d \end{pmatrix}_L u_R, d_R, \quad \begin{pmatrix} c \\ s \end{pmatrix}_L c_R, s_R, \quad \begin{pmatrix} t \\ b \end{pmatrix}_L t_R, b_R.$$

Minimal Standard Model Lagrangian consist of 4 sectors, $\mathcal{L} = \mathcal{L}^I + \mathcal{L}^{II} + \mathcal{L}^{III} + \mathcal{L}^{IV}$

- $\mathcal{L}^I = -\frac{1}{4}W_{\mu\nu}W^{\mu\nu} - \frac{1}{4}Z_{\mu\nu}Z^{\mu\nu}$ where $W_{\mu\nu} = \partial_\mu \vec{A}_\nu - \partial_\nu \vec{A}_\mu - g \vec{A}_\mu \times \vec{A}_\nu$, $Z_{\mu\nu} = \partial_\mu B_\nu - \partial_\nu B_\mu$ with A_μ^i and B_μ being massless gauge bosons. This sector is the kinetic term and corresponds to self coupling of weak bosons.
- $\mathcal{L}^{II} = \frac{-g}{2\sqrt{2}}(J_\mu W^\mu + J_\mu^\dagger W^{\dagger\mu}) - \frac{g}{2\cos\theta_w}J_\mu^0 Z^\mu - eJ_\mu^{em}A^\mu$

where θ_w is the Glashow - Weinberg mixing angle defined as $\tan\theta_w = \frac{g'}{g}$ and Z^μ, W^μ, A^μ are the physical fields and related with gauge bosons through the following equations:

$$W^\mu = \frac{A^{1\mu} + iA^{2\mu}}{\sqrt{2}}$$

$$Z^\mu = A^{3\mu}\cos\theta_w - B^\mu\sin\theta_w$$

$$A^\mu = A^{3\mu}\sin\theta_w + B^\mu\cos\theta_w$$

and J_μ is the lepton and quark interaction current probability density associated with the weak and electromagnetic components of the interaction:

$$J_\mu^0 = \frac{1}{2}(\bar{\nu}_e\gamma_\mu(1 + \gamma_5)\nu_e + \bar{\nu}_\mu\gamma_\mu(1 + \gamma_5)\nu_\mu + \bar{\nu}_\tau\gamma_\mu(1 + \gamma_5)\nu_\tau +$$

$$\begin{aligned}
& \bar{u}\gamma_\mu(1 + \gamma_5)u + \bar{c}\gamma_\mu(1 + \gamma_5)c + \bar{t}\gamma_\mu(1 + \gamma_5)t \\
& - \frac{1}{2}(\bar{e}\gamma_\mu(1 + \gamma_5)e + \bar{\mu}\gamma_\mu(1 + \gamma_5)\mu + \bar{\tau}\gamma_\mu(1 + \gamma_5)\tau) + \\
& \bar{d}\gamma_\mu(1 + \gamma_5)d + \bar{s}\gamma_\mu(1 + \gamma_5)s + \bar{b}\gamma_\mu(1 + \gamma_5)b) + 2\sin^2\theta_w J_\mu^{em}
\end{aligned}$$

$$\begin{aligned}
J_\mu^{em} &= \bar{e}\gamma_\mu e + \bar{\mu}\gamma_\mu\mu + \bar{\tau}\gamma_\mu\tau - \frac{2}{3}(\bar{u}\gamma_\mu u + \bar{c}\gamma_\mu c + \bar{t}\gamma_\mu t) \\
&+ \frac{1}{3}(\bar{d}\gamma_\mu d + \bar{s}\gamma_\mu s + \bar{b}\gamma_\mu b) \\
J_\mu &= \bar{e}\gamma_\mu(1 + \gamma_5)\nu_e + \bar{\mu}\gamma_\mu(1 + \gamma_5)\nu_\mu + \bar{\tau}\gamma_\mu(1 + \gamma_5)\nu_\tau + \\
&\bar{d}'\gamma_\mu(1 + \gamma_5)u + \bar{s}'\gamma_\mu(1 + \gamma_5)c + \bar{b}'\gamma_\mu(1 + \gamma_5)t
\end{aligned}$$

Here, d', s', b' which are the weak eigenstates of quarks, are expressed as a linear combination of the quark mass eigenstates via the 3×3 unitary CKM (Cabbibo-Kobayashi-Maskawa) mixing matrix given below.

$$\begin{pmatrix} d' \\ s' \\ b' \end{pmatrix} = \begin{pmatrix} c_1 & -s_1 c_3 & -s_1 s_3 \\ s_1 c_2 & c_1 c_2 c_3 - s_2 s_3 e^{i\delta} & c_1 c_2 s_3 + s_2 s_3 e^{i\delta} \\ s_1 s_2 & c_1 s_2 c_3 + c_2 s_3 e^{i\delta} & c_1 s_2 s_3 - c_2 c_3 e^{i\delta} \end{pmatrix} \begin{pmatrix} d \\ s \\ b \end{pmatrix}. \quad (2.1)$$

Here we have $s_i = \sin\theta_i$, $c_i = \cos\theta_i$ where θ_i are mixing angles, δ is the phase which describes CP violation. This sector describes the interaction of fundamental fermions and vector bosons i.e. the weak interactions of fermions and also the electromagnetic interactions of fermions. In order to obtain \mathcal{L}^{II} one should make the following substitutions in the free Lagrangian of fermion fields, $\mathcal{L} = \bar{\psi}(i\gamma_\mu\partial^\mu + m)\psi$.

$$\partial_\mu\psi \rightarrow D_\mu\psi = \begin{cases} \partial_\mu\psi_L + ig\frac{1}{2}\tau^i A_\mu^i\psi_L + ig'\frac{1}{2}Y B_\mu\psi_L \\ \partial_\mu\psi_R + i\frac{1}{2}g'Y B_\mu\psi_R \end{cases} \quad (2.2)$$

and in the corresponding expressions for Dirac conjugated spinors. Here, A_μ and B_μ are the gauge fields associated with the local gauge symmetry groups, $SU(2)_L \times U(1)_Y$, g and g' (it is required that $e = \frac{gg'}{\sqrt{(g')^2 + g^2}}$) are coupling constants

and Y is the hypercharge (as shown in Table (2.1)) which is chosen in such a way that Gell-Mann and Nishijima relation, $Q = T^3 + \frac{Y}{2}$ is satisfied. The left-handed (LH) and the right-handed (RH) components of ψ transform under the local gauge group $SU(2)_L \times U(1)_Y$ as

$$\begin{aligned}\psi'_L &= e^{i\vec{\alpha}(x) \cdot \vec{T} + i\beta(x)Y} \psi_L \\ \psi'_R &= e^{i\beta(x)Y} \psi_R\end{aligned}\tag{2.3}$$

and gauge fields transform as

$$\begin{aligned}\vec{A}'_\mu(x) &= \vec{A}_\mu(x) - \frac{1}{g}\partial_\mu \vec{\alpha}(x) - \vec{\alpha}(x) \times \vec{A}_\mu(x) \\ B'_\mu(x) &= B_\mu(x) - \frac{1}{g'}\partial_\mu \beta(x)\end{aligned}\tag{2.4}$$

Under these transformations, which are local $SU(2)_L \times U(1)_Y$ transformation for massless fields, the expression in sector II is invariant.

The sectors III and IV which give the masses of the bosons and fermions and their coupling to Higgs fields are

- $\mathcal{L}^{III} = |(\partial_\mu + \frac{1}{2}ig\tau^i A_\mu^i + i\frac{1}{2}g'Y B_\mu)\phi|^2 - V(\phi)$
- $\mathcal{L}^{IV} = -(G_f \bar{f}_L f_R + G'_f \bar{f}_L f_R + h.c.)$ where the f are the fundamental fermion fields and G_f and G'_f are the coupling constants.

2.2 Quantum Chromodynamics

Quantum Chromodynamics (QCD) which describes the strong interactions of quarks and gluons is another part of the Standard Model.

In strong interaction, experiments confirm that each quark has another internal degree of freedom with a corresponding quantum number called colour which can take three different values. Transition between different colour states of quarks are generated by eight coloured gluons and described by transformations belonging to the $SU(3)$ group.

Table 2.1: Weak Isospin and Hypercharge quantum numbers for leptons and quarks in the Standard Electroweak Model

Fermions	T	T ³	Y	Q
ν_e, ν_μ, ν_τ	1/2	1/2	-1	0
e_L, μ_L, τ_L	1/2	-1/2	-1	-1
e_R, μ_R, τ_R	0	0	-2	-1
u_L, c_L, t_L	1/2	1/2	1/3	2/3
d_L, c_L, b_L	1/2	-1/2	1/3	-1/3
u_R, c_R, t_R	0	0	4/3	2/3
d_R, c_R, b_R	0	0	-2/3	-1/3

The QCD Lagrangian is given by

$$\mathcal{L} = -\frac{1}{4}F_{\mu\nu}^{(a)}F^{(a)\mu\nu} + \sum_q \bar{\psi}_i^q (i\gamma^\mu (D_\mu)_{ij} - m_q \delta_{ij}) \psi_j^q$$

with $F_{\mu\nu}^a = \partial_\mu A_\nu^a - \partial_\nu A_\mu^a + g_s f_{abc} A_\mu^b A_\nu^c$

and $(D_\mu)_{ij} = \delta_{ij} \partial_\mu - ig_s T_{ij}^a A_\mu^a$

where g_s is QCD coupling constant, T_{ij}^a and f_{abc} are the $SU(3)_c$ colour matrices and structure constants respectively, the $\psi_i^q(x)$ are the 4 component Dirac spinors associated with each quark field of colour i and flavour q . A_μ^a are the eight Yang-Mills gluon fields. The matrices T^a form a complete basis of traceless 3×3 matrices and f_{abc} is defined by

$$[T^a, T^b] = if^{abc}T^c \tag{2.5}$$

The QCD Lagrangian is very similar to the Quantum electrodynamics (QED) Lagrangian. The most apparent difference is due to the fact that fermions carry a new quantum number, colour. Also gluons carry colour related to their quantum numbers. Unlike the case of QED the gluons are charged, and can emit other gluons. The consequences of this fact leads to two important properties of the QCD, namely the confinement and the asymptotic freedom of quarks. It is found that the effective coupling constant goes to zero as the separation becomes very

small. This behaviour is known as asymptotic freedom. This is why the quarks and gluons seem to be interacting weakly at short distances probed in hard collisions. Confinement means that quarks do not exist as isolated single particles but they exist only in bound systems which form colour singlet.

2.3 Higgs Mechanism

The $SU(2)_L \times U(1)_Y$ gauge invariance can be exact only in the case when the masses of all particles are equal to zero. Any mass term in the Lagrangian would violate the gauge invariance of the theory. The Standard Model of the electroweak interaction is based on the assumption that $SU(2)_L \times U(1)_Y$ gauge invariance is broken spontaneously via Higgs mechanism [6, 22, 17, 18] through which masses are introduced.

In order to break $SU(2)_L \times U(1)_Y$ to $U(1)_{EM}$ we assume the universe is filled with a spin zero field, called a Higgs field; it is introduced as an isodoublet and described by the Lagrangian

$$\begin{aligned}\mathcal{L}_H &= (\partial_\mu \phi^\dagger)(\partial^\mu \phi) - V(\phi) \\ V(\phi) &= -\mu^2 \phi^\dagger \phi + \lambda(\phi^\dagger \phi)^2\end{aligned}\tag{2.6}$$

where $\mu^2 > 0$, $\lambda > 0$ and

$$\phi = \begin{pmatrix} \phi_+ \\ \phi_0 \end{pmatrix}, \quad Y = 1$$

Here, ϕ_+ and ϕ_0 are complex fields,

$$\phi_+ = \frac{\phi_1 + i\phi_2}{\sqrt{2}}, \quad \phi_0 = \frac{\phi_3 + i\phi_4}{\sqrt{2}}\tag{2.7}$$

In order to maintain the gauge invariance the following substitution should be made in Eq.(2.6)

$$\partial_\mu \rightarrow D_\mu = \partial_\mu + i\frac{g}{2}\vec{\tau} \cdot \vec{A}_\mu + i\frac{g'}{2}B_\mu\tag{2.8}$$

After this substitution Eq.(2.6) becomes

$$\mathcal{L}_H = |(\partial_\mu + \frac{1}{2}ig\tau^i A_\mu^i + i\frac{1}{2}g'Y B_\mu)\phi|^2 - V(\phi) \quad (2.9)$$

Thus, the total $SU(2)_L \times U(1)_Y$ invariant Lagrangian is

$$\mathcal{L} = \mathcal{L}^I + \mathcal{L}^{II} + \mathcal{L}_H \quad (2.10)$$

where \mathcal{L}^I and \mathcal{L}^{II} are the kinetic and the interaction parts of S.M. Lagrangian. \mathcal{L} still describes a hypothetical world with massless fermions and gauge bosons and self-interacting scalar fields with mass μ . $SU(2)_L \times U(1)_Y$ symmetry can be broken in such way that $U(1)_{em}$ remains an exact symmetry of nature. This can be accomplished by giving a vacuum expectation value (VEV) to ϕ . The potential $V(\phi)$ has a minimum at

$$(\phi^\dagger \phi) = -\frac{\mu^2}{2\lambda} \equiv \frac{v^2}{2} \quad (2.11)$$

which is a circle on the complex ϕ plane. We choose a point on this circle, to be the ground state. This corresponds to replacing ϕ by

$$\phi \rightarrow \phi = \frac{1}{\sqrt{2}} \begin{pmatrix} 0 \\ v + H \end{pmatrix} \quad (2.12)$$

where H is scalar real field and v is the vacuum expectation value. The new ϕ has non-vanishing VEV

$$\phi_0 = \frac{1}{\sqrt{2}} \begin{pmatrix} 0 \\ v \end{pmatrix}. \quad (2.13)$$

We can write ϕ as

$$\phi \rightarrow \phi = \frac{1}{\sqrt{2}} \begin{pmatrix} 0 \\ v + H \end{pmatrix} = \frac{v + H}{\sqrt{2}} \chi_-, \quad \chi_- = \begin{pmatrix} 0 \\ 1 \end{pmatrix} \quad (2.14)$$

for convenience. Substituting Eq.(2.14) into Eq.(2.9) and setting $Y=1$ and finally using the explicit form of $\vec{\tau}$ matrices we obtain

$$L_H = \frac{1}{2} \partial_\mu H \partial^\mu H + \frac{(v + H)^2}{8} \chi_-^\dagger [(g' B_\mu - g A_\mu^3)(g' B^\mu - g A^{3\mu}) + g^2 (A_\mu^1)^2 + g^2 (A_\mu^2)^2] \chi_- - V\left(\left(\frac{v + H}{2}\right)^2\right)$$

The relevant term which is responsible for the generation of W^\pm , Z^0 and H masses is

$$\frac{1}{8}v^2[(g'B_\mu - gA_\mu^3)(g'B^\mu - gA^{3\mu}) + g^2(A_\mu^1)^2 + g^2(A_\mu^2)^2] - \lambda v^2 H^2 \quad (2.15)$$

Using the definitions,

$$W_\mu^\pm = \frac{(A_\mu^1 \pm iA_\mu^2)}{\sqrt{2}}, \quad Z_\mu = \frac{-gA_\mu^3 + g'B_\mu}{\sqrt{g^2 + g'^2}} \quad (2.16)$$

we can rewrite Eq.(2.15) as

$$\frac{v^2}{2}[\frac{1}{4}2g^2W^{+\mu}W_\mu^- + \frac{1}{4}(g^2 + g'^2)Z^\mu Z_\mu] - \lambda v^2 H^2 \quad (2.17)$$

W_μ is the field of the charged vector boson and Z_μ is the neutral gauge boson. As seen from Eq.(2.17) the spontaneous symmetry breaking result in the following mass terms for W, Z and Higgs fields.

$$\mathcal{L}_M = M_W^2 W^{+\mu} W_\mu^- + \frac{1}{2}M_Z^2 Z^\mu Z_\mu - \frac{1}{2}M_H^2 H^2 \quad (2.18)$$

Here,

$$\begin{aligned} M_W^2 &= \frac{1}{4}g^2v^2 \\ M_Z^2 &= \frac{1}{4}(g^2 + g'^2)v^2 \\ M_H^2 &= 2\lambda v^2 \end{aligned} \quad (2.19)$$

are the W-boson, Z-boson and the Higgs-boson mass squared respectively. A photon mass does not arise in Lagrangian. Thus, the $SU(2)_L \times U(1)_Y$ local gauge invariance is broken in a way that electrodynamics remains an exact symmetry of nature.

In the limit of low momentum transfer $q^2 \rightarrow 0$ we have the relation

$$\frac{G_F}{\sqrt{2}} = \frac{g^2}{8M_W^2} \quad (2.20)$$

Using the Eq.(2.20) and $e = g\sin\theta_w$ we obtain

$$M_W = \frac{e}{2\sin\theta_w} \left(\frac{\sqrt{2}}{2G_F}\right)^{1/2} = 80 \text{ GeV}$$

Table 2.2: Basic Standard Model parameters measured at LEP and SLC [18].

Parameters	Measurement
$M_Z(GeV)$	91.1871 ± 0.0021
$M_W(GeV)$	80.448 ± 0.062
$M_t(GeV)$	174.3 ± 5.1
$\sin^2\theta_w$	0.2255 ± 0.0021

This prediction is in very good agreement with the experimental results as shown in Table (2.2).

The next step is to generate the fermions masses. In order to generate the fermions masses we must introduce an interaction of these fermions with the Higgs boson in the Lagrangian. Yukawa coupling among ϕ , fermion doublet f_L and singlet f_R gives

$$\mathcal{L}_f = -G_f[\bar{f}_L\phi f_R + \bar{f}_R\phi^\dagger f_L] \quad (2.21)$$

where G_f is the coupling constant. The spontaneously broken form of Eq.(2.21) is obtained by substitution of Eq.(2.14) into Eq.(2.21) and is given by

$$\begin{aligned} L_f &= -G_f \frac{v+h}{\sqrt{2}}[\bar{f}_L f_R + \bar{f}_R f_L] \\ &= -G_f \frac{v}{\sqrt{2}}\bar{f}f - \frac{G_f}{\sqrt{2}}h\bar{f}f \end{aligned} \quad (2.22)$$

Here, f is the fermion fields. we can identify the coefficient of the first term on the right-hand side of Eq.(2.22) as the fermion mass, $m_f = G_f \frac{v}{\sqrt{2}}$.

2.4 Neutrino Mass

In Standard Model neutrinos are introduced as massless; and essentially because of this, their magnetic moments [49], their mixing matrix etc also vanish [7,12]. However, there is no fundamental reason why the neutrinos should be massless; it would be more natural for them to have finite masses, like all other

fermions. In fact most of the extensions of the Standard Model predict massive neutrinos. In the following section we will see that how the mass rise in the theory.

2.4.1 Dirac Mass Term

In extensions of the Standard Model, one can introduce extra fermions, so that the model can predict massive neutrinos. So let us add right-handed ν_R neutrino fields corresponding to each charged lepton, and see what happens.

The presence of these right-handed neutrino field imply the following mass term [7,12],

$$L^D = -(\bar{\nu}_R M^D \nu_L + \bar{\nu}_L M^D \nu_R) \quad (2.23)$$

where

$$\nu_L = \begin{pmatrix} \nu_e \\ \nu_\mu \\ \nu_\tau \end{pmatrix}_L, \quad \nu_R = \begin{pmatrix} \nu_e \\ \nu_\mu \\ \nu_\tau \end{pmatrix}_R \quad (2.24)$$

and the mass matrix M^D is, in general, a complex $N \times N$ matrix. Here we assumed that number of generations N is 3. To obtain the physical fields one must find the eigenvectors of the matrix, M . In general, this can be done by diagonalizing M^D with a biunitary transformation:

$$m = V^\dagger M^D U$$

or

$$M^D = V m U^\dagger \quad (2.25)$$

where V and U are unitary matrices and m is a diagonal matrix. Inserting Eq.(2.25) into Eq.(2.23) we get

$$\begin{aligned} L^D &= -(\bar{\nu}'_R m \nu'_L + \bar{\nu}'_L m \nu'_R) \\ &= -\sum m_k \bar{\nu}'_k \nu'_k \end{aligned} \quad (2.26)$$

Here,

$$\begin{aligned}
\nu_k &= \nu_{kL} + \nu_{kR} \\
\nu'_L &= U^\dagger \nu_L \\
\nu'_R &= V^\dagger \nu_R.
\end{aligned} \tag{2.27}$$

Since U and V are unitary matrices; we can rewrite Eq.(2.27) as

$$\begin{aligned}
\nu_{lL} &= \sum_k U_{lk} \nu_{kl} \\
\nu_{lR} &= \sum_k V_{lk} \nu_{kl}
\end{aligned}$$

An immediate consequence of neutrino mixing is that the general lepton numbers; L_e, L_μ and L_τ are no more good global symmetries because any mass eigenstate is a mixture of ν_e, ν_μ, ν_τ . However, Lagrangian of the theory containing the mass term as in Eq.(2.26) is invariant with respect to the global gauge transformations

$$\nu_{lL}(x) \rightarrow e^{i\Lambda} \nu_{lL}(x), \quad \nu_{lR}(x) \rightarrow e^{i\Lambda} \nu_{lR}(x), \quad l(x) \rightarrow e^{i\Lambda} l(x), \quad l = e, \mu, \tau$$

where Λ is a constant parameter. The invariance of Lagrangian under this gauge transformation leads to conservation of total lepton number, $L = L_e + L_\mu + L_\tau$. Thus, processes like

$$\mu^+ \rightarrow e^+ \gamma, \quad \mu^+ \rightarrow e^+ e^- e^+, \quad \text{and} \quad K^+ \rightarrow \pi^+ \mu^+ e^-$$

are allowed and oscillation $\nu_l \rightarrow \nu_{l'}$ should be observed. However, neutrinoless double- β decay and processes like $K^+ \rightarrow \pi^- e^+ \mu^+$ are forbidden as a consequences of the conservation of total lepton charge, L .

2.4.2 Majorana Mass Term

The main difference between neutrinos and other fundamental fermions is that neutrinos do not carry any electric charge. This brings a new possibility that neutrinos might be Majorana particles with the consequence that neutrino is its own

antiparticle. There are no good quantum numbers that distinguish the neutrinos from anti-neutrinos.

The Majorana mass is given by the following Lagrangian [7,12]

$$L^M = -\frac{1}{2}(\bar{\nu}_L^c)M\nu_L + h.c. \quad (2.28)$$

Where

$$\nu_L = \begin{pmatrix} \nu_e \\ \nu_\mu \\ \nu_\tau \end{pmatrix}_L \quad (2.29)$$

and M is a complex 3×3 matrix (we assume that number of the generations N=3) and also M is a symmetric matrix. We verify this as follows:

$$\begin{aligned} (\bar{\nu}_L^c)M\nu_L &= -(\nu_L^T C^{-1} M \nu_L)^T \\ &= \nu_L^T (C^{-1})^T M^T \nu_L \\ &= (\bar{\nu}_L^C) M^T \nu_L \end{aligned} \quad (2.30)$$

where C is the charge conjugation matrix obeying the conditions, $C^T = -C$, $C^\dagger C = I$. The negative sign appears in Eq.(2.30) because of the interchange of the orders of two anticommuting fermion fields. Eq.(2.30) implies

$$M^T = M$$

In order to express the Lagrangian L^M in the standard form let us diagonalize the matrix, M. A complex symmetric matrix can be diagonalized by a unitary matrix, U

$$m = U^\dagger M U \quad (2.31)$$

Substituting Eq.(2.31) into Eq.(2.28) we get

$$\begin{aligned} L^M &= \frac{1}{2}\nu_L^T C^{-1} U m U^\dagger \nu_L + h.c. \\ &= -\frac{1}{2}\bar{\chi} m \chi \\ &= -\frac{1}{2} \sum_k m_k \bar{\chi}_k \chi_k \end{aligned} \quad (2.32)$$

where

$$\chi = U^\dagger \nu_L + (U^\dagger \nu_L)^c \quad \text{so,} \quad \chi_k^c = \chi_k \quad (2.33)$$

which is a Majorana field. From Eq.(2.33) we obtain

$$\chi_L = U^\dagger \nu_L \quad (2.34)$$

since U is an unitary operator we can write

$$\nu_L = U \chi_L \quad (2.35)$$

or

$$\nu_{lL} = \sum_k U_{lk} \chi_{kl} \quad (2.36)$$

Thus, if the neutrino mass term given by Eq.(2.32), the LH current fields, ν_{lL} ($l=e, \mu, \tau$) are superpositions of the LH components of the neutrino fields with the Majorana masses, m_k ($k=1, 2, 3$). One of the consequences of introducing the Majorana mass term is the violation of lepton number. Therefore, a theory with a Majorana mass term, allows not only process such as $\mu^+ \rightarrow e^+ \gamma$, $\mu^+ \rightarrow e^- e^+ e^-$ but also double decay.

2.5 Neutrino Oscillations

There is no easy and direct way to detect neutrino masses. However, one method which is very promising and very interesting to examine, is the neutrino oscillations. The neutrino oscillation phenomenon was first discussed by B. Pontecorvo (1957) [11]. The physics of neutrino oscillation is similar to that of strangeness oscillation for neutral kaons. In order to formulate neutrino oscillation, one should start with the following assumptions: neutrinos are massive (and mass eigenstates are not degenerate) and mixed. In that case, for an observable state of neutrinos with the momentum \mathbf{p} we have,

$$|\nu_\alpha\rangle = \sum_i U_{\alpha i}^* |\nu_i\rangle, \quad \alpha = e, \mu, \tau \quad (2.37)$$

where $|\nu_\alpha\rangle$ is a weak eigenstate and $U_{\alpha i}$ is an unitary matrix $U^\dagger U = 1$. $|\nu_i\rangle$ is a mass eigenstate of neutrino with momentum \mathbf{p} , energy

$$E_i = \sqrt{p^2 + m_i^2} \simeq p + \frac{m_i^2}{2p} \quad (2.38)$$

Here, we assume $p \gg m$, i.e. relativistic neutrino. The propagation in space time is given by the relation

$$|\nu_\alpha\rangle_t = \sum_i U_{\alpha' i}^* e^{-iE_i t} |\nu_i\rangle \quad (2.39)$$

From Eq.(2.37) and unitary properties of $U_{\alpha i}$ we have

$$|\nu_i\rangle = \sum_{\alpha'} |\nu_{\alpha'}\rangle U_{\alpha' i} \quad (2.40)$$

From Eqs. (2.39) and (2.40) we have

$$|\nu_\alpha\rangle_t = \sum_{\alpha'} |\nu_{\alpha'}\rangle A_{\nu' \nu_\alpha}(t) \quad (2.41)$$

where

$$A_{\nu' \nu_\alpha}(t) = \sum_i U_{\alpha' i} e^{-iE_i t} U_{\alpha i}^*$$

is the amplitude of the transition $\nu_\alpha \rightarrow \nu_{\alpha'}$ at the time t . The meaning of the transition amplitude, $A_{\nu' \nu_\alpha}(t)$ is the following: the term $U_{\alpha' i}^*$ is the amplitude of transition from the state ν_α to state ν_i ; the term $e^{-iE_i t}$ describes the evolution in the state with energy E_i , the term $U_{\alpha i}^*$ is the transition amplitude from state $|\nu_i\rangle$ to state $|\nu_{\alpha'}\rangle$.

The different $|\nu_i\rangle$ gives a coherent contribution to the amplitude $A_{\nu' \nu_\alpha}(t)$. From Eq.(2.41) it follows that the transitions between the different states can take place only if: i) at least two neutrino masses are different ii) the mixing matrix is nondiagonal.

We can get transition probability from Eq.(2.41) as

$$\begin{aligned} P_{\nu_\alpha \rightarrow \nu_{\alpha'}} &= \left| \sum_i U_{\alpha' i} e^{-i(E_i - E_1)t} U_{\alpha i}^* \right|^2 \\ &= \left| \delta_{\alpha\alpha'} + \sum_i U_{\alpha' i} U_{\alpha i}^* (e^{-i\Delta m_{i1}^2 \frac{L}{2p}} - 1) \right|^2 \end{aligned} \quad (2.42)$$

where $\Delta m_{i1}^2 = m_i^2 - m_1^2$ and $L \simeq t$ is the distance between the neutrino source and the detector.

2.5.1 Two Flavour Oscillation

In the case of two flavour oscillation we have oscillation probability as

$$P(\nu_\alpha \rightarrow \nu'_\alpha) = |\delta_{\alpha\alpha'} + U_{\alpha'2}U_{\alpha 2}^*(e^{-i\Delta m_{21}^2 \frac{L}{2p}} - 1)|^2 \quad (2.43)$$

For $\alpha' \neq \alpha$,

$$P(\nu_\alpha \rightarrow \nu'_\alpha) = P(\nu_{\alpha'} \rightarrow \nu_\alpha) = \frac{1}{2}A_{\alpha'\alpha}(1 - \cos\Delta m^2 \frac{L}{2p}). \quad (2.44)$$

Here the amplitude of oscillation is equal to

$$A_{\alpha'\alpha} = 4|U_{\alpha'2}|^2|U_{\alpha 2}|^2 \quad (2.45)$$

and $\Delta m^2 = m_2^2 - m_1^2$. Introducing the mixing angle θ as

$$|U_{\alpha 2}| = \sin\theta, \quad |U_{\alpha' 2}| = \cos\theta \quad (2.46)$$

and using $|U_{\alpha 2}|^2 + |U_{\alpha' 2}|^2 = 1$, the oscillation amplitude is $A_{\alpha'\alpha} = \sin^2 2\theta$. Therefore the oscillation probability is

$$P(\nu_\alpha \rightarrow \nu_{\alpha'}) = \frac{1}{2}\sin^2 2\theta(1 - \cos\Delta m^2 \frac{L}{2p}) \quad (2.47)$$

or ($p \sim E$)

$$P(\nu_\alpha \rightarrow \nu_{\alpha'}) = \frac{1}{2}\sin^2 2\theta \sin\left(\frac{1}{2}\frac{\Delta m^2 L}{2E}\right) \quad (2.48)$$

2.5.2 Neutrino Oscillations Experiments

Experimental searches for neutrino oscillations can be classified into two groups: appearance and disappearance experiments. In the first type, one is looking for the appearance of neutrinos of a given flavour, ν_l at some distance from a source of neutrinos of a different flavour. In the second type, at some distance from the sources of neutrinos of a definite flavour, one detects the reduction in the neutrinos of the same flavour. Experiments of first type answer the question, whether the probability

$$P(\nu_\alpha \rightarrow \nu_\alpha) = 1 - \sum_{\alpha \neq \alpha'} P(\nu_\alpha \rightarrow \nu_{\alpha'}) \quad (2.49)$$

is different from unity. The appearance experiments can be very sensitive to small mixing angles, as it is in principle sufficient to detect a small number of events induced by flavour changed neutrinos. The second method is less sensitive to small mixing amplitudes. It is limited by statistics and systematic uncertainties in the absolute intensity of the neutrino source used, the neutrino spectrum and detection efficiency.

Searches for oscillation phenomena have been made using the neutrinos from reactors, accelerators and interactions of cosmic rays in the atmosphere. High energy accelerators produce intense ν_μ and $\bar{\nu}_\mu$ beams which are used in neutrino oscillation experiments to search for the occurrence of a new neutrino flavour. Many experiments have searched for the phenomenon of neutrino oscillations.

2.6 Evidence for Neutrino Oscillations

Recently, evidences for the neutrino oscillations have been found in some accelerator and atmospheric neutrino experiments. In the following sections we will discuss them.

2.6.1 LSND Experiment

An indication for flavour $\bar{\nu}_\mu \rightarrow \bar{\nu}_e$ oscillations was found in the LSND experiment which was carried out at Los Alamos linear accelerator with protons of 800 MeV energy. This is a beam stop experiment: most of the pions produced by protons come to rest in the target and decay mainly by $\pi^+ \rightarrow \mu^+ \nu_\mu$. The μ^+ 's also come to rest in the target and decay by $\mu^+ \rightarrow e^+ \nu_e \bar{\nu}_\mu$. Thus the beam-stop target is a source of ν_μ, ν_e and $\bar{\nu}_\mu$.

The Large Scintillator Neutrino Detector LSND was located at a distance of about 30 m from the neutrino source. In the detector the $\bar{\nu}_e$'s were searched for through the observation of the process

$$\bar{\nu}_e p \rightarrow e^+ n \tag{2.50}$$

Both e^+ and delayed 2.2 MeV γ 's from the capture reaction $np \rightarrow d\gamma$ were detected.

In the LSND experiment [70] 33.9 ± 8.0 events were found in the interval of e^+ energies $30 < E < 60 \text{ MeV}$. Assuming these are coming from $\bar{\nu}_\mu \rightarrow \bar{\nu}_e$ oscillation, the transition probability was found to be

$$P(\bar{\nu}_e \rightarrow \bar{\nu}_\mu) = (0.31 \pm 0.09 \pm 0.06) \times 10^{-3} \quad (2.51)$$

On the other hand, KARMEN experiment [18] which uses a similar beam to LSND, does not confirm this result. The indication for $\bar{\nu}_\mu \rightarrow \bar{\nu}_e$ oscillations obtained in the LSND experiment will be checked by the BOONE experiment at Fermilab, scheduled for 2001-2002.

2.6.2 Atmospheric Neutrino Experiments

Atmospheric neutrinos are mainly produced in the decay of pions and muons

$$\pi^+ \rightarrow \mu^+ \nu_\mu, \quad \mu^- \rightarrow e \nu_e \nu_\mu \quad (2.52)$$

the pions being produced in the interaction of cosmic rays. At small energies ($1 \text{ GeV} \leq$) the ratio of fluxes of ν_μ 's and ν_e 's from the decays (in Eq.(2.52)) equal two. At higher energies the ratio is larger than two (not all muons decay in atmosphere). But there is a large uncertainty concerning the absolute fluxes of ν_e ($\bar{\nu}_e$) and ν_μ ($\bar{\nu}_\mu$) expected from different models. However all the models yield approximately the same values for the ratio of the fluxes of muon neutrinos to electrons neutrinos. This is the reason why the results of measurements of total fluxes of atmospheric neutrinos are presented in the form of a double ratio

$$R = \frac{\left(\frac{N_\mu}{N_e}\right)_{DATA}}{\left(\frac{N_\mu}{N_e}\right)_{MC}} \quad (2.53)$$

The detector which is mainly a large Cherenkov detector consist of two parts: the inner one of 50 kton is covered with 11146 photomultipliers, the outer part, 2.75 m thick is covered by 1885 photomultipliers. The electrons and muons are detected

by observing the Cherenkov radiation. The efficiency of particle identification is 98%. The observed events are divided into fully contained events (FC) for which Cherenkov light is deposited in the inner detector, and partially contained events (PC) in which muon track deposits part of its Cherenkov radiation in outer detector. FC is further divided into sub-GeV events ($E_{vis} \leq 1.33\text{GeV}$) and multi-GeV events $E_{vis} \geq 1.33\text{GeV}$. In the Super-Kamikonde experiment [72] for sub-GeV events and multi-GeV events (FC and PC), the following values double ratio R obtained respectively

$$R = 0.680_{-0.022}^{+0.023} \pm 0.053 \quad (2.54)$$

$$R = 0.678_{-0.039}^{+0.042} \pm 0.080 \quad (2.55)$$

These values are in agreement with values obtained in other water Cherenkov experiments (Kamiokande and IMB [18]) and in the SOUDAN2 [74] experiment in which the detector is an iron calorimeter a similar result is found

$$R = 0.65 \pm 0.05 \pm 0.08 \quad \textit{Kamiokande} \quad (2.56)$$

$$R = 0.54 \pm 0.05 \pm 0.11 \quad \textit{IMB} \quad (2.57)$$

$$R = 0.61 \pm 0.15 \pm 0.05 \quad \textit{SOUDAN2} \quad (2.58)$$

The fact that the double ratio R is significantly less than one is an indication of neutrino oscillations. The observed ν_μ disappearance may be partially due to $\nu_\mu \rightarrow \nu_{sterile}$ even though the investigations so far favour the $\nu_\mu \rightarrow \nu_\tau$ oscillation. Therefore next generation neutrino oscillation search at accelerators will mainly probe the parameter region pointed by the atmospheric neutrino oscillation claim. These are the long base line (LBL) experiments.

The first LBL accelerator experiment K2K [73] is now running with an average energy of 1.4 GeV, The neutrinos are produced at KEK accelerator and detected in

the Super kamioande detector (at distance 250km). The disappearance $\nu_\mu \rightarrow \nu_e$ will be investigated in detail. This experiment is sensitive to $\Delta m^2 \geq 2 \times 10^{-3} eV^2$ at large $\sin^2 2\theta$.

In the Kam-land experiment, the $\bar{\nu}_e$ from a reactor at a distance of 150-200 km from the detector will be investigated. The neutrino oscillations $\bar{\nu}_e \rightarrow \bar{\nu}_x$ with $\Delta m^2 \geq 10^{-5} eV^2$ and large values of $\sin^2 2\theta$ will be explored.

A neutrino beam with an average energy $\sim 4-20 GeV$ will be sent to Gran Saso from CERN (~ 732 km) in order to search for $\nu_\mu \rightarrow \nu_\tau$ or ($\nu_\mu \rightarrow \nu_e$) oscillations. OPERA [61] is one of the experiments, aiming at an appearance search for $\nu_\mu \rightarrow \nu_\tau$ and soon the construction of the detector set-up at Gran Sasso will start. It will be sensitive to the parameter region indicated by atmospheric neutrino anomaly. The experiment design is based on the Emulsion Cloud Chamber (ECC) detector, a modular structure made up of a sandwich of passive material (Fe, Pb) plates and thin emulsion sheets. The emulsion is used for tracking and τ decays are to be identified by a direct kink detection.

The other LBL experiment MINOS [18] is to be located at SOUDAN mine, 730 km from Fermilab. It will use a neutrino beam with an average energy of 10 GeV from Fermilab. They will use kinematical analysis to detect ν_τ appearance and will look for ν_μ disappearance by observing the CC/total interaction ratio and comparing the energy spectra at the close (a small near detector will be located at Fermilab) and far detector (at SOUDAN mine).

2.7 Neutrino Charged Current Interaction

Neutrino nucleon charge current interaction is classified as Deep Inelastic Scattering (DIS)[6, 18]: if the nucleon is broken up in interaction, and as Quasielastic scattering if the nucleon is left intact. Deep inelastic scattering does not only allow for tests of perturbative QCD but also provides information about distribution of partons within the proton. Neutrino nucleon charge current interaction may be

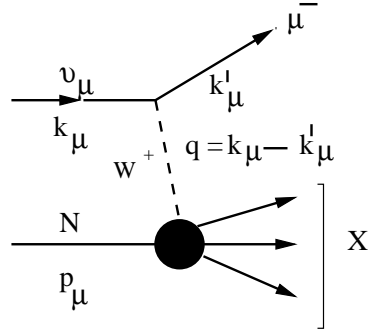


Figure 2.1: Diagram shows neutrino D.I.S. interaction with nucleon.

written as

$$\nu_\mu N \rightarrow \mu^- X \quad (2.59)$$

Where N is the nucleon and X is the final state hadron (hadrons). The process is mediated by W -boson exchange and as interaction Lagrangian given by

$$\mathcal{L} = -\frac{g}{2\sqrt{2}}(J_\mu W^\mu + J_\mu^\dagger W^{\dagger\mu}) \quad (2.60)$$

where J_μ is defined in section 2.1.

2.7.1 Parton Model

The quark-parton model provides a very good approximation of the nucleon as a collection almost free point like partons: three valence quarks and a sea of quark and antiquark pairs.

Deep inelastic scattering is usually characterized by the following variables

$$\begin{aligned} Q^2 &= -q^2 = -(k_\mu - k'_\mu)^2 \\ x &= \frac{Q^2}{2p \cdot q} = \frac{Q^2}{2M(E - E')} \\ y &= \frac{p \cdot q}{p \cdot k} = \frac{E - E'}{E} \end{aligned} \quad (2.61)$$

The variable " Q^2 " is referred to as the momentum transfer, " $E - E'$ " is the energy transferred to recoiling hadrons. In the parton model the struck nucleon is

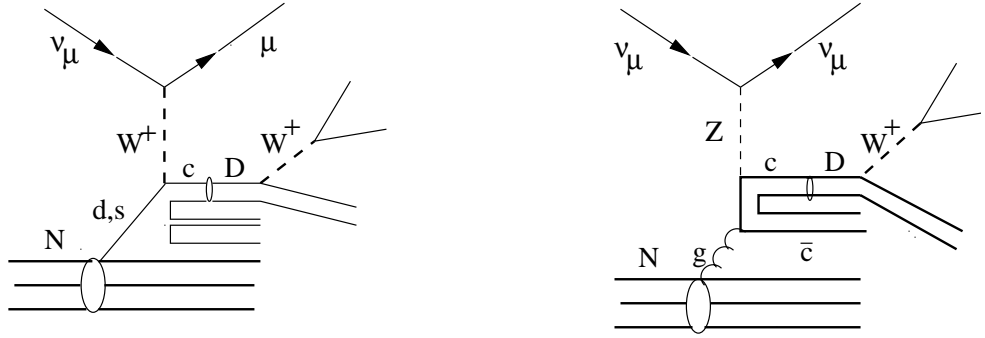


Figure 2.2: Charmed hadron production by neutrino charge current (left) and neutral current (right) interactions.

composed of a number of quarks (3 valence quarks and sea quarks) and neutrino interacts with one of the quarks. The variable "x" is the fraction of the nucleon energy processed by the struck quark. The variable "y" is the fraction of the available energy associated with the recoiling mass.

The cross section of this process is given by

$$\frac{d^2\sigma(\nu_\mu N \rightarrow \mu^- X)}{dxdy} = \frac{G^2}{\pi} ME \left[xy^2 F_1 + \left(1 - y - \frac{Mxy}{2E}\right) F_2 + xy \left(1 - \frac{1}{2}y\right) F_3 \right]$$

where F_1, F_2, F_3 are structure functions which are related to the quark "distribution functions" or "densities" $q(x, \mu^2)$, where $q(x, \mu^2)dx$ is the probability that the parton considered carries a momentum fraction x of the target nucleon momentum.

2.7.2 Charm Production by Neutrino Charged Current Interaction

Figure (2.2) shows charmed hadron production by neutrino deep inelastic scattering. In the charge-current interaction neutrino interacts with "valence" d quark or "sea" s quark and produces c quark. Then hadronization process occurs that is c quark "dresses" itself with other quarks or antiquarks from "valence" and

”sea” quarks of the interacting nucleon so then a charm hadron is produced. In the case of neutral current interaction, only gluon initiated diagrams are possible. Gluon splits into $c\bar{c}$ then c -quark ”dresses” itself with other quarks to produce charm hadron. Since d to c transition is Cabibbo suppressed and number of ”sea” s quark is not many, charm production by neutrino deep inelastic process is low. Main characteristics of the charmed hadrons are summarized in Table 2.3

Table 2.3: Charmed hadron properties [75].

Charm Hadron	quark com.	Mass(MeV)	lifetime (ps)
\mathbf{D}^0	$c\bar{u}$	1864.6 ± 0.5	0.415 ± 0.004
\mathbf{D}^+	$c\bar{d}$	1869.3 ± 0.5	1.057 ± 0.015
\mathbf{D}_s^+	$c\bar{s}$	1968.5 ± 0.6	0.467 ± 0.017
λ_c^+	udc	2284.9 ± 0.6	0.206 ± 0.012

CHAPTER 3

THE EXPERIMENTAL APPARATUS

The CHORUS (CERN Hybrid Oscillation Research apparatus) experiment was originally designed to search for $\nu_\mu \rightarrow \nu_\tau$ oscillation; but drastic improvements in the automatic scanning allowed the experiment to study also charm physics.

The CHORUS detector is a hybrid system which is made of an emulsion target combined with electronic detectors. The electronic detectors reconstruct tracks and predict the positions of the events in the emulsion target. Using electronic detector predictions an automatic scanning of emulsion target has been performed in order to find decay topologies.

As illustrated in Figure (3.1), CHORUS detector consists of the emulsion target, hadron spectrometer, calorimeter and muon spectrometer. In the following we briefly describe some technical properties and principal aims of all sub-detectors mounted in the CHORUS set-up [59, 64].

3.1 Emulsion Target

Nuclear emulsion still remains to be the only detector providing three dimensional spatial information with a resolution of $1 \mu\text{m}$. Hence emulsion is particularly suited for observing short living particles, like τ^- lepton. On the other hand it does not have direct time discrimination and must be observed with optical microscopes under relatively high magnification. Some of the recent emulsion experiments in which semi-automatic or automatic scanning was used is shown in Table 3.1.

Nuclear emulsion consists of silver bromide (AgBr) crystals as a sensitive device dispersed in a thin gelatin layer (the composition of the CHORUS emulsion is

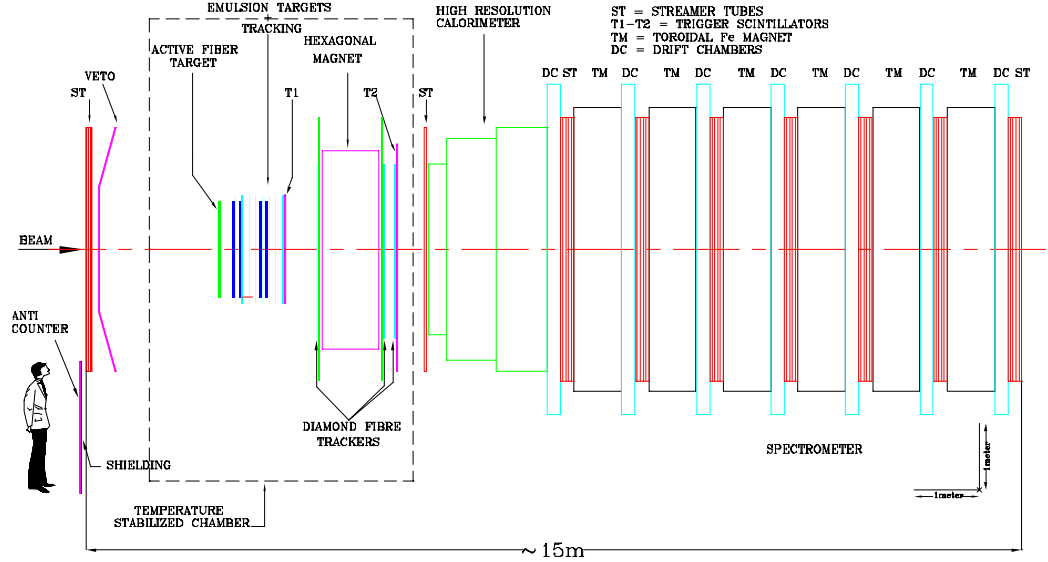


Figure 3.1: Schematic diagram of CHORUS detector

shown in Table (3.5)). When the charged particle passes through nuclear emulsion, it forms latent images ionizing the silver bromide. These images of tracks with characteristic dimensions $\sim 0.2\mu m$ are enhanced by suitable chemical processing techniques. After the processing the sizes of the silver grains making up the tracks become $\sim 0.6\mu m$ which can be seen when magnified by optical systems.

CHORUS emulsion consist of two components i) emulsion target where the neutrino interactions occur ii) interface emulsion sheets which are used as high accuracy tracking interface between the fiber tracker and the emulsion target.

Emulsion Target which consists of 4 emulsion stacks has a mass of about 770 kilograms. Each emulsion stack having dimensions of $1418 \times 1418 \text{ mm}^2$ is made of 8 emulsion modules. Every module consists of 36 individual emulsion plates which have two layers of emulsion gel on either side of a plastic base. The thickness of the base and each of the emulsion layers is $90 \mu m$ and $350 \mu m$ respectively. To

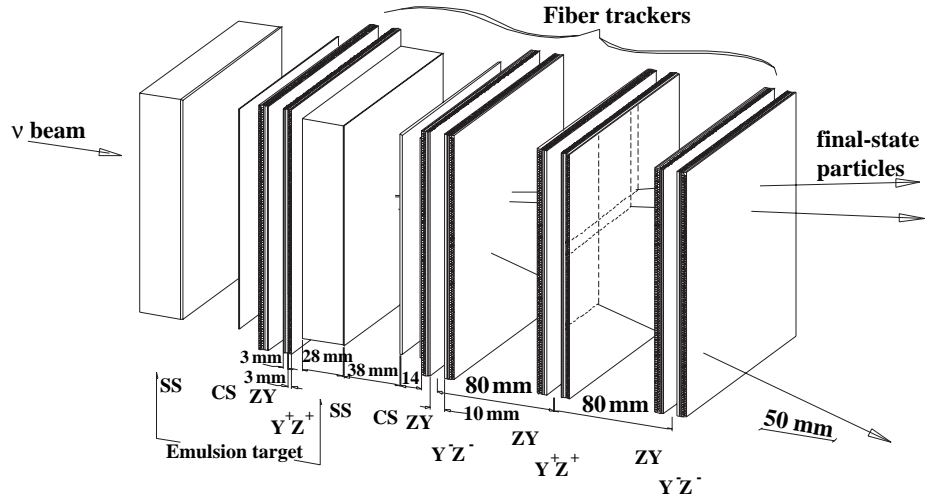


Figure 3.2: Schematic diagram of CHORUS target: Bulk emulsion, interface sheets and fiber tracker

reduce fading, emulsion stacks were kept at a temperature of $5C^o$ in a cool box. A set of bulk plates was exposed for a period of two years. When the exposure period ends, stacks were unpacked and a pattern of fiducial marks were created on every plate, using a mask and a xenon flash lamp. The fiducial marks are used for an internal calibration of the plates during the automatic scanning process.

Interface sheets have the same lateral dimensions as the bulk emulsion plates ($1418 \times 1418 \text{ mm}^2$) but the thickness is different: Interface sheets have $100 \mu\text{m}$ layers of emulsion coated on both sides of a $700 \mu\text{m}$ thick base. To keep the density of background tracks low, interface sheets were changed in certain periods.

3.1.1 Nikon Microscope

In order to scan the emulsion automatically, Nagoya group designed a computerized emulsion microscope [51, 38]. It consists of the Nikon stage, PC, Track Selector, CCD camera and Nikon optics. Mechanically the main part of the microscope is the Nikon stage and its acceptance is $35 \times 35 \text{ cm}^2$. Along the three

Table 3.1: Emulsion experiments in which semi-automatic or automatic scanning was used

Experiment	Physics aim	Beam	Emulsion vol.	# of loc. ev.
FNAL E531	Charm	ν	58.6	$\sim 4K$
CERN WA75	charm, beauty	π^-	80	$\sim 10K$
FNAL E653	charm, beauty	p, π^-	71	$\sim 50K$
CERN NA34	charm	O	6	$\sim 1K$
CERN EMU09	charm	S	3	$\sim 1K$
KEK E176	H-dibaryon	K^-	40	$\sim 1K$
CHORUS	$\nu_\mu \rightarrow \nu_\tau$	ν	206	$\sim 150K$
DONUT	ν_τ	π^-	40	203

axes the stage is driven by stepper motors. To have precise motion of the stage linear encoders are used. XY precision of the stage is of the order of a micron. The whole stage is managed by a controller which is linked to PC through an interface (called "DOMS (Digitized Online Microscope System)"). The microscope can be controlled in the semi-automatic mode by a joystick. As objectives, $50\times$ oil immersion lense and $10\times$ dry lenses are used. The images are collected by a Hamamatsu CCD (C3077) camera with 768×512 pixels. The emulsion readout is based on the hardware called "Track selector" (TS) which is a type of video image processor and has 16 frame memories. The operational principles of TS is the following: Tomographic images are taken and digitized by focusing at 16 different depths in a $100\ \mu\text{m}$ thick emulsion layer. The digitized images are shifted according to the track angle and added. The tracks are identified as enhancement of the pulse height and considered as found if the pulse height corresponding to 12 grains is collected in the 16 layers. The TS track finding efficiency as a function of track slope is shown in Figure (4.8). The efficiency is higher than 98 % up to about 400 mrad. In Ankara we have a Nikon Microscope equipped with a second version of Track Selector (TS2). After TS, new versions of track selectors: NTS (New Track Selector), UTS (Ultra fast Track Selector) were developed in Nagoya University. Table 3.2 shows scanning speed of "Track selectors" [49].

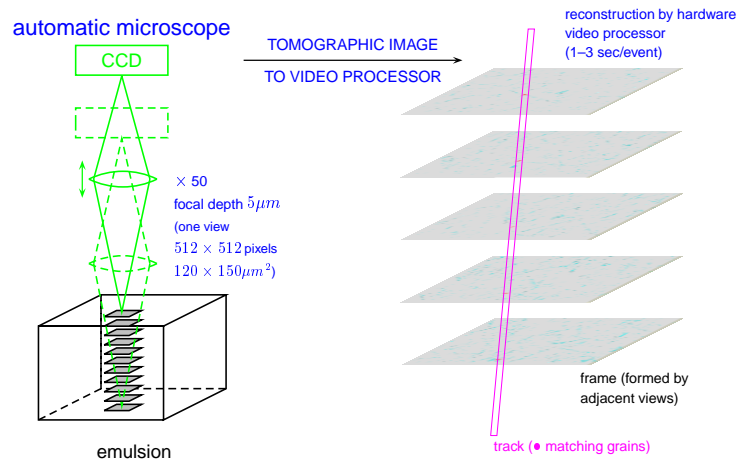


Figure 3.3: Automatic track recognition hardware.

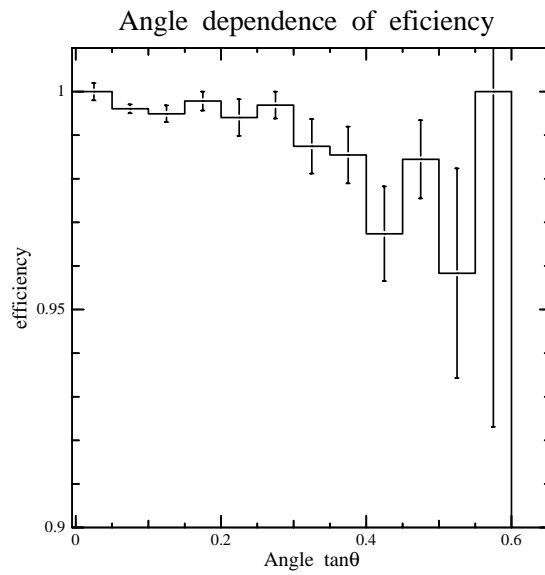


Figure 3.4: Track selector efficiency.

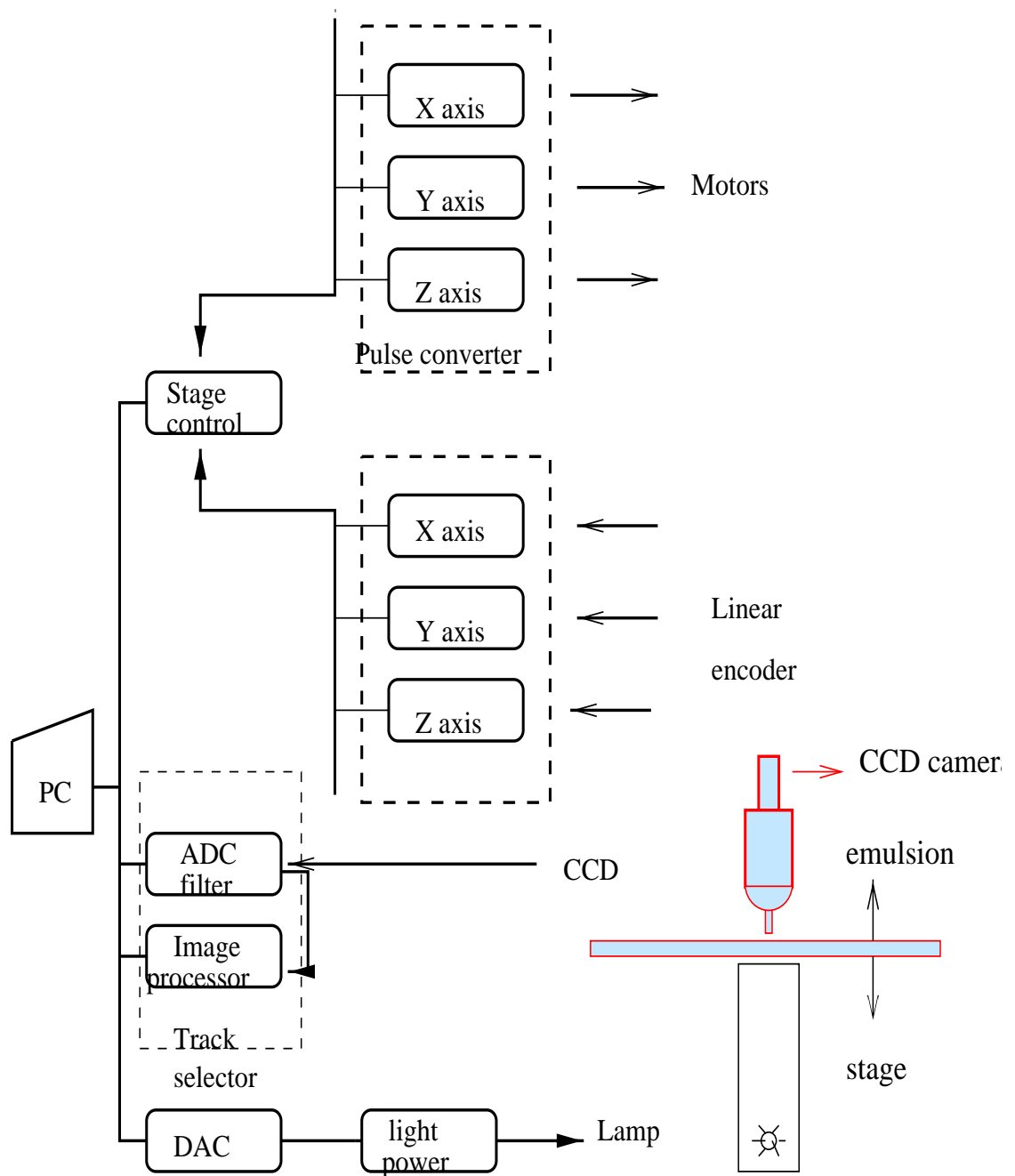


Figure 3.5: Block diagram of Nikon microscope equipped with TS2.

Table 3.2: Steps in the development of Track Selector systems. The scanning speed expressed in view per second (a view corresponding to an area of $\sim 0.018 \text{ mm}^2$) [49]

Name	Year	Scanning speed (Specified angle)	Scanning speed (All angle)
TS	1982	0.2	not tried
TS2	1994	0.4	0.008
NTS	1996	3	0.25
UTS	1998	3	3

3.2 Target Tracker

The main task of the target tracker, which is made of scintillating fibers of $500 \mu\text{m}$ in diameter and 2.3 m in length, is to locate in the emulsion stack the positions where the neutrino interactions takes place and to make accurate prediction of the coordinates of energetic secondary tracks from these interactions at the interface emulsion sheets. There are eight target tracker modules which were placed between the 4 emulsion targets, half of them shown in Figure (3.2). Each target module consist of four projection planes (Y, Z and Y^\pm , Z^\pm rotated by $\pm 8^\circ$ relative to Y, Z). By using information from these four projections three dimensional trajectories of transversing particles can be reconstructed. The prediction accuracy was measured as $\sigma \sim 150 \mu\text{m}$ in position and $\sigma \sim 2.5 \text{ mrad}$ in angle.

3.3 Hadron Spectrometer

Hadron spectrometer was located upstream of the calorimeter. It is used for measurement of the charge and momentum of particles before they enter the calorimeter. It is composed of three fiber tracking modules, streamer tube planes and a toroidal pulsed air-core magnet of hexagonal shape. There are three fiber trackers, called diamond tracker modules, one upstream and two downstream of the air core magnet which produce a homogeneous field of 0.12 Tesla in each

section parallel to the outer side. The momentum resolution $\Delta P/P$ of the magnet tracker results from the quadratic combination of two terms: a constant term at 22 % from multiple scattering and a term proportional to particle momentum which reflects the measurement accuracy. The resolution is given by the following expression

$$\frac{\Delta P}{P} = \sqrt{(0.22)^2 + (0.035p)^2} \quad (3.1)$$

3.4 Calorimeter

The main task of calorimeter is to measure the energy of the particles and to confirm the momentum measured in hadronic spectrometer. The calorimeter consist of 3 parts with decreasing granularity called, EM, HAD1 and HAD2. The total interaction depth corresponds to 144 radiation lengths and 5.2 interaction lengths such that 99 % of shower produced by a 5 GeV pion created are contained. The EM and HAD1 sections are made of by "spaghetti method": scintillating fibers of 1mm diameter embedded into a lead matrix with a lead to scintillator volume ratio of 4:1. The most downstream part of the calorimeter HAD2 is a lead/scintillator- strip sandwich with volume 4:1. The electron response was studied for different beam momenta in the range from 2.5 to 10 GeV. The energy dependent resolution is well fitted by the function

$$\frac{\sigma(E)}{E} = \frac{(13.8 \pm 0.9)\%}{\sqrt{E}} + (-0.2 \pm 0.4)\% \quad (3.2)$$

The results agree with Monte Carlo predictions. The response pions were studied in the range from 3 to 20 GeV. The energy dependence of the hadronic resolution is parametrized as

$$\frac{\sigma(E)}{E} = \frac{(32.3 \pm 2.4)\%}{\sqrt{E}} + (1.4 \pm 0.7)\% \quad (3.3)$$

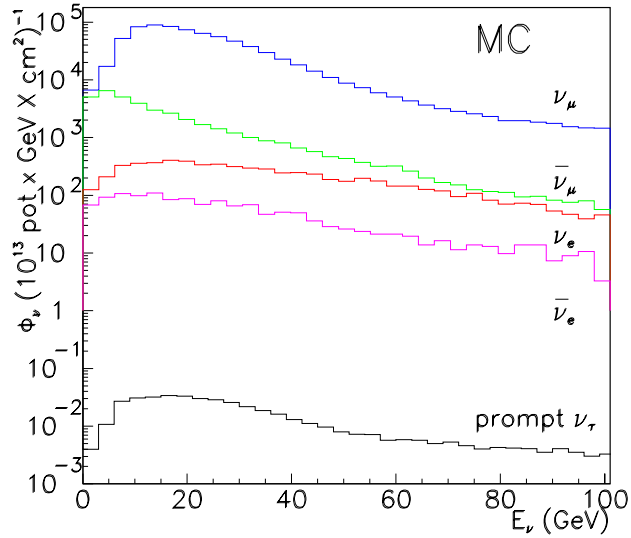


Figure 3.6: Neutrino beam energy spectrum

3.5 Muon Spectrometer

Almost all particles except muons stop before reaching the spectrometer. Hence, muon trajectory, momentum and charge are measured in a clean environment in the spectrometer which is located behind calorimeter. The spectrometer consists of six magnetized iron toroid modules and the tracking detectors made of drift chambers and limited streamer tubes. The scintillation counters in the gaps of the iron magnets have four functions. They are providing trigger signals for penetrating tracks and are complementing the measurement of hadron energy leaking from the preceding calorimeter. They also give range of muons stopping in one of the modules and they measure energy lost by bremsstrahlung in the iron modules. The momentum resolution of the muon spectrometer is about 19% at 71 GeV/c as measured by test muon beams.

3.6 Trigger

The main purpose of trigger is to select all the neutrino induced events in the target and reject background events due to cosmic rays, beam muons and

neutrino events outside target region. In addition, trigger modes for calibration and alignment of the detector are needed. The trigger consist of scintillator planes, named E, T, H, V and A. A neutrino trigger in the target region is defined by a coincidence hit in E, T and H consistent with the particle trajectory with $\theta < 0.250$ rad with respect neutrino beam direction and no activity in veto system (V, A). The measured rate of neutrino interactions is 0.5 events per 10^{13} proton on Be target. The fraction of events originating from emulsion is 50%. A trigger efficiency of 99 % (90 %) was measured for ν_μ CC (NC) events passing the offline selection criteria.

3.7 Neutrino Beam

The West Area Neutrino Facility (WANF) of the CERN SPS provides a beam of ν_μ mostly above threshold for ν_τ Charge Current interactions. Protons are accelerated by SPS to an energy of 450 GeV with a cycle of 14.4 s. They are extracted in two 6ms long spills separated in time by 2.7 s and are directed onto a beryllium target producing mainly pions and kaons. Neutrinos originate from their decays in flight, mostly in 289 m long vacuum tunnel. The relative abundance of the different neutrino flavours in the beam is given in the Table 3.3 and energy spectra are shown in Figure (3.6).

For calibration purposes a test beam ("X7") from SPS West Area is used. It is essentially a tertiary beam of pion with an average momentum 25 GeV/c.

Table 3.3: Relative composition of CHORUS neutrino beam.

Neutrino Type	Relative Aboun.	$\langle E \rangle$ (GeV)
ν_μ	100 %	26.9
$\bar{\nu}_\mu$	5.6 %	21.7
ν_e	0.7 %	47.9
$\bar{\nu}_e$	0.17 %	35.3

Table 3.4: The composition of CHORUS Fuji ET-7B emulsion

Element	Atomic number	Weight (%)	Mole Fraction (%)
Iodine (I)	53	0.3	0.06
Silver(Ag)	47	45.4	11.2
Bromine(Br)	36	33.4	11.1
Sulfur(S)	16	0.2	0.2
Oxygen(O)	8	6.8	11.3
Nitrogen(N)	7	3.1	5.9
Carbon(C)	6	9.3	20.6
Hydrogen(H)	1	1.5	40.0

Table 3.5: Decay modes producing neutrino beam.

Decay Modes	Branching Ratio
$\pi^+ \rightarrow \mu^+ \nu_\mu$	100%
$K^+ \rightarrow \mu^+ \nu_\mu$	63.5%
$K^+ \rightarrow \mu^+ \nu_\mu \pi^0$	3.2%
$K^+ \rightarrow e^+ \nu_e \pi^0$	4.8%
$K^+ \rightarrow e^+ \nu_e \pi^0$	4.8%
$K_L^0 \rightarrow e^+ \nu_e \pi^-$	19.4%
$K_L^0 \rightarrow \mu^+ \nu_\mu \pi^-$	13.6%
$\mu^+ \rightarrow e^+ \nu_e \bar{\nu}_\mu$	100%

CHAPTER 4

THE $\nu_\mu \rightarrow \nu_\tau$ OSCILLATION SEARCH ANALYSIS

In this chapter, CHORUS analysis procedure for $\nu_\mu \rightarrow \nu_\tau$ oscillation will be discussed. Using the sample analyzed in Ankara so far, a limit on $\nu_\mu \rightarrow \nu_\tau$ oscillation will be extracted.

4.1 CHORUS Phase I Analysis

In the CHORUS experiment, the signature of $\nu_\mu \rightarrow \nu_\tau$ oscillation is the detection of ν_τ charge current (CC) interaction vertex and subsequent decay vertex of τ^- lepton in the bulk emulsion target. The considered τ^- lepton decay channels are

$$\begin{aligned} (a) \quad \tau^- &\rightarrow \mu^- \bar{\nu}_\mu \nu_\tau & Br &= 17.37 \pm 0.09\% \\ (b) \quad \tau^- &\rightarrow h^- (n\pi^0) \nu_\tau & Br &= 49.52 \pm 0.07\% \end{aligned} \quad (4.1)$$

Both decay modes give rise to a kink topology: a track changes its direction after a short path as shown in Figure (4.1).

The first step of the data analysis in the CHORUS experiment is to run the reconstruction code, so called CHORAL (Chorus Offline Reconstruction and Analysis Library) [46] in order to reconstruct events in the electronic detectors.

4.2 Event Selection

Using information from electronic detectors, CHORUS data is classified as 1μ and 0μ sample in order to search the decay modes **(a)** and **(b)** in Eq.(4.1) respectively. 1μ sample contains mainly ν_μ CC interaction and a small contamination

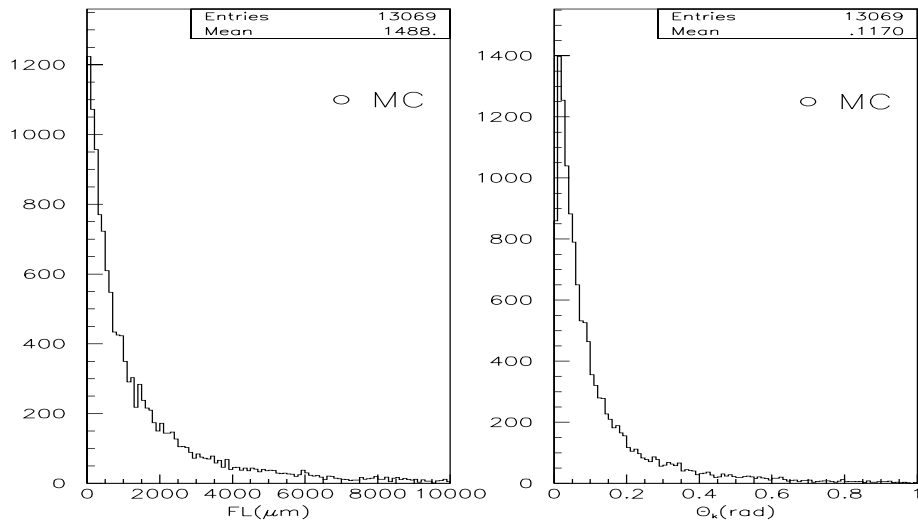
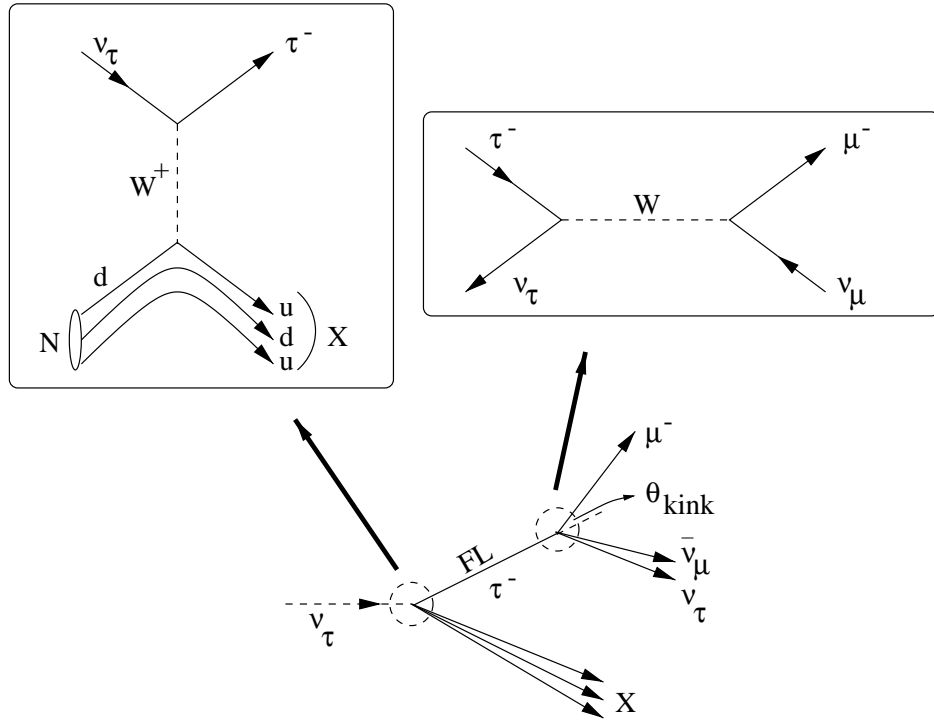


Figure 4.1: Top: decay topology of τ lepton, Bottom: flight length and kink angle of τ lepton from MC simulation.

from ν_μ NC (Neutral current) interaction with $\pi^-/K^- \rightarrow \mu^-$ decay. The 0μ sample mainly contains ν_μ NC interaction and a contamination from ν_μ CC events with unidentified muon in the electronic detectors. In addition to these two samples, 2μ sample which contains ν_μ CC interaction, is also scanned for charm search. Scanning of this sample is useful to check scanning efficiency.

Main selection criteria both for 1μ and 0μ samples are the following:

- vertex position is reconstructed in the bulk emulsion target,
- event has at least one reconstructed negative track which is supposed to come from τ^- candidate.

In addition to these requirements other kinematical cuts are applied in order to reduce scanning load while keeping high reconstruction and scanning efficiency for each mode.

4.2.1 Selection Criteria for 1μ Sample

As explained before, an event is classified as 1μ if it contains one reconstructed muon track of negative charge, as shown in Figure (4.2.3). and as 0μ if there is no reconstructed muon in the event. If the event fulfills the following conditions, it is searched for in the Changeable Sheet (CS).

- Muon slope is less than 400 mrad. This cut is applied in order to have good functioning of automatic scanning.
- Measured muon momentum is less than 30 GeV/c, if it is calorimeter muon, or less 28 GeV if momentum is measured by muon spectrometer. This cut improves signal to background ratio. Its result is 29% reduction on number of 1μ events to be scanned. It would reject 15 % of ν_τ interaction if ν_μ and ν_τ have the same energy spectrum.
- Track slope with respect to X7 beam direction is greater than 50 mrad (This cut is only applied on 1994 and 1995 data when X7 beam was run at high density.).

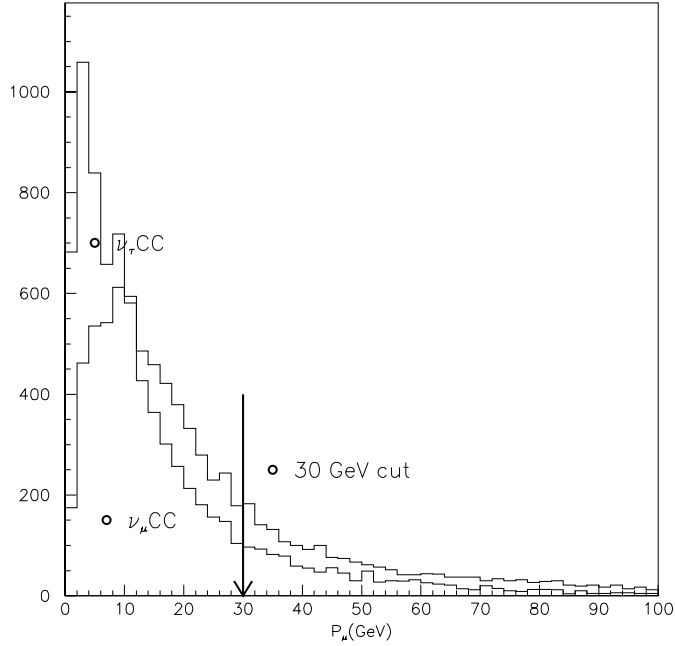


Figure 4.2: Applied momentum cut to the 1μ sample.

4.2.2 Selection Criteria for 0μ Sample

All the negatively charged tracks are considered in scanning for 0μ sample. Further criteria are the following:

- Track slope is less than 400 mrad.
- Measured momentum is between the limits $1\text{GeV} < P_{h^-} < 20\text{ GeV}$.
- track slope with respect to X7 beam direction is greater than 50 mrad (This cut is only applied on 1994 and 1995 data when X7 beam was run at high density.).

4.2.3 Selection Criteria for 2μ Sample

This sample is scanned for charm search. An event belongs to this sample if it has more than one reconstructed muon tracks, (at middle in Figure (4.2.3)). The only selection requirement for this sample is the following: one of the reconstructed muons must have a slope smaller than 400 mrad.

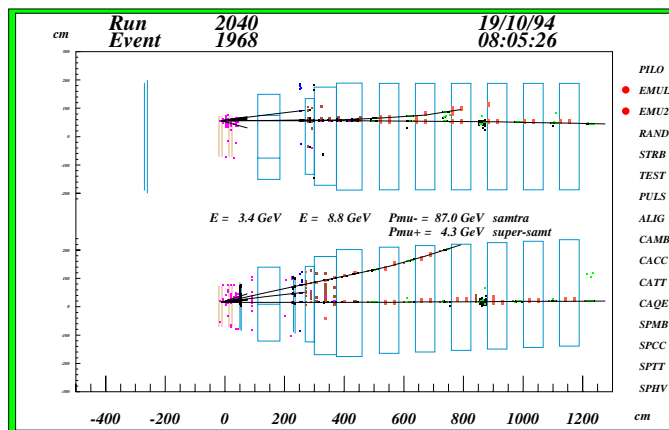
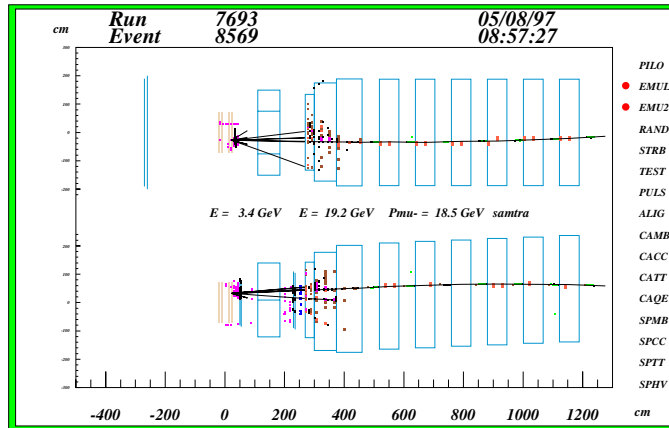
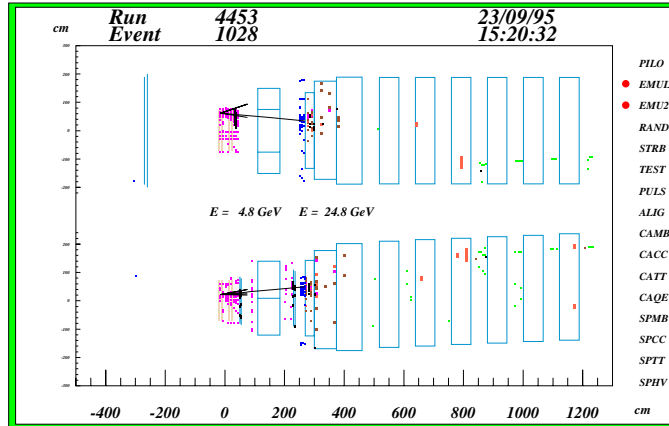
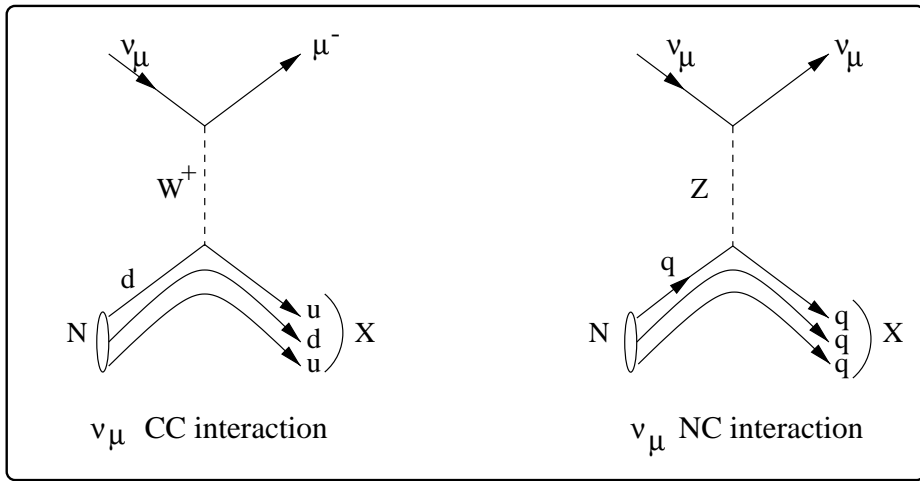



Figure 4.3: Event reconstructed as 0μ (Top), 1μ (Middle) and 2μ (Bottom) in the electronic detectors




 in emulsion

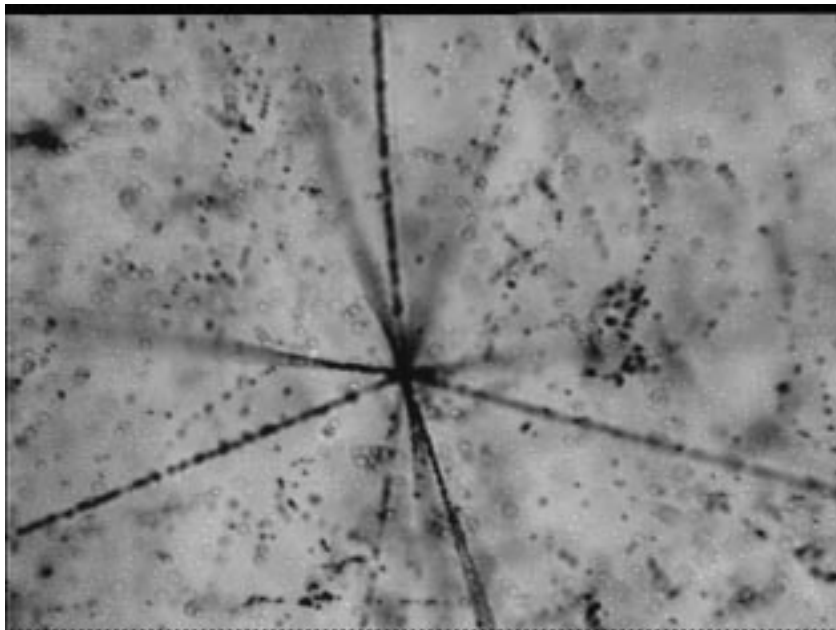


Figure 4.4: We have seen mainly, ν_μ CC or ν_μ NC interaction in emulsion

4.3 Emulsion Scanning

After classification and selection of events scanning has been performed by a fully automatic scanning system based mainly on the "Track Selector" (as explained in section 3.1.1.).

Emulsions are distributed to laboratories for scanning according to their scanning power. In CHORUS, most of the emulsion scanning has been performed in Nagoya emulsion laboratory.

The first step of emulsion scanning is to make predictions for selected tracks in interface sheets. The muon track (for 1 mu sample) and all negatively charged hadrons (for 0 mu sample), passing selection criteria, are searched for in CS. These tracks are called as "Scan Back" (SB) tracks.

4.3.1 Changeable Sheet Scanning

For selected events, SB parameters: slopes and positions, reconstructed in the fiber tracker, are used to guide the scan in the most downstream interface emulsion sheet. An automatic scanning is performed within 11×11 ($1080 \times 810 \mu m^2$) views around extrapolated position of SB track. A track is taken as a candidate if the angle difference, $\Delta\theta$, between predicted (fiber reconstructed) and measured angles is less than 30 mrad. A candidate having error, $\Delta\theta$, less than 6 mrad and pulse height (PH) greater than 13 is called "good stop". When a 'good stop' track is found within the scanning area, scanning is finished for that prediction. All the found candidates undergo checks for further selection to keep the good candidates for Special Sheet (SS) scanning that is in next plate (upstream) to CS. For 1994, 1995, 1996 runs, found tracks are kept for SS scanning if $\Delta\theta$ is less than 15 mrad and PH is greater than 10. For 1997 run, a different criterion is applied due to high track density in CS (in 1997 run only one CS sheet was used). This selection is based on χ^2 and PH values of track i.e.

- $\chi^2/n.d.f. < 3.5$ and (n.d.f=no. of degrees of freedom)

- $PH > 10$

All candidates satisfying these criteria are selected for SS scanning.

4.3.2 Special Sheet Scanning

After finding the track in CS they are followed in Special Sheet (SS), using position and slope information (only position information for 1996 and 1997 runs) from CS scanning. SS scanning is performed within the 7×7 microscope views ($800 \times 700 \mu m^2$) centered about predicted position. For 1994 and 1995 runs, the cut: $\Delta\theta < 15$ mrad is applied to select good candidates for bulk scanning and also 'good stop' method was used. For 1996 and 1997 runs, the criteria are:

- $\chi^2/n.d.f. < 3.3$ and
- $PH > 10$

As well as these criteria also 'good stop' method was used. The main advantage of this selection is to reduce fake predictions for the bulk scanning. All candidates satisfying these criteria are kept for the bulk scanning.

4.3.3 Vertex Location

SB track which has been found in the SS is then followed in the upstream direction plate by plate in the bulk emulsion using track segments in the most upstream, $100 \mu m$ of each plate. The measured position in the bulk plate, \mathbf{n} and angle in SS are used to predict position of the track in the bulk plate $\mathbf{n} + \mathbf{1}$. Track is said to be found in the bulk plate, \mathbf{n} if

- $\Delta r < \frac{2}{\sqrt{\pi}}(15 + 50 \times \Delta\theta_{x7}) \mu m$
- $\Delta\theta < \frac{2}{\sqrt{\pi}}(0.025 + 0.05 \times \Delta\theta_{x7}) rad$

where Δr is the position difference between predicted and measured positions, $\Delta\theta$ is the angle difference between predicted and measured angles and $\Delta\theta_{x7} =$

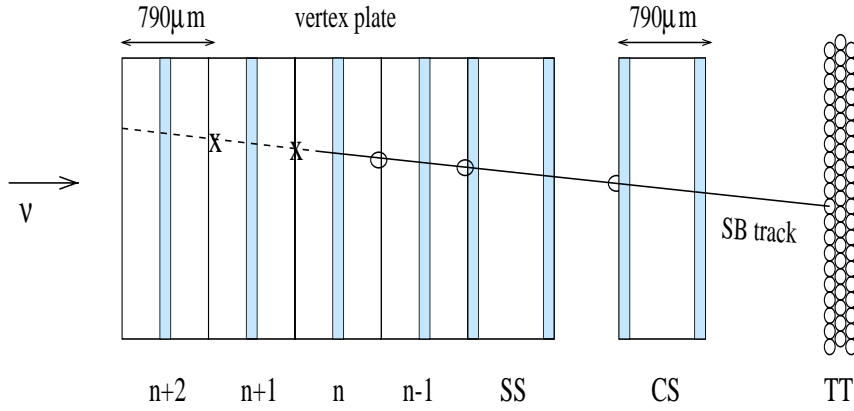


Figure 4.5: Event location

$\sqrt{(\theta_y - \theta_{x7y})^2 + (\theta_z - \theta_{x7z})^2}$, $(\theta_{x7y}, \theta_{x7z}) = (-0.080, 0)$ is the center value of X7 beam slope, and (θ_y, θ_z) is the track slope.

If SB track is not found in two successive emulsion plates (say in \mathbf{n} and $\mathbf{n} + \mathbf{1}$), plate \mathbf{n} , is decided to be a vertex plate which is supposed to contain the neutrino interaction or the decay vertex (or both) shown in Figure (4.5) Event location is not performed in the first 3 bulk plates due to high track density. The efficiency of vertex location (found/located) is evaluated as 92% for 1μ and 85% for 0μ from analysis of Ankara emulsion.

4.3.4 Decay Search

Once the vertex is located, an automatic decay search is performed by scanning a depth of $100 \mu\text{m}$ in the most upstream surface of the bulk emulsion plate. The aim of the decay search is to reduce manual check load while keeping events potentially containing a decay topology for detailed analysis and rejecting non-interesting events.

Different methods have been applied as a result of improvement in the scanning speed and feed back of applied scanning algorithms. Mainly 4 different methods

were applied for the decay search.

4.3.5 Method I

This method, applied to part of 1994 data, is effective for short decays. A search is performed for other predicted tracks (reconstructed by fiber tracker) in the upstream surface of the plate n-1 (downstream of vertex plate). Event is selected for eye-checking If the minimum distance between SB track and another predicted track is larger than $2 + 0.006 \times dx \mu m$ where dx is the vertex depth, measured from downstream surface of the emulsion plate. If only one track other than SB track is detected, video image analysis which will be explained in the next section, is applied.

4.3.6 Method II

This method, applied to part of 1994 and 1995 data, is called Video Image analysis. During the decay search scanning, full depth information of vertex plate is taken by recording 48 CCD images at $7 \mu m$ spaced depths on each surface of bulk emulsion target, centering SB track position. SB track is followed in the video image data. When a kink is detected, transverse momentum, \mathbf{P}_T , of daughter particle is calculated and if it is larger than $250 \text{ MeV}/c$, the event is selected for manual check. This method is not sensitive to kink angles larger than 150 mrad and decays occurring in the base and within $50 \mu m$ of the emulsion surfaces.

4.3.7 Method III

This procedure which is called Parent Search method was applied to all data. By this method, it is possible to hunt long decays with large angles (LL) and short decays (Long Half Large (LHL)): primary vertex and decay vertex are on opposite side of the base. LHL decay search was done only for 1996 and 1997 data for which a depth of $100 \mu m$ from downstream surface of base was also scanned in order to improve the decay finding efficiency. Kink angles larger than

25 mrad are detectable by this method. A track is searched on the upstream part of vertex plate in the area defined by a cone around SB track with a opening angle, $\theta_{con} \sim 1/P_{SB}$ as shown in Figure (4.6). If a track, in the cone, with a minimal distance, \mathbf{d} , with respect to SB is found, it is referred to as parent track and kept for scanning. A cut is applied on the minimal distance, \mathbf{d} in order to reduce fake parent candidates. The applied cut was different for run1 and run2 data. For 1994 and 1995 data where angle and position resolutions are 5 mrad and 3 μm respectively, the cut: $d < 15\mu\text{m}$ is applied. For 1996 and 1997 data where angle and position resolution are 3 mrad and 1 μm respectively, the cut: $d < 9\mu\text{m}$ is applied without losing efficiency.

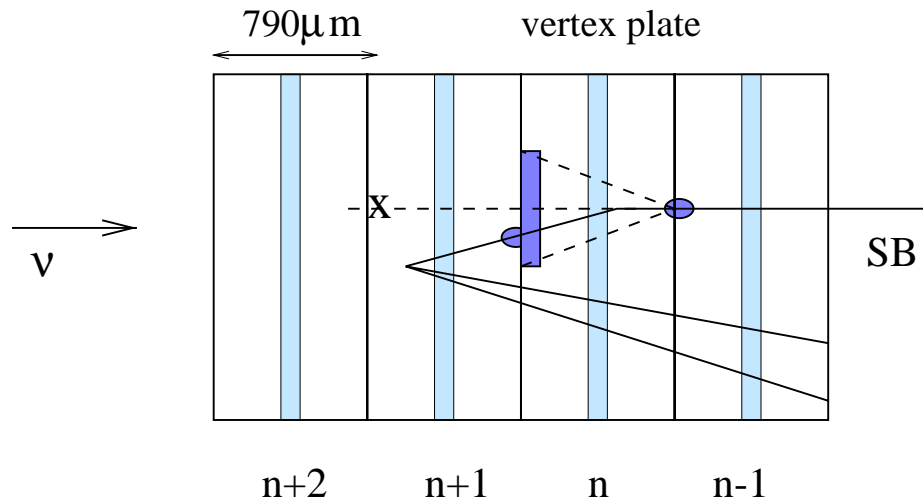


Figure 4.6: Parent search

4.3.8 Method IV

This is the Vertex Scan Back Location method and it is applied to 70 % of the 1995 1μ data and to 75 % of 1996 and 1997 1μ and 0μ data. This method is sensitive to short decays. After event location, all other tracks which are reconstructed in the fiber tracker are searched for in the vertex plate. If tracks are

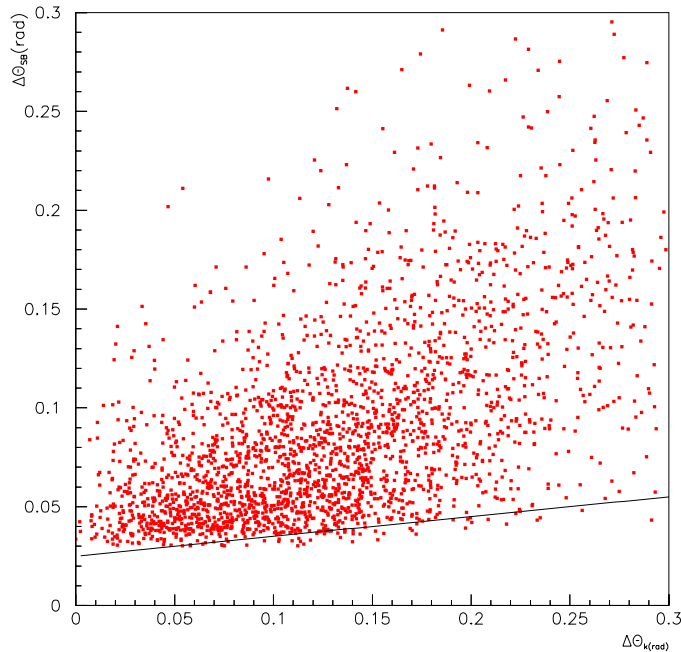


Figure 4.7: Kink angles above the line can be detected by eye.

detected, primary vertex position is calculated. A cut is applied on impact parameter (IP) between SB and vertex point in order to select potential τ^- candidates while rejecting ν_μ CC interactions. The applied IP cut is

$$IP > 4 + 0.012 \times dx \text{ } \mu\text{m}. \quad (4.2)$$

The events selected by this method are carefully checked by eye.

4.4 Decay Confirmation

For selected events by either of 4 the decay search methods, a computer assisted eye-check is performed in order to confirm the presence of the secondary vertex. About 8% of located events are selected for eye check. A decay topology is referred to as τ^- candidate if it satisfies the the following criteria:

- decay topology is a kink without black prongs, nuclear recoils, blobs or Auger electrons.

- transverse momentum of daughter particle with respect to parent particle direction is larger than 250 MeV/c (in order to reject decay of K/ π particles and secondary elastic hadron interactions, so called white kinks.)
- decay occurs within 5 plates downstream of neutrino interaction point. This 5 plates requirement is applied only for muonic decays. Due to different background sources, the decay is required to occur within 3 plates for 0μ channel.

The analyzed events in CHORUS are summarized in Table (4.1). No τ^- has been observed; therefore we conclude that the experiment does not show any evidence of $\nu_\mu \rightarrow \nu_\tau$ oscillation.

Table 4.1: Data flow chart

	1μ	0μ
Vertex predicted in emulsion	713,000	335,000
Selected events for scanning	477,600	122,400
Events scanned	355,395	85,211
Vertex Located	143,742	23,206
Eye-checked events	11,398	2,282

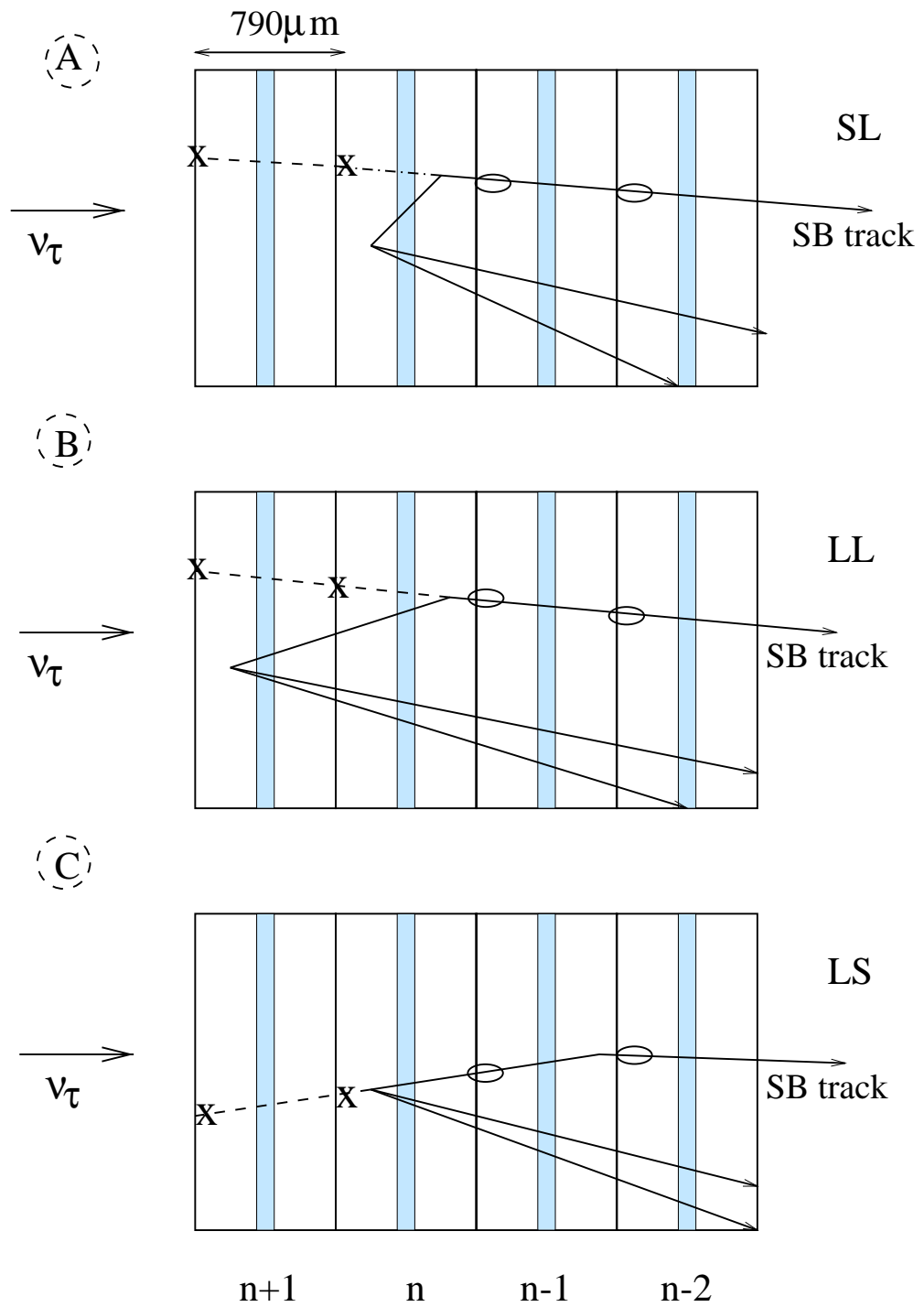


Figure 4.8: Decay types: a) short large type, b) Long Large type, c) Long small type.

4.5 Emulsion Scanning in Ankara

In Ankara emulsion scanning was began in the semi-automatic mode with mini plate geometry: Half module from 1994 run was divided into miniplates, with a dimensions $6 \times 6 \text{ cm}^2$. Then system is upgraded to work also in automatic mode. After upgrading the microscope, we received 4 half bulk modules (Figure (4.9) shows the place of Ankara emulsion in the bulk target) and corresponding interface sheets (CS periods 1 to 8 and 2 SS sheets). Systematic automatic emulsion scanning was started in 1998. We scanned CSs belonging to period 5 and 6. In these sheets 490 prediction were searched. The scanning results of these sheets are the following:

- Total number of predictions: 490
- Number of predictions with candidates: 404
- Number of predictions with good candidates ($\Delta\theta < 15 \text{ mrad}$): 372
- $\eta_{CS} = 0.76\%$
- Average speed: 5min./prediction.
- Average track multiplicity: 2.2/prediction

The scanning efficiency is comparable with Nagoya CS scanning efficiency. But scanning speed is much lower than Nagoya. The scanning of these two CS sheets took about 1.5 month. It was understood that it would not be possible to complete scanning on time with present system. In that case, there were two possibilities; a) upgrade the TS to NTS, or b) Perform the automatic scanning in Nagoya University (suggested by Prof. Dr. K. Niwa) and then do the final analysis in Ankara. Second possibility was chosen. Therefore the automatic scanning was performed in Nagoya (and some part in Utsonomiya). Interface sheets (CS and SS) and bulk modules; 28t, 68t, 68b were scanned in Nagoya University. Module 28b and corresponding SS were scanned in Utsonomiya University. Interface sheet

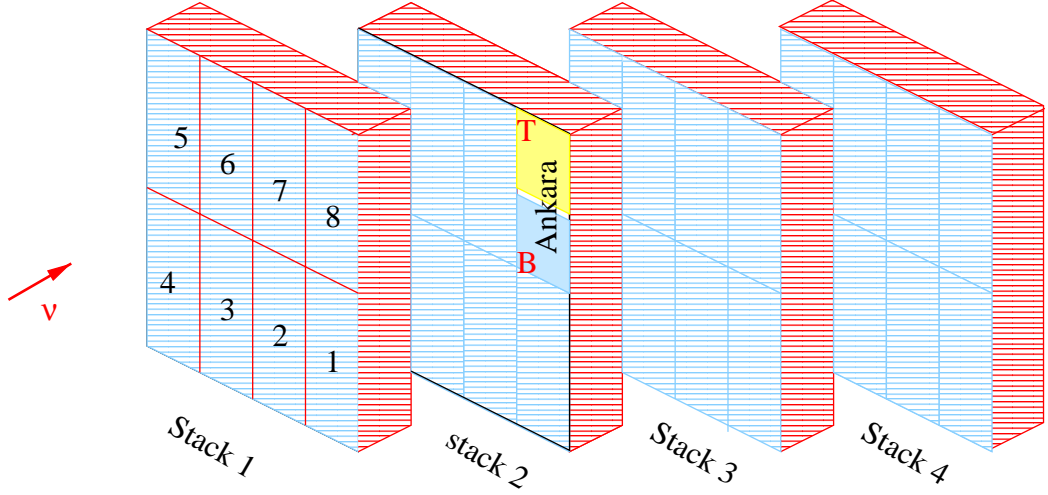


Figure 4.9: The analyzed modules in Ankara is 28B, 28T, 68B, 68T as shown in Figure.

scanning were performed according to 97 scanning strategy, explained in sections 4.3.1. and 4.3.2. Event location was done according to the procedure explained in section 4.3.3. The automatic scanning results can be summarized as:

- Total number of prediction for CS: 5251
- Total number of found events in CS: 4767
- Total number of found events in SS: 3731
- Total number of located events in bulk: 2460

Tables (4.2) and (4.3) show details of automatic scanning. After the event location bulk plates were brought back to Ankara to check located event candidates in bulk and to do final analysis. As explained before, after vertex location, automatic decay search scanning would have been performed. However, for Ankara emulsion we did not perform this scanning (which is done automatically) due to time limitation in Nagoya and did not get the corresponding reduction in numbers of located events in bulk. For all located events, a computer assisted manual check

Table 4.2: Scanning results of modules 28b, 28t (1994 data)

	28B			28T			Total		
	1μ	0μ	2μ	1μ	0μ	2μ	1μ	0μ	2μ
# of Prediction	819	198	22	699	166	11	1518	364	33
Searched in CS	812	196	22	693	166	11	1505	362	33
Found in CS	708	167	20	618	145	10	1326	312	30
Searched in SS	683	164	19	596	139	10	1279	303	29
Found in SS	477	116	14	461	105	9	938	221	23
Searched in Bulk	465	114	14	437	98	9	902	212	23
Found in Bulk	307	65	14	322	69	7	629	134	21
Eye-checked		64	14		69	7		134	21
Vertex found		43	11		55	7		98	18

has been performed on the Ankara microscope. The drawback of this method is increase of manual check load. On the other hand, this kind of study was very useful in order to check efficiency of the the other decay search methods, applied in other laboratories and to know vertex location efficiency better. Since decay search finding efficiency estimation is not an easy job, independent checks must be done with different methods.

Table 4.3: Scanning results of modules 68b, 68t (1995 data)

	68B			68T			Total		
	1μ	0μ	2μ	1μ	0μ	2μ	1μ	0μ	2μ
# of Prediction	1538	284	53	1201	222	38	2739	506	91
Searched in CS	1521	279	52	1181	220	37	2702	499	89
Found in CS	1413	262	51	1124	214	35	2537	476	86
Searched in SS	1382	260	51	1096	208	31	2478	468	82
Found in SS	1122	191	42	812	126	23	1934	317	65
Searched in Bulk	1002	188	40	717	122	19	1719	310	59
Found in Bulk	792	127	30	622	91	14	1414	218	44
Eye-checked	792	127	28		90	14	792	217	42
Vertex found	732	120	26		81	14	732	201	40

Eye-scan of located events in the modules 68b, 68t and 28t have been completed. We have not seen any τ^- decay candidate until now. On the other hand, some interesting decays have been seen in these modules. We have seen 3 kink, 1 Vee, 2 trident, 1 4vee decay topologies during eye-check. The preliminary analysis of these events has been done (see appendix A).

Table 4.4: Track finding efficiencies.

Efficiency	1μ	0μ	2μ
ε_{CS}	0.94	0.92	0.94
ε_{SS}	0.76	0.69	0.79
$\varepsilon_{\text{bulk}}$	0.78	0.67	0.79
ε_{eye}	0.92	0.85	0.92
ε_{loc}	0.56	0.42	0.59

The following procedure have been applied during eye-check;

- First the predicted plate is checked to see if the kink exists or not; if SB track and vertex are found in that plate, we complete the event-sheet by doing the necessary measurements.
- If the SB is "passing through" the predicted plate, it is followed in 5 (for 1μ sample) or 3 (for 0μ sample) plates if the measured angle is different from the SS measured angle.
- if the SB is not found in the predicted plate, the previous plate is checked.

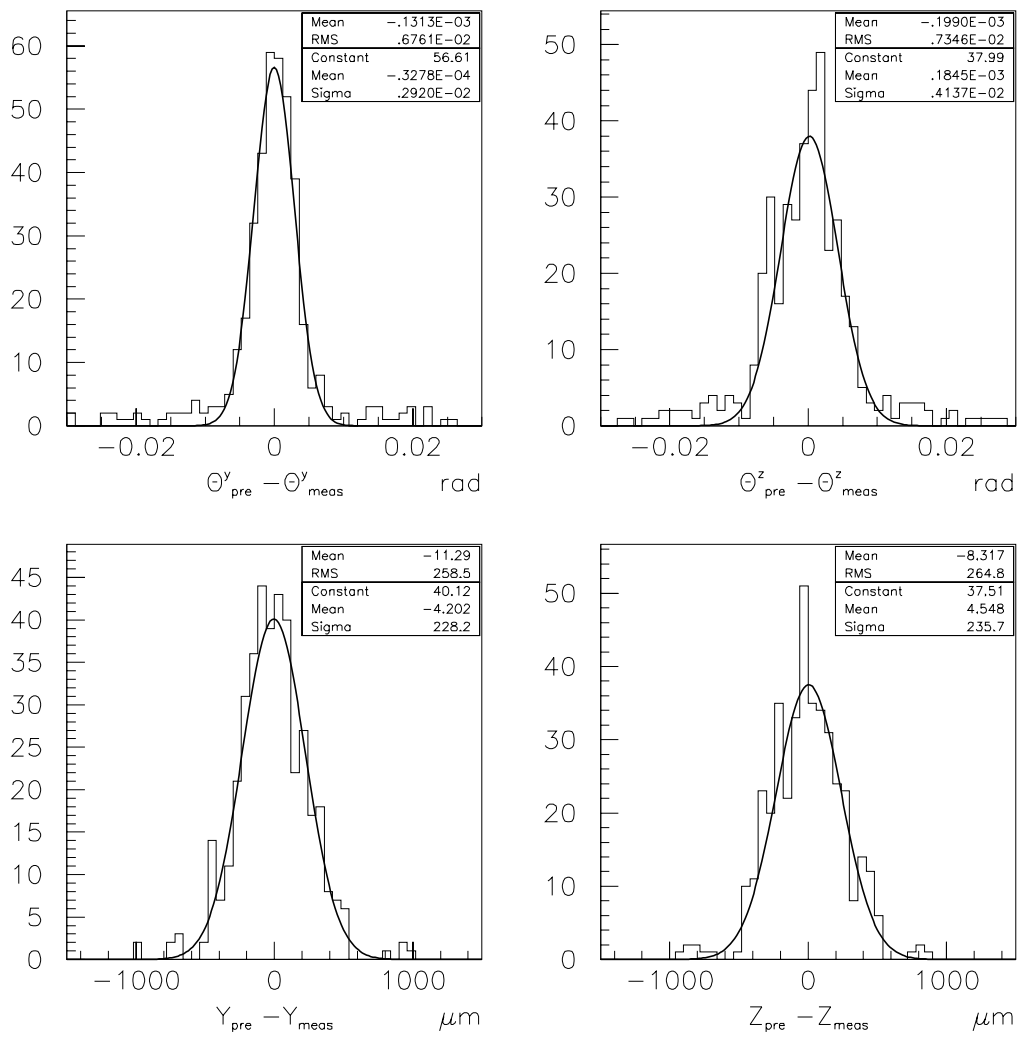


Figure 4.10: Top: measured-predicted CS angle in y and z. Bottom: measured-predicted CS angle in y and z (scanned in Ankara)

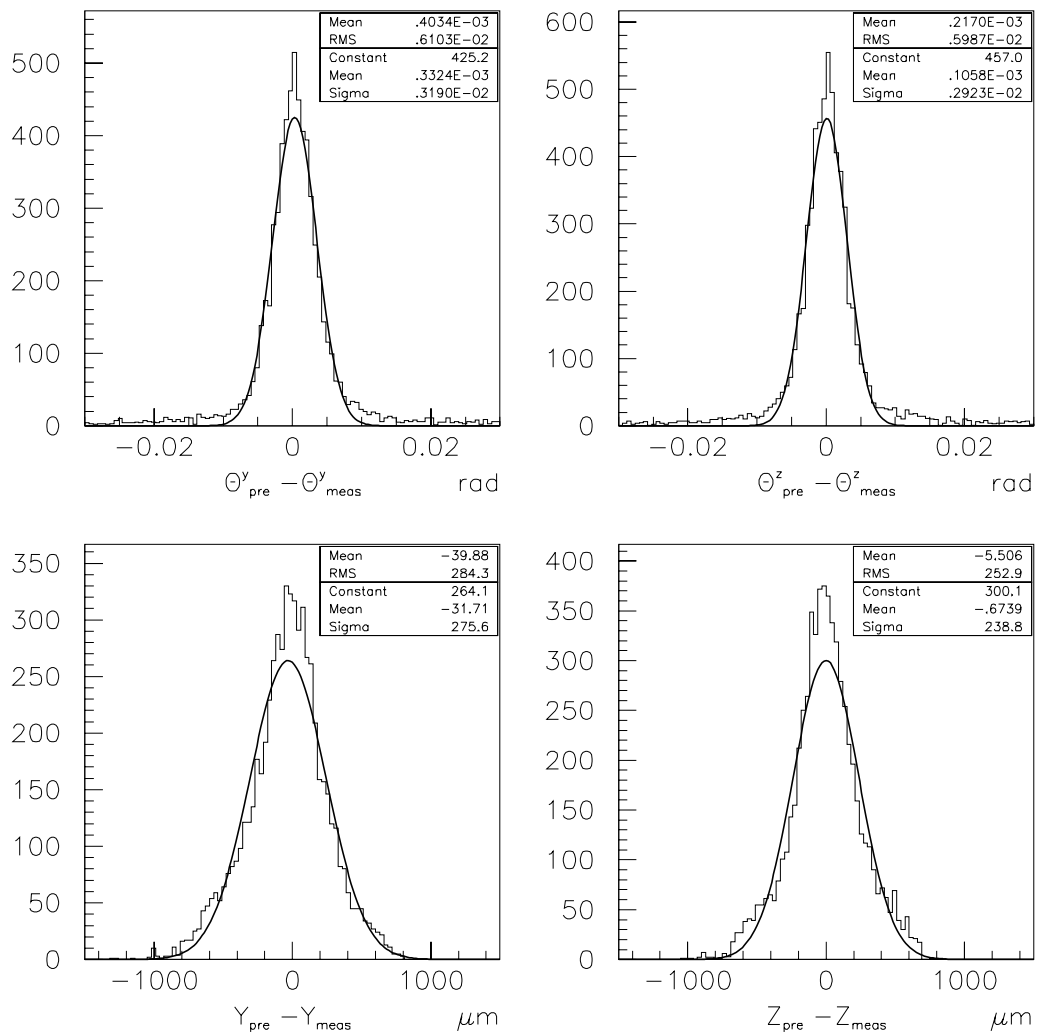


Figure 4.11: Top: measured-predicted CS angle in y and z. Bottom: measured-predicted CS angle in y and z (scanned in Nagoya Laboratory)

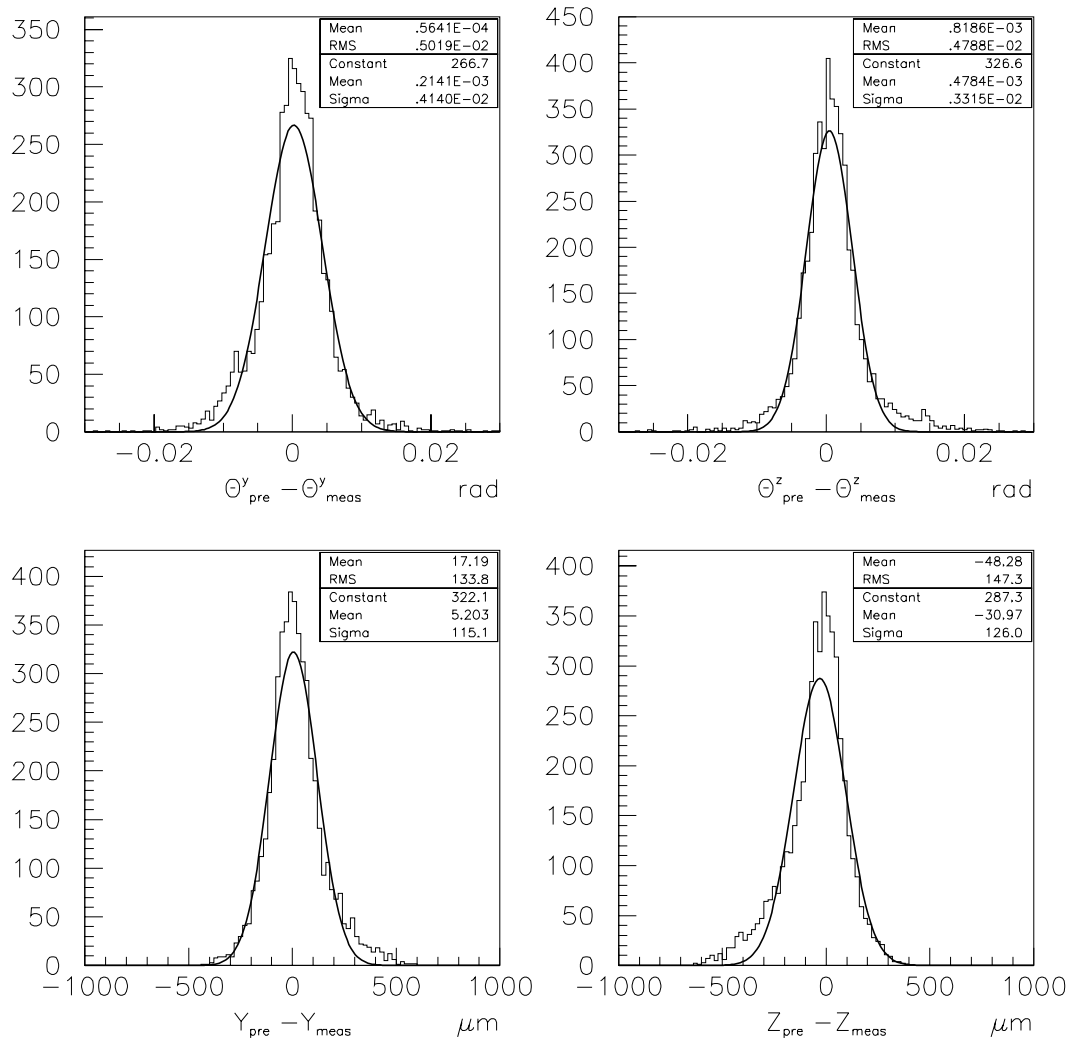


Figure 4.12: Top: measured-predicted SS angle in y and z. Bottom: measured-predicted SS angle in y and z (scanned in Nagoya Laboratory)

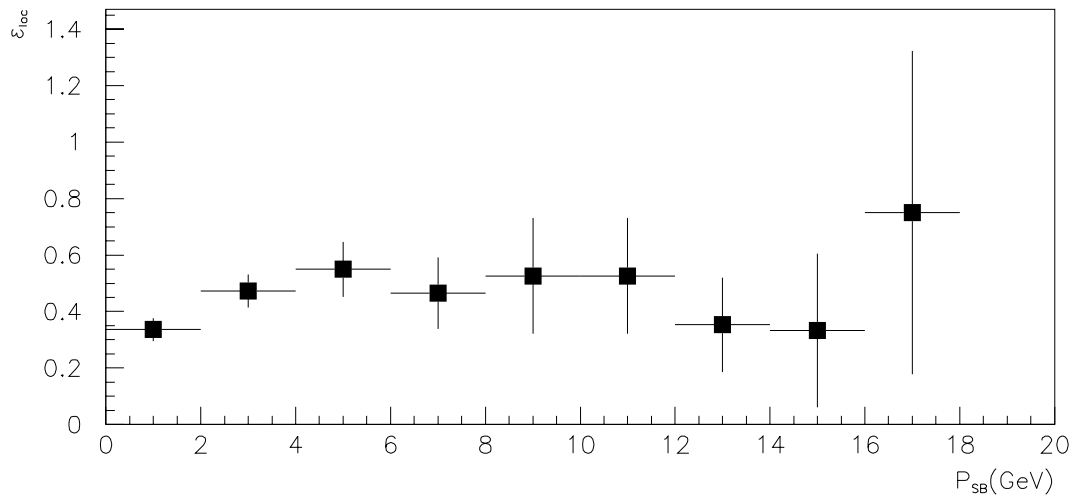
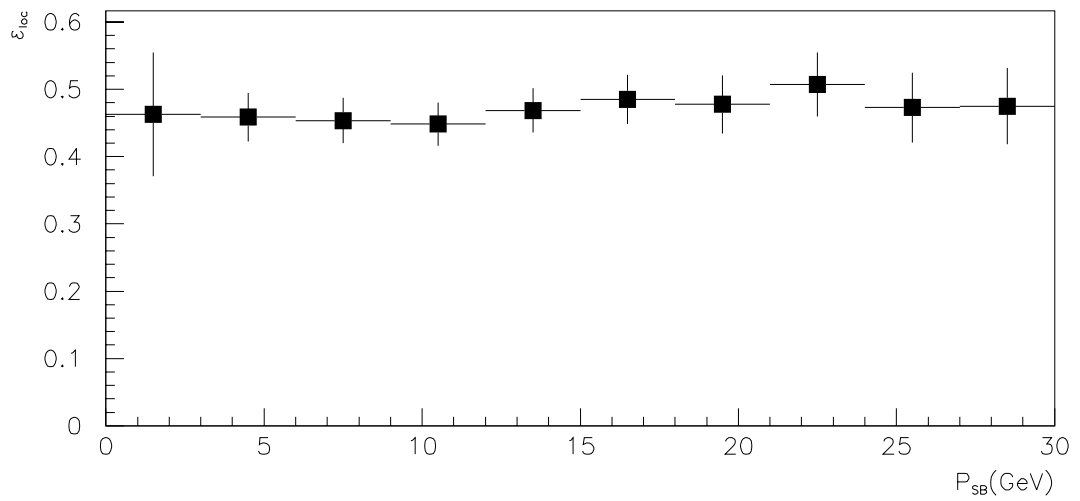


Figure 4.13: Plots show location efficiency versus SB momentum, top: 1μ sample, bottom: 0μ sample.

4.5.1 Monte Carlo Simulation

In this section, oscillation limit will be extracted by considering only the Ankara sample. As discussed in the previous section, we did not perform automatic decay search scanning for Ankara emulsion, but we checked every located event by eye using our computer assisted microscope. Therefore kink finding efficiency is different from the one computed for automatic decay search methods. Now, reconstruction acceptances and kink finding efficiencies will be computed by Monte Carlo simulation. MC samples, for $\nu_\mu CC$ and $\nu_\tau CC$ are used in order to simulate the results for the efficiencies.

In CHORUS MC events are generated by the following procedure;

- Neutrino beam files are generated by the MC simulation program GBEAM, based on FLUKA package. It generates the primary beam (proton) and lets them interact with the target (Be) to produce mesons which are tracked through decay tunnel to a decay vertex where a neutrino is created.
- Neutrino interactions are simulated with program JETTA and RESQUE [48] using neutrino beam files as input. JETTA produces a full set of particles that result from neutrino (3-flavours) interactions. It is based on LEPTO model for deep inelastic neutrino interactions. The Fermi motion of the nucleon is treated by using a simple Fermi gas model in which nucleons are considered as free fermions in a finite volume. The reinteractions of hadrons while crossing the nucleus are not taken into account. Hadronic fragmentation at primary vertex is accomplished according to LUND string model. The RESQUE package simulates quasi-elastic interactions and resonance production in neutrino scattering. Nuclear effects such as Fermi motion and Pauli suppression are taken into account, but not nuclear reinteractions.
- The simulated events are then passed to MC simulation program EFICASS (Emulsion FIBers CALorimeter and Spectrometer Simulation; based on GEANT 3.21) which simulate the response of the CHORUS detector. All

the primary tracks from the neutrino interactions in the target are traced through the entire apparatus taking into account all relevant physics processes. For every particle crossing the sensitive volume of a sub-detector, a response in the form of an electronic signal is computed. This part is specific to every detector and incorporates efficiencies, possible background, resolution and other parameters needed to simulate a reliable response. Agreement between the simulated data and real data for known processes is satisfactory. However some discrepancies may still exist. They are mostly due to the alignment problem and some unexpected effects.

- Finally, MC events are reconstructed with program CHORAL (CHorus Offline Reconstruction and Analysis Library). The first stage of tracking is performed in sub-detectors independently. Using track segments, reconstructed by space point (hits), track fitting is performed in sub-detectors. The fitted tracks are then extrapolated through the whole detector and re-fitting is performed.

4.5.2 Reconstruction Efficiency $1\mu^-$ Events

In order to simulate reconstruction efficiency of 1μ events, ν_μ CC and ν_τ CC (both simulated with EFICASS 1.10/22 and CHORAL 2.13/22) MC events are used. As a starting sample, events whose interaction vertex in the emulsion are taken. For these events the following conditions are required for them to be accepted as reconstructed in the electronic detector.

- Vertex must be located in the fiducial volume: in $-72 < Y, Z < 72$ cm.
- Vertex must be reconstructed in the correct stack : generated and reconstructed stacks must be matching.
- Event must be reconstructed as $1\mu^-$, that is a negative muon reconstructed in the fiber tracker. The applied cut is $\Delta\theta_{TT} < 3.44\sqrt{(0.00275)^2 + (0.01828.\theta_{sp})^2}$

where $\Delta\theta_{TT}$ is the difference between MC truth and reconstructed angles of the track and θ_{sp} is track space angle.

- Reconstructed muon momentum, P_{μ^-} , must be less than 30 GeV/c, if it is a calorimeter muon, or less than 28 GeV/c if it is reconstructed in the spectrometer.

The reconstruction efficiency, $\langle \mathbf{A}^{\mathbf{R}} \rangle$ for ν_{μ} CC and ν_{τ} CC($\tau^- \rightarrow \mu^-$) are evaluated as $49.8 \pm 0.3\%$ and $50.6 \pm 0.4\%$ respectively as shown in Table (4.5).

Table 4.5: Reconstruction efficiency of 1μ events.

	ν_{μ} CC	ν_{τ} CC($\tau^- \rightarrow \mu^-$)
Vertex in emulsion	28662	13069
Vertex in fiducial volume	25384	11661
Events reconstructed in correct Stack	24420	11026
1 μ event	21271	8783
μ^- reconstructed	19739	7822
$0 < P_{\mu} < 30$ GeV/c	14278	6619
$\langle \mathbf{A}^{\mathbf{R}} \rangle$	0.498 ± 0.003	0.506 ± 0.004

4.5.3 Reconstruction Efficiency $0\mu^-$ Events

Similar to $1\mu^-$ simulation, ν_{τ} CC interaction is used to simulate $0\mu^-$ reconstruction efficiency. Losses are due to following cuts;

- vertex must be located in the fiducial volume: in $-72 < Y, Z < 72$ cm.
- Vertex must be reconstructed in the correct emulsion stack : MC truth and reconstructed stack must be matching.
- Event must be reconstructed as 0μ in CHORAL (no muon in the event).
- There must be at least one $h^-(e)$ which is reconstructed by the Fiber Tracker, and satisfies the cut: $\Delta\theta_{TT} < 3.44\sqrt{(0.00275)^2 + (0.01828 \cdot \theta_{sp})^2}$.

- Track momentum, P , reconstructed by hexagonal magnet, must be between $1 < P_{h^-} < 20\text{GeV}/c$.

The reconstruction efficiency, $\langle \mathbf{A}^{\mathbf{R}} \rangle$ for **CC** ν_τ ($\tau \rightarrow \mathbf{h}^-$) and **CC** ν_τ ($\tau \rightarrow \mathbf{e}^-$) are evaluated as $24.9 \pm 0.2\%$ and $11.7 \pm 0.3\%$ respectively. as shown in Table (4.6).

Table 4.6: Reconstruction efficiency of 0μ events.

	$(\tau \rightarrow \mathbf{h}^-)$	$(\tau \rightarrow \mathbf{e}^-)$
Vertex in emulsion	30919	11788
Vertex in fiducial volume	27555	10502
Events reconstructed in correct Stack	23472	8727
0 μ event	22604	8503
μ^- reconstructed	8871	2254
$1 < P < 20$ GeV	7725	1383
$\langle \mathbf{A}^{\mathbf{R}} \rangle$	0.249 ± 0.002	0.117 ± 0.003

4.5.4 Scanning Efficiency

For scanning simulation, a reconstructed track whose angle is less than 400 mrad and larger than 50 mrad with respect to X7 beam direction, is extrapolated to CS from the fiber tracker. If there is a track inside a $1320 \times 990 \mu\text{m}^2$ centered around extrapolated point and its angle differs ($\Delta\theta$) by less than 15 mrad, the track is flagged as found. Track, found in CS, is then extrapolated to SS. it is flagged as found if it is inside $840 \times 630 \mu\text{m}^2$ and $\Delta\theta < 15$ mrad. Finally, we require vertex plate, $\text{pl} > 3$, since in the first 3 plate vertex reconstruction is not performed as explained before. Tables (4.7) and (4.8) show scanning simulation results for 1μ and 0μ events respectively.

Table 4.7: Scanning efficiency of 1μ events.

	CC ν_μ	CC $\nu_\tau (\tau \rightarrow \mu^-)$
Event reconstructed	14278	6619
Selected for CS scanning	12517	6134
SB found in CS	10397	4928
SB found in SS	10397	4662
Event located	9459	4380
$\langle A^S \rangle$	0.662 ± 0.004	0.662 ± 0.006

Table 4.8: Scanning efficiency of 0μ events.

	CC $\nu_\tau (\tau \rightarrow h^-)$	CC $\nu_\tau (\tau \rightarrow e^-)$
Event reconstructed	7725	1383
Selected for CS scanning	7282	1302
SB found in CS	5149	393
SB found in SS	4925	328
Event located	4488	273
$\langle A^S \rangle$	0.581 ± 0.007	0.197 ± 0.011

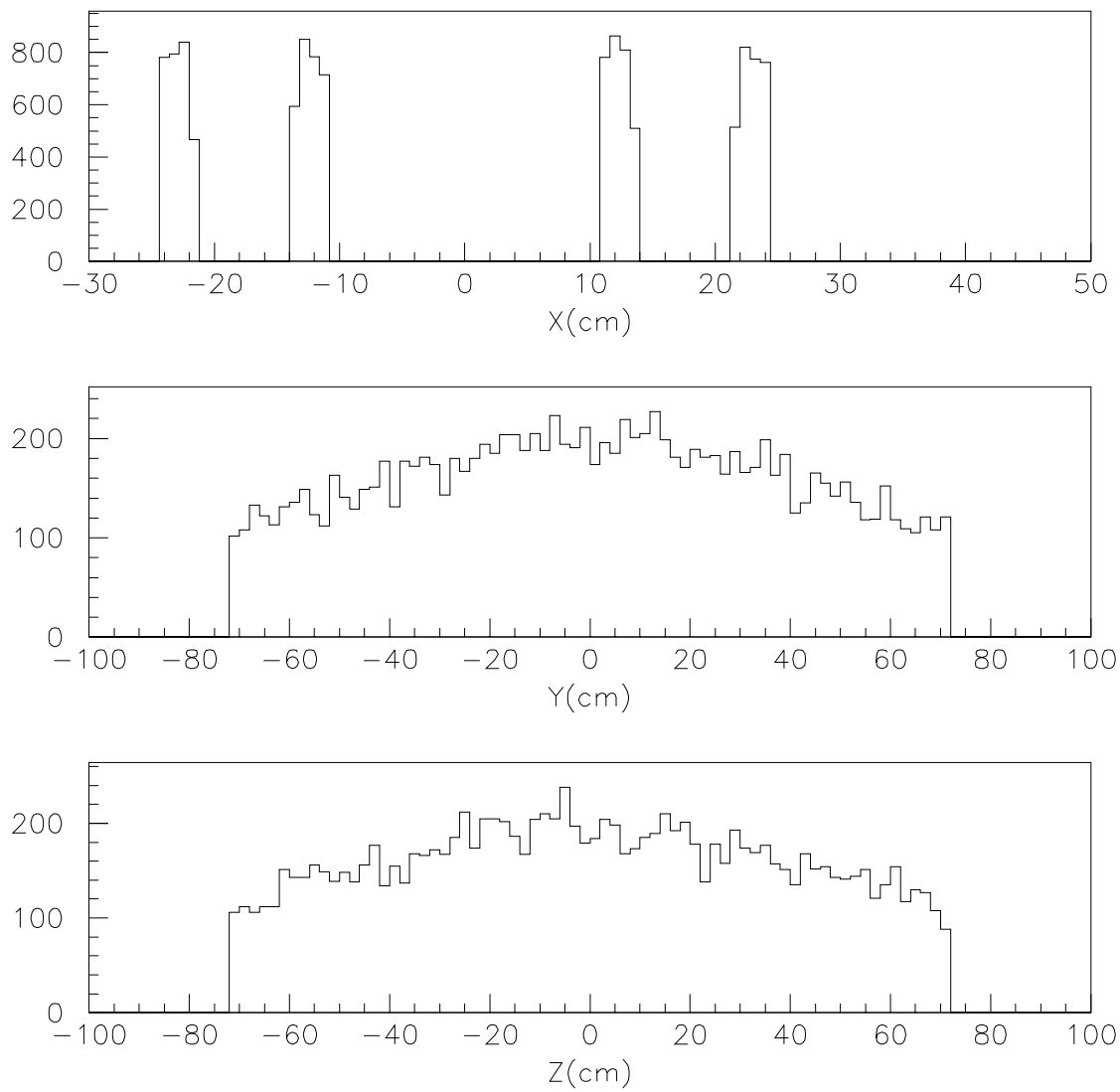


Figure 4.14: Vertex position in the emulsion target from MC simulation.

4.6 Kink Finding Efficiency

The kink finding efficiency can be written as

$$\eta_{kink} = \eta_{loc} \times \eta_{pt} \times f(\text{scanning methods}) \quad (4.3)$$

where

- η_{loc} is location efficiency;
- η_{pt} is transverse momentum cut efficiency; applied cut is $P_T > 250 \text{ MeV}$, ($P_T = P \times \sin\theta_{kink}$), P is the reconstructed momentum, θ_{kink} is from MC truth.
- f(scanning method) reflects scanning method efficiency; $f = \eta_{SL} \times \eta_{man}^{SL} + \eta_{LHL} \times \eta_{man}^{LHL} + \eta_{LL} \times \eta_{man}^{LL}$

In our method "f" reflects manual scanning efficiency. η_i (i= SL,LHL, LL) is the relative percentage of decays which are categorized according to lengths and kink angles. These definition are implemented in MC.

If the decay length of tau lepton is too short or too long it is not detected. Therefore, the following cuts are applied on flight length.

- primary vertex and decay vertex are in the same stack.
- flight length is not too long; $L_{decay} < 5 \text{ Plates}$
- flight length is not too short; $L_{decay} > 20 \mu m$.

To compute manual scanning efficiency, we define dead zones in which decay is not seen by eye. A kink is missed if it is in following places: decay vertex in the base or in a depth of $20 \mu m$ from the downstream surface of the base and primary vertex is in the base or in a depth of $20 \mu m$ from upstream surface of the base; decay vertex in a depth of $20 \mu m$ from upstream surface of emulsion plate and primary vertex is in a depth of $20 \mu m$ from downstream surface of emulsion plate.

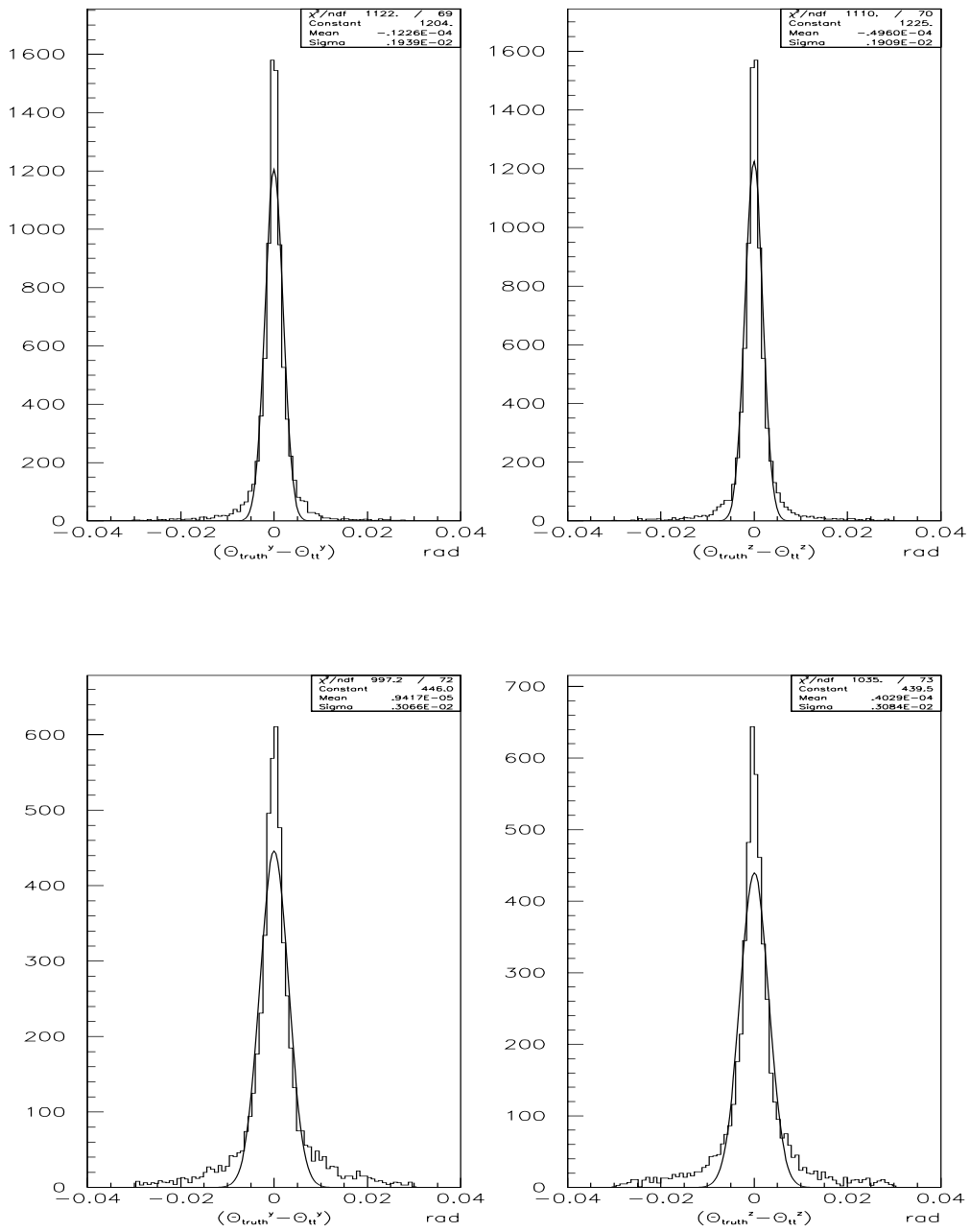


Figure 4.15: Angle difference between MC truth and TT reconstructed track for 1 μ (top) and 0 μ (bottom) events.

If the kink angle is too small, it is not easy to see. Therefore, we apply a scanback-angle-dependent cut on the kink angle, $\theta_{kink} > 0.1 \times \theta_{SB}$. This cut comes from scanning experience.

Table 4.9: Kink finding efficiencies

	CC $\nu_\tau (\tau \rightarrow \mu^-)$	CC $\nu_\tau (\tau \rightarrow \mathbf{h}^-)$	CC $\nu_\tau (\tau \rightarrow \mathbf{e}^-)$
η_{loc}	0.88	0.85	0.82
η_{pt}	0.91	0.66	0.39
η_μ	0.90		
η_{SL}	0.16	0.17	0.16
η_{LHL}	0.09	0.10	0.10
η_{LL}	0.48	0.52	0.53
η_{MSL}	0.991	0.992	0.983
η_{MLHL}	0.993	0.994	1.00
η_{MLL}	0.991	0.994	1.00
η_{kink}	0.52	0.44	0.25

4.7 Computation of Δm^2 Dependence of $\sin^2 2\theta$

To compute the excluded region in Δm^2 and $\sin^2 2\theta$ parameter space in the case of no signal event, Δm^2 dependence of $\sin^2 2\theta$ must be known. In this part this dependence will be obtained. Most of the systematic errors will be cancelled if we express the oscillation probability in terms of observed ratio of ν_τ to ν_μ events.

The total number of observed ν_μ CC interactions is given by

$$N_\mu = \int \Phi(E, L) \sigma_\mu(E) A_\mu(E) dE dL \quad (4.4)$$

If oscillation exist, observed total number of ν_τ interaction will be

$$N_\tau = \int \Phi(E, L) P(E, L) \sigma_\tau(E) A_\tau(E) \eta_{kink} Br(\tau \rightarrow spr) dE dL \quad (4.5)$$

where

- $P = \sin^2 2\theta \sin^2\left(\frac{1.27\Delta m^2 L}{E}\right)$ is oscillation probability for two flavor case; the average value of L and E are 0.6 km and 27 GeV respectively;
- Φ is ν flux;
- σ is cross section;
- A is reconstruction acceptance;
- η_{kink} is kink finding efficiency;
- $Br(\tau \rightarrow spr)$ is branching ratio (spr:single prong):

$$Br(\tau^- \rightarrow \mu^- \bar{\nu}_\mu \nu_\tau) : 17.8\%$$

$$Br(\tau^- \rightarrow e^- \bar{\nu}_e \nu_\tau) : 17.4\%$$

$$Br(\tau^- \rightarrow h^-(n\pi^0)\nu_\tau) : 49.5\%.$$

We can rearrange Eq.(4.5) as

$$N_\tau = \sin^2 2\theta Br(\tau \rightarrow spr) \int \phi(E) \sigma_\tau(E) P'(E) A_\tau(E) \eta_{kink} dE \quad (4.6)$$

where $\sin^2 2\theta \int \phi(E) P'(E) dE = \int \Phi(E, L) P(E, L) dE dL$. Eq.(4.6) can be written in terms of weighted values.

$$N_\tau = \sin^2 2\theta Br(\tau \rightarrow spr) \int \phi dE \frac{\int \phi P' dE}{\int \phi dE} \frac{\int \phi \sigma P' dE}{\int \phi P' dE} \frac{\int \phi \sigma P' A dE}{\int \phi \sigma P' dE} \frac{\int \phi \sigma P' A \eta_{kink} dE}{\int \phi \sigma P' A dE}$$

or

$$N_\tau = \sin^2 2\theta Br(\tau \rightarrow spr) \Phi \langle P \rangle \langle \sigma_\tau \rangle \langle A \rangle \langle \eta_{kink} \rangle \quad (4.7)$$

What is useful is the ratio of N_τ and N_μ so,

$$\frac{N_\tau}{N_\mu} = \sin^2 2\theta Br(\tau \rightarrow spr) \frac{\Phi \langle P' \rangle \langle \sigma_\tau \rangle \langle A_\tau \rangle \langle \eta_{kink} \rangle}{\Phi \langle \sigma_\mu \rangle \langle A_\mu \rangle} \quad (4.8)$$

At large Δm^2 , $\langle P' \rangle \rightarrow \frac{1}{2}$. Then Eq.(4.8) becomes

$$\frac{N_\tau}{N_\mu} = \frac{1}{2} \sin^2 2\theta Br(\tau \rightarrow spr) \langle \eta_{kink} \rangle \frac{\langle \sigma_\tau \rangle \langle A_\tau \rangle}{\langle \sigma_\mu \rangle \langle A_\mu \rangle} \quad (4.9)$$

or

$$N_\tau = \frac{\langle \sigma_\tau \rangle N_\mu}{\langle \sigma_\mu \rangle \langle A_\mu \rangle} > \frac{1}{2} \sin^2 2\theta [Br(\tau \rightarrow \mu X) \langle A_{\tau\mu} \rangle \eta_\mu + Br(\tau \rightarrow hX) \langle A_{\tau h} \rangle \eta_h] \quad (4.10)$$

where

- $\langle \sigma \rangle$ is flux weighted cross section;
- $\langle A \rangle$ is flux and cross section weighted acceptance;
- $\langle \eta_{kink} \rangle$ is flux, cross section and acceptance weighted kink finding efficiency.

In order to obtain a relation between Δm^2 and $\sin^2 2\theta$, Eqs.(4.4) and (4.5) can be combined in the following way,

$$\frac{N_\tau}{N_\mu} = \sin^2 2\theta Br(\tau \rightarrow spr) \frac{\int \Phi(E, L) \sigma_\tau(E) A_\tau(E) \eta_{kink} \sin^2\left(\frac{1.27 L \Delta m^2}{E}\right) dE dL}{\int \Phi(E, L) \sigma_\mu(E) A_\mu(E) dE dL} \quad (4.11)$$

Eq.(4.11) is reduced at large Δm^2 to

$$\frac{N_\tau}{N_\mu} = P'' Br(\tau \rightarrow spr) \frac{\int \Phi(E, L) \sigma_\tau(E) A_\tau(E) \eta_{kink} dE dL}{\int \Phi(E, L) \sigma_\mu(E) A_\mu(E) dE dL} \quad (4.12)$$

where $P'' = \frac{1}{2} \sin^2 2\theta^\infty$ is oscillation probability at large Δm^2 . Using Eqns. 4.11 and 4.12, we can compute Δm^2 dependence of $\sin^2 2\theta$ as

$$\sin^2 2\theta = \frac{1}{2} \sin^2 2\theta^\infty \frac{\int \Phi(E, L) \sigma_\tau(E) A_\tau(E) \eta_{kink} dE dL}{\int \Phi(E, L) \sigma_\tau(E) A_\tau(E) \eta_{kink} \sin^2\left(\frac{1.27 L \Delta m^2}{E}\right) dE dL} \quad (4.13)$$

To compute exclusion region in the plane of $\sin^2 2\theta$ and Δm^2 , it is enough to know $\sin^2 2\theta^\infty$ and energy dependence of efficiencies, flux and cross sections.

4.7.1 Systematic Errors

The systematic uncertainty on Eq.(4.9) is due to

- Uncertainty on the cross section ratio, $\frac{\langle \sigma_\tau \rangle}{\langle \sigma_\mu \rangle}$: 10 %.
- Track selector pulse height cut : (+5, -10)%

- Uncertainty on momentum measurement in spectrometer : $\pm 5\%$
- Uncertainty on MC statistics: $\pm 1\%$ and reliability $\pm 5\%$

Over all systematic error on Eq.(4.9) is estimated as 16%

4.8 Background Sources

The following sources can give rise to background for the signal (τ^- decay.).

- **Prompt ν_τ CC interaction:** This is common background to both 1μ and 0μ channels. The expected number of background events due to this source is estimated as $\sim \frac{10^{-6}}{\nu_{\mu int.}}$. Therefore it is negligible for the present sample.
- **Negative charm meson production in $\bar{\nu}_\mu$ ($\sim 5\%$ in the ν beam) CC interaction:** These events constitute background to 1μ channel if primary vertex μ^+ or e^+ is not identified. Number of background from this process is estimated as $\sim \frac{10^{-7}}{\nu_{int.}}$ for 1μ and 0μ channels.
- **Positive charm meson production in ν CC interaction:** If the primary vertex lepton is not identified and charge of the charmed particle daughter is incorrectly measured, these events are background to τ^- decay. The expected number in 0μ and 1μ samples are $\sim \frac{10^{-5}}{\nu_{\mu CC}}$ and $\sim \frac{10^{-7}}{\nu_{\mu NC}}$ respectively.
- **The associated charm production both in CC and NC interactions:** An event from this source will be a background event if one of the charmed particles is not detected and, for CC interaction, primary vertex lepton is not identified. The expected background due to this source is also negligible. It is estimated as $\sim \frac{10^{-8}}{\nu_{int.}}$.
- **Elastic interaction of a hadron with nuclei :** This type of scattering is called "White Kink", if there is no black or grey track, blobs or Auger electron at the kink point. Background from this source is not negligible for the 0μ sample. However it is possible to kill this background by applying

appropriate kinematical cuts. In our sample there are no decay candidates whose P_T is larger than 250 MeV/c.

Table 4.10: Estimated acceptance and kink finding efficiency for each decay mode

	$\tau \rightarrow \mu^-$	$\tau \rightarrow \mathbf{h}^-$	$\tau \rightarrow \mathbf{e}^-$	$\nu_\mu \mathbf{CC}$
$\langle \mathbf{A}_i \rangle$	0.33	0.14	0.023	0.33
$\frac{\langle \mathbf{A}_{\tau i} \rangle}{\langle \mathbf{A}_{\nu_\mu} \rangle}$	1.00	0.44	0.070	1.00
$\eta_{\tau i}$	0.52	0.44	0.25	

4.9 A Limit on $\nu_\mu \rightarrow \nu_\tau$ Oscillation

In absence of a signal, we can compute a limit on oscillation at a chosen confidence limit, C.L. replacing N_τ by the upper limit on the number of signal events. We have not seen any candidate event. Therefore we can compute a limit on the $\nu_\mu \rightarrow \nu_\tau$ oscillation as follows. In the case of no signal Eq.(4.9) is reduced to

$$\frac{2.37}{N_\mu} = \sin^2 2\theta_{\mu\tau} P_{\mu\tau} \frac{\langle \sigma_\tau \rangle \langle A_\tau \rangle}{\langle \sigma_\mu \rangle \langle A_\mu \rangle} \eta_{\tau i} Br(\tau \rightarrow spr_i) \quad (4.14)$$

or

$$P_{\mu\tau} \leq \frac{2.37 \cdot \frac{\langle \sigma_\mu \rangle \langle A_\mu \rangle}{\langle \sigma_\tau \rangle \langle A_\tau \rangle}}{BR(\tau \rightarrow spr). N_i \cdot \eta_{\tau i}} \quad (4.15)$$

at 90 % C.L. and large Δm^2 . The factor 2.37 takes into account 16 % systematic uncertainty. Using the numbers in Tables (4.9), (4.10) and (4.11) we can obtain a limit on the oscillation probability. To allow an easy combination of the results from 1μ and 0μ event samples; it is useful to define the "equivalent number of muonic events" of the 0μ sample using Eq.(4.10)

$$N^{eq} = N_{0\mu} \Sigma_i \frac{\langle A_{\tau i} \rangle}{\langle A_{\tau\mu} \rangle} \frac{BR(\tau \rightarrow i)}{BR(\tau \rightarrow \mu)} \frac{\langle \eta_{\tau i} \rangle}{\langle \eta_{\tau\mu} \rangle} \quad (4.16)$$

Table 4.11: Quantities used in estimation of limit on oscillation probability

	$\mathbf{1}\mu$	$\mathbf{0}\mu$
$N_{\mathbf{loc}}$	792	352
$\frac{\sigma_{\tau}}{\sigma_{\mu}}$	0.53	0.53
$\mathbf{Br}(\tau \rightarrow \mathbf{i})$	0.18	0.50

Using numbers in Tables (4.9), (4.10) and (4.11) we get oscillation probability,

$$P_{\tau\mu} \leq 1.14 \cdot 10^{-2} \quad (4.17)$$

On the other hand if we analyzed all the located events in CHORUS in the same way as we have done as in Ankara, CHORUS limit on oscillation probability will be

$$P_{\tau\mu} \leq 7.9 \cdot 10^{-5} \quad (4.18)$$

at 90 % C.L., and at large Δm^2 . In a two flavour mixing scheme at 90 % C.L. the excluded region in the $(\sin^2 2\theta, \Delta m^2)$ parameter space is shown in Figure (4.16).

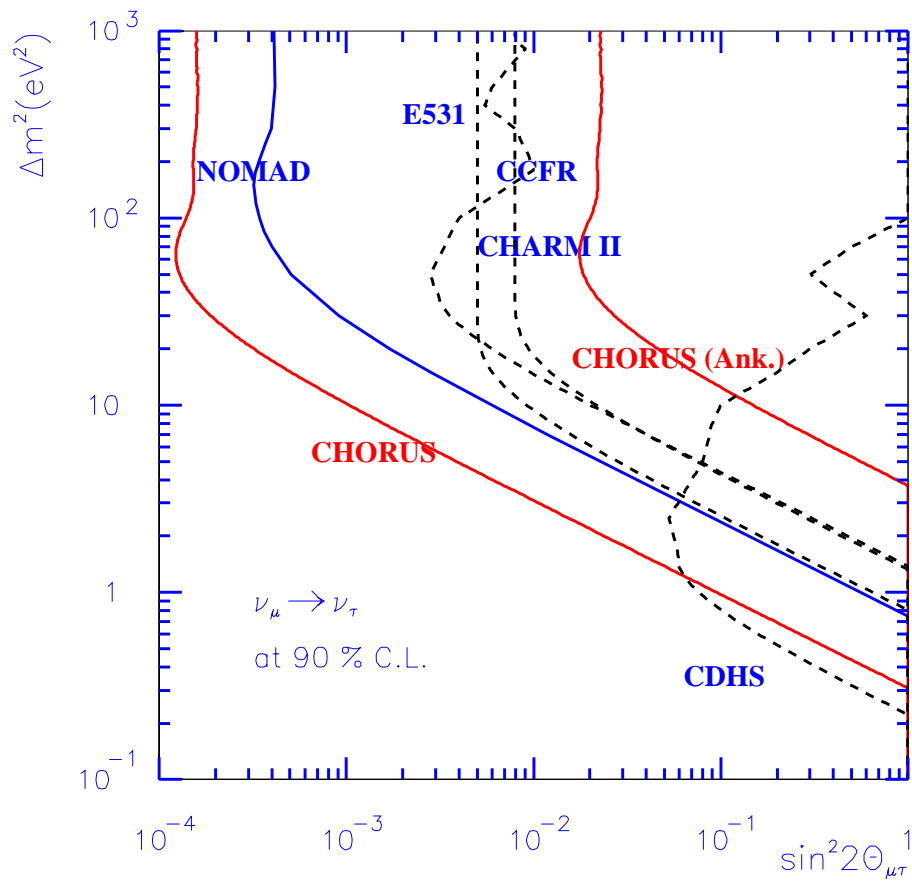


Figure 4.16: Limit on $\nu_\mu \rightarrow \nu_\tau$ obtained using data scanned in Ankara (right) (we would get the limit (most left) if all data were analyzed in the same way as in Ankara)

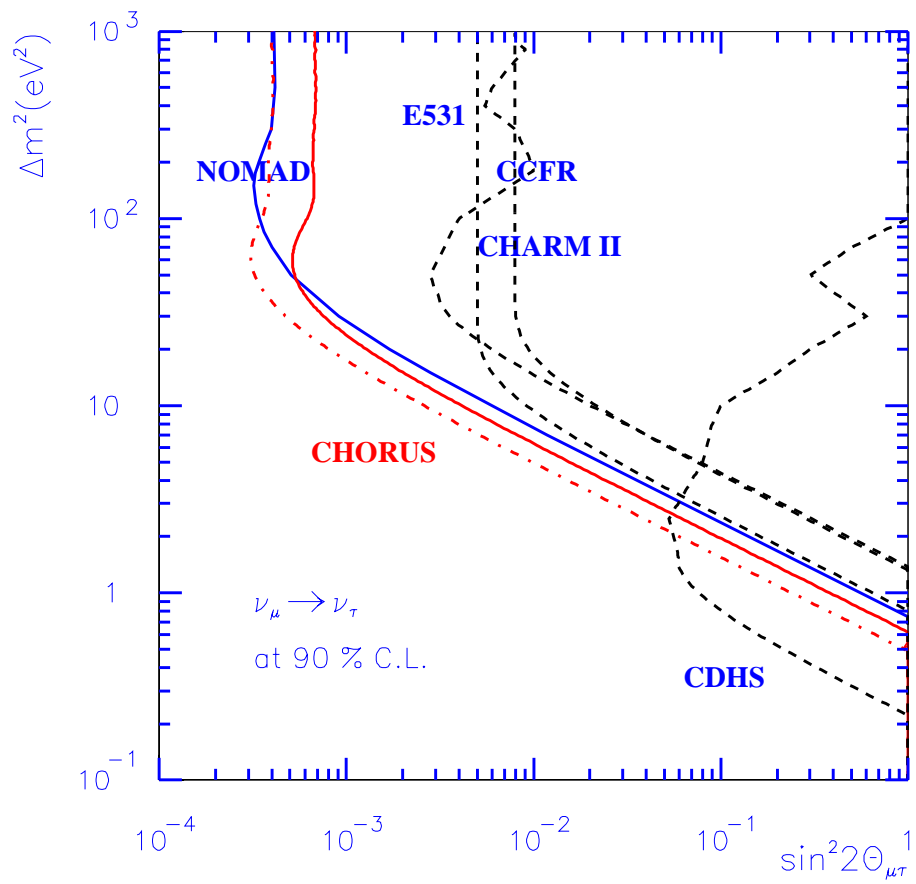


Figure 4.17: Present limit of CHORUS on $\nu_\mu \rightarrow \nu_\tau$ oscillation

CHAPTER 5

D^0 PRODUCTION RATE MEASUREMENT IN NEUTRINO INTERACTIONS

In recent years, high statistics and high resolution experiments has turned charm quark physics into precision physics.

Most of the data on charmed particle production by neutrinos has been obtained using large neutrino detectors. Usually the decay of a charmed particle is not seen directly, its presence is inferred from the observation of strange particles or final state leptons. This requires large background subtractions. Major advantages of emulsion experiments are the ability to fully reconstruct event kinematics. This suppresses the large background that comes from the decays of kaons and pions. On the other hand there is a disadvantage: low statistics due to scanning load. Recent improvements in scanning systems and methods which have been done in Nagoya University, solved this problem.

By fast automatic microscopes and a new scanning method, CHORUS experiment is turned into a high statistics experiment for charm physics.

5.1 CHORUS Phase II Analysis

In the CHORUS experiment Phase I analysis, explained in the previous chapter, is recently completed; and a second phase more thorough analysis has been started with a new scanning and analysis method which will be explained in the following sections.

5.2 Net Scanning

Net Scanning is a new method for event location and decay search in emulsion, developed in Nagoya University.

Main principle of Net Scanning is to pick up all track segments in the fiducial volume corresponding to every prediction. In order to perform this kind of scanning, one needs very fast microscope. The latest generation of track selector (UTS) makes this possible. All track segments, in the angular acceptance ($-0.4 < \theta_{y,z} < 0.4$ rad) and in one view ($150 \times 120 \mu m^2$) are detected within 0.3 sec.

In phase I analysis we followed the track referred to as scan back track, (SB) until the vertex plate. This method is the so called "scan back location". In Net Scanning method we use this information: located events in Phase I as the prediction for Net Scanning.

As shown in Figure (5.3), Net Scanning fiducial volume is $1.5 \times 1.5 \times 6.32$ (8 plates) = 14.22 mm^3 centered about the SB track position. Starting from vertex plate, 6 plates downstream and one plate upstream are scanned. The angular acceptance is set to $-0.4 < \theta_{y,z} < 0.4$ rad. All the events between plates 3 and 36 are Net-Scanned. The speed of Net Scanning is about 1560 event /month/UTS.

Plate by plate all segments (applied pulse height cut is 10) in the fiducial area are picked up. Output of this scanning contains all segment informations (slopes, positions in CHORUS coordinates, pulse height etc.). Using three dimensional position coordinates and angle information of segments, tracks are reconstructed. Tracking and vertex reconstruction involve a number of steps. First step is to run offline reconstruction programs; ecfosal 2.3 and ecvtxa 2.0, written by S. Aoki and K. Komatsu respectively.

In the following sections we explain the main steps of tracking and vertex reconstruction.

5.2.1 Alignment and Tracking

After Net Scanning, off-line reconstruction program, `ecfsal 2.3` is run in order to perform tracking. The position and slope of all segments are transformed into aligned coordinates using off-set from global alignment of plate. The main steps of this process are following:

- First, segment selection for tracking is done, with the requirement that pulse height must be bigger than 12. If distance between two segments is less than $5 \mu\text{m}$ one of them is killed (ghost cancellation).
- After first level selection, plate by plate alignment is done. This includes rotation between plates, gap, position and angle shift corrections using angle and position informations of all tracks. Then tracking is performed as follow: track is extrapolated to next plate and one checks whether there is a candidate which matches with extrapolated segment. If there is no candidate for matching in the extrapolated plate, it is kept in the sample and it is tried to find a match in one further upstream plate. Maximum cone angle around the extrapolated track is ~ 20 mrad and radius is $\sim 4 \mu\text{m}$. Output of this program gives all aligned track informations.

5.2.2 Fine Alignment and Vertex Reconstruction

5.2.2.1 Fine Alignment

After first level alignment and tracking the mean number of tracks in the fiducial area is about 5k. Almost 99% of this is background tracks i.e. low momentum tracks. Before vertex reconstruction this background must be reduced as much as possible since these fake tracks will generate fake vertices which increase the manual check load. We outline this procedure as following:

- Before vertex reconstruction, low momentum track rejection is done in "ecvtxa". This is done by opening a cone whose opening angle corresponds

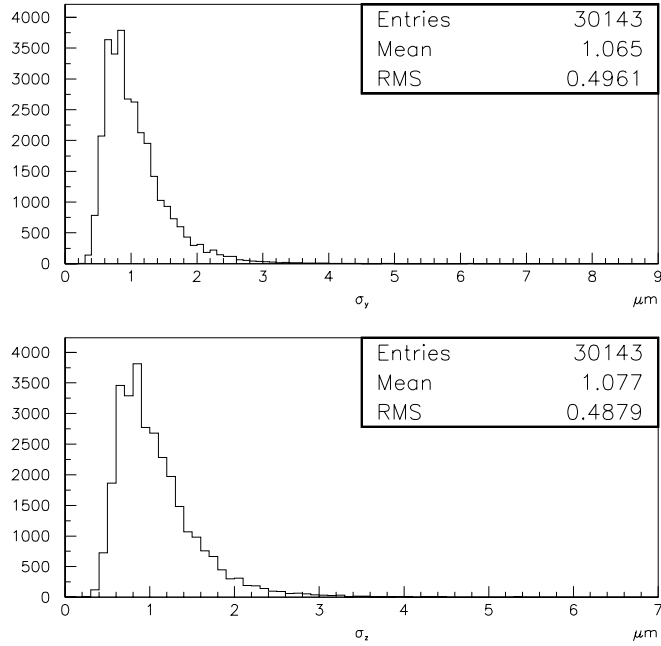


Figure 5.1: Residuals RMS distribution in position y and z .

to 100 MeV and searching for connectable segments from upstream and downstream. If a candidate is found, this track is rejected.

- After low momentum rejection, plate by plate fine alignment is done using position informations as free parameters. This is similar to first level alignment; position shift, angle shift, rotation between plates and gap corrections are done. Final tracks are chosen on the basis of their χ^2 value. These tracks (so called "good tracks") are sent to vertex reconstruction

Figures (5.1) and (5.2) show RMS distribution of residuals in position and slopes respectively after the fine alignment. After fine alignment RMS found for the position difference between a segment position and its track position is 0.5 μm and corresponding angle resolution is 2 mrad.

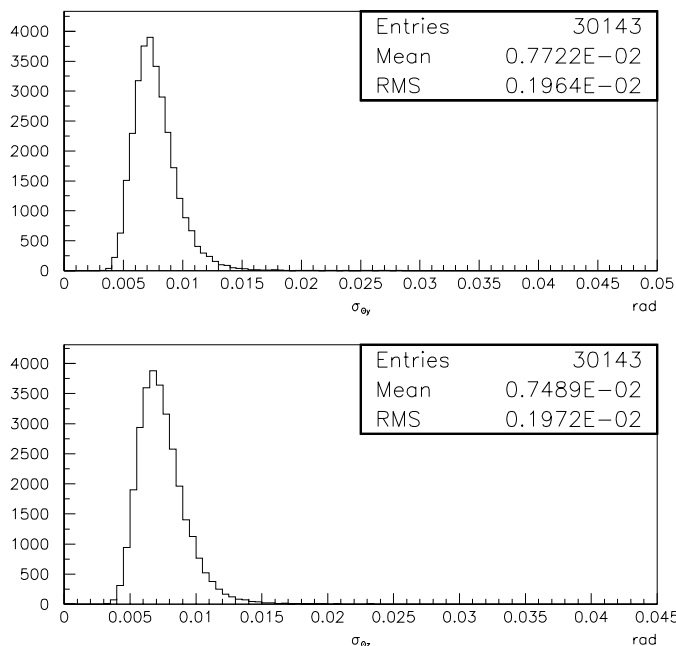


Figure 5.2: Residuals RMS distribution in slope y and z .

5.2.2.2 Vertex Reconstruction

After rejection of penetrating tracks through fiducial volume remaining tracks are considered for vertex location. Main parameters for vertex reconstruction are summarized in Table (5.1). These are runcard parameters so that they can be changed before processing.

Vertex reconstruction is done in two steps:

- First, two track vertices are reconstructed. Requirements are that each of the two tracks should be a "good track" (one segment TT matched tracks are also included in vertex reconstruction; but at least one track must be two plate connected) and stop in fiducial volume (no segment in one upstream plate) and impact parameter between two tracks must be smaller than $20\mu\text{m}$.
- After the reconstruction of two track vertices; clustering of vertices is done. The requirement is that the impact parameter between two tracks which

Table 5.1: Runcard parameters of "ecvtxa"

parameter	set value
Max. seg. for track fitting	3
Single Stop min. seg.	2
Number of miss from up	1
Number of miss from down	1
Two vertex IP.	20 μm
Min. cluster IP.	10 μm
TT match cut	30 mrad
χ^2 factor	2

form two track vertices must be smaller than 10 μm . Impact parameter between two track vertices must be bigger than 10 μm .

5.2.3 Selection for Charm Search

After vertex reconstruction we make selection for charm search. The mean number of stopping tracks which satisfy the "good track conditions" in fiducial volume is about 40 as shown in Figure (5.8). This sample still contains low momentum and passing through tracks. In order to select interesting events from this sample we do additional filtering of events using various cuts.

5.2.3.1 Selection A

This selection is based on impact parameter cut. First, "good tracks" are selected based on global angle difference that is angle difference of fitted track and track segments. Then impact parameter between track and vertex point is calculated. Tracks passing the impact parameter cut are checked by eye. Selection steps are the following:

- At least two TT matching tracks (one is at primary vertex the other is at decay vertex) must be reconstructed. TT-matched tracks must be at least

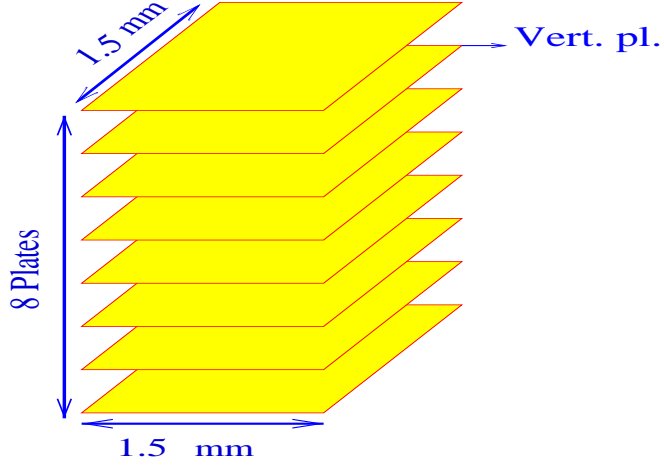


Figure 5.3: Fiducial volume for Net Scanning

2 plate connected. Applied cut for TT-matching is

$$\Delta\theta_{TT} < 3.44\sqrt{(0.00546)^2 + (0.0194\theta)^2}$$

at 99 % C.L. This requirement is necessary in order to have reasonable manual check load and also we have to be sure that neutral charm come from the right primary vertex.

- To reject low momentum tracks, we apply the following cut at 99 % C.L.:

$$\Delta\theta < 2.31\sqrt{(0.00367)^2 + (0.0236\theta)^2}$$

where $\Delta\theta$ is the angle difference between the global angle of the track and track segment angle measured in the last (and first) plate.

- A cut is applied on impact parameter between stopping track and vertex point.

$$IP > \sqrt{3^2 + (2\sigma_\theta dx)^2}$$

where dx is vertex depth and $\sigma_\theta = \sqrt{(0.00305)^2 + (0.0194\theta)^2}$

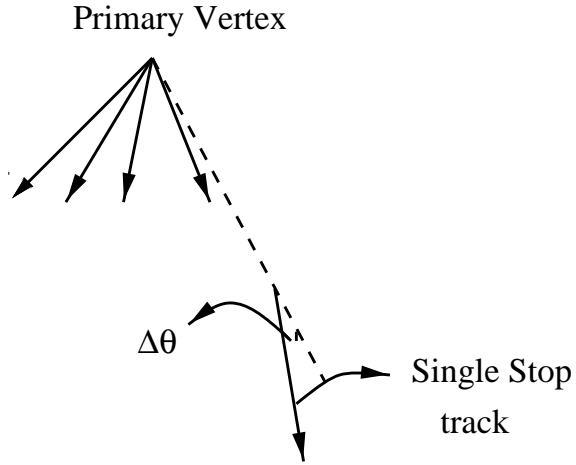


Figure 5.4: e-pair cut: $\Delta\theta > 10\text{mrad}$

- Finally, to kill electron pairs, minimum kink angle (shown in Figure (5.4)) cut is applied : $\Delta\theta_k > 10\text{mrad}$.

Single stopping tracks are checked by eye only if they pass all these criteria, listed above.

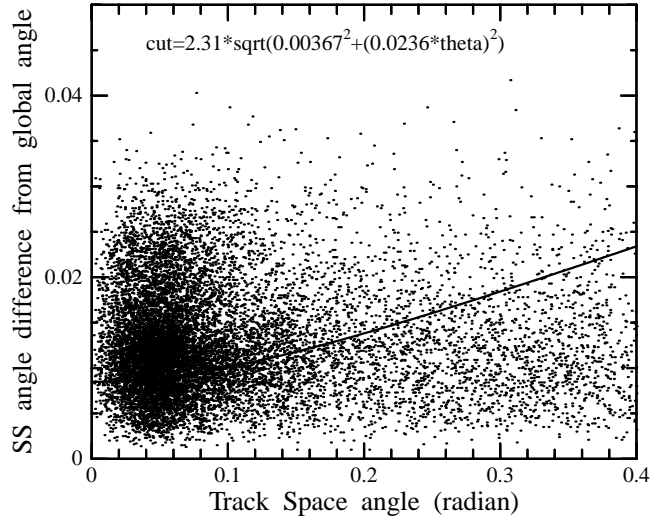
The mean number of tracks which stop in the fiducial volume is reduced to 2.4 (shown in Figure (5.9)) after selection.

5.2.3.2 Selection B

Since impact parameter allowance for two-track vertices and vertex clustering is $20\mu\text{m}$, some of the short decays are not caught by this selection.

In order to recover the short decays a new selection is done using all connected tracks. The minimum distance, d_{min} , between muon track and other reconstructed tracks are calculated (Figure (5.7) shows d_{min} distribution) and a cut on d_{min} is applied in order to hunt these decay topologies. We can summarize selection criteria as

Single Stop tracks (= 2 segments)



Single Stop tracks (≥ 3 segments)

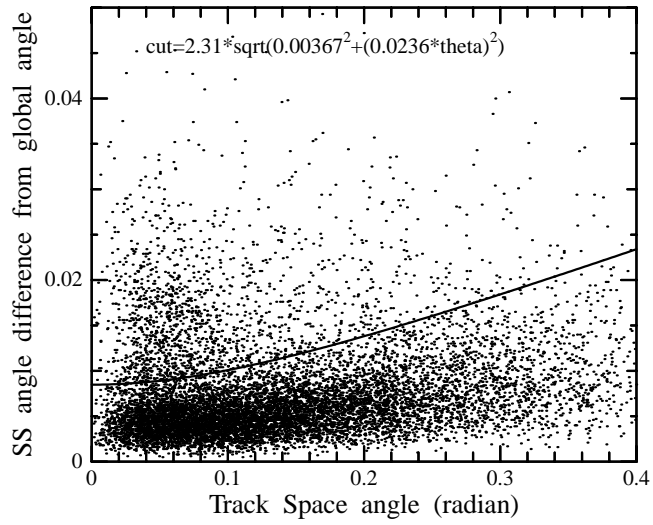
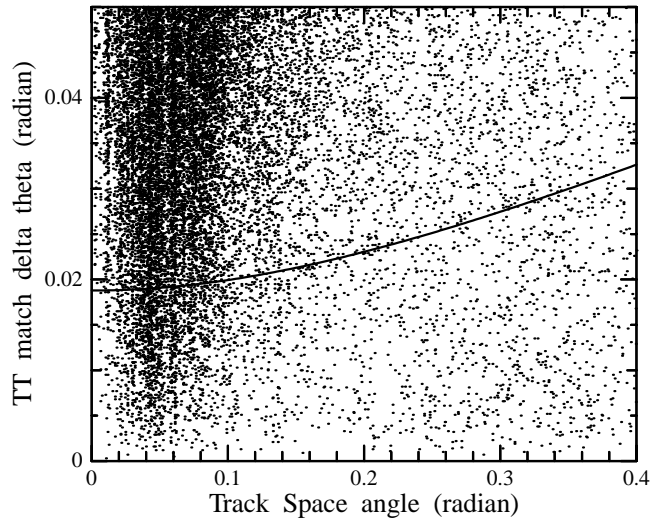


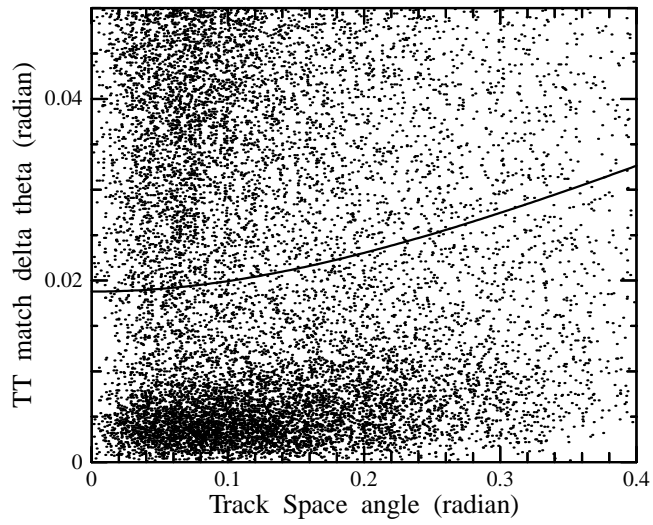
Figure 5.5: Global angle difference of 2-segment (Top) and 3-segment (Bottom) tracks

Angle difference with TT (\equiv 2 segments)



$$\text{cut}=3.44*\text{sqrt}(0.00546^2+(0.0194*\text{theta})^2)$$

Angle difference with TT



$$\text{cut}=3.44*\text{sqrt}(0.00546^2+(0.0194*\text{theta})^2)$$

Figure 5.6: TT angle difference of 2-segment (Top) and 3-segment (Bottom) tracks

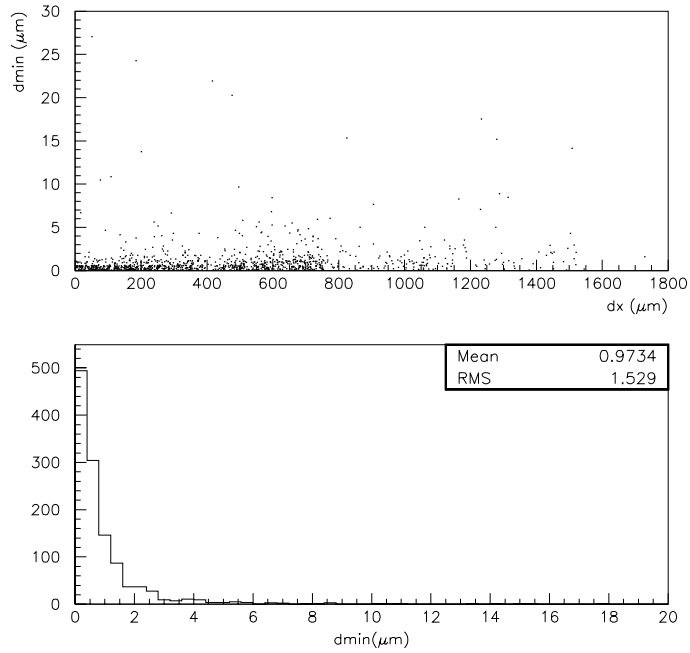


Figure 5.7: Top: minimum distance between muon track and other tracks versus vertex depth, bottom: minimum distance between muon track and other tracks.

- Muon and at least one TT-matched track must be reconstructed. (TT-matching allowance is 30 mrad). TT- matched track must be 3 plate connected.
- $\chi^2 < 1.5$ cut is applied in order to suppress fake connections.
- Distance between muon and TT-matched track must be larger than $\sigma_\theta dx$ where $\sigma_\theta = 0.0194\theta$ and dx is vertex depth.

If the event satisfies these conditions, it is sent to manual check.

5.3 Manual Check and Results

The last step in finding charm candidates is manual check of selected events. In the manual check, we first check the predicted plate.

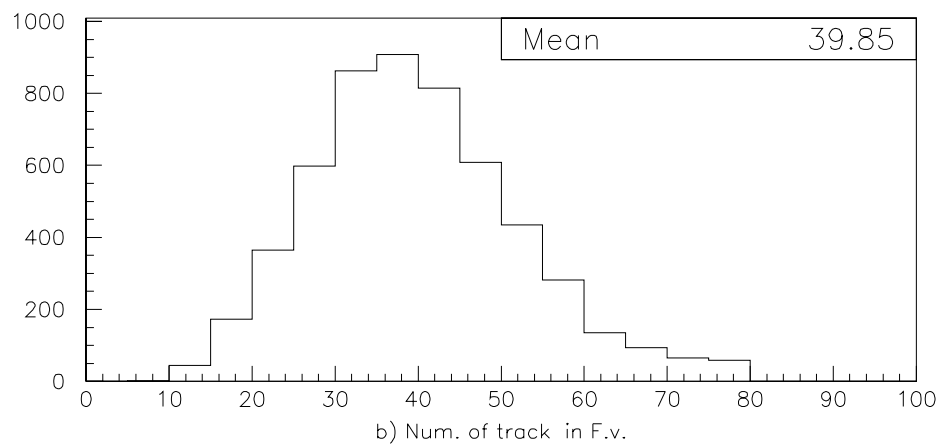
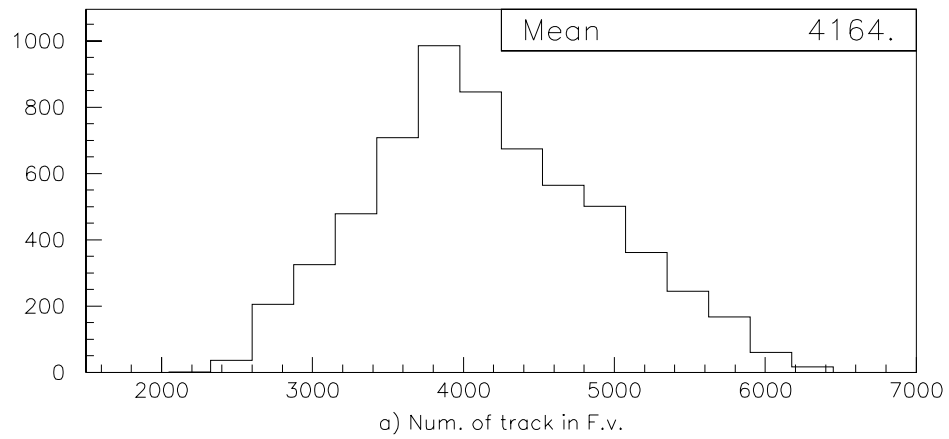


Figure 5.8: a) Number of tracks after first level alignment and tracking. b) Number of tracks which stop in fiducial volume (at least 2-segment connected) after low-momentum rejection.

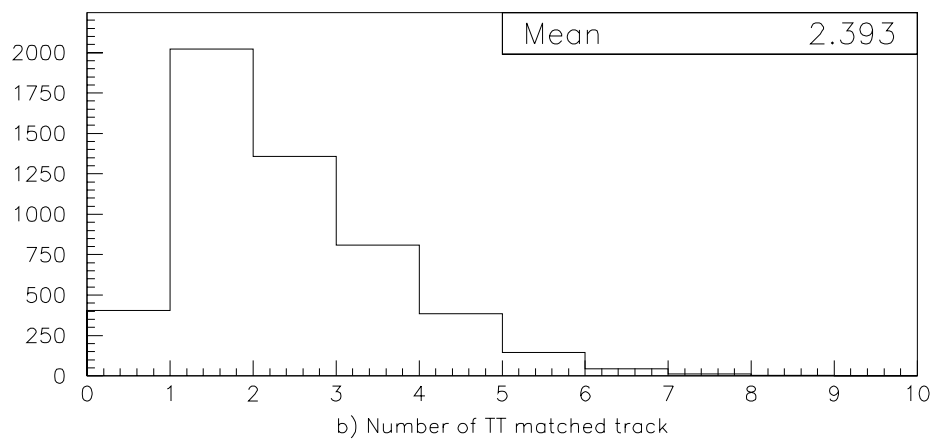
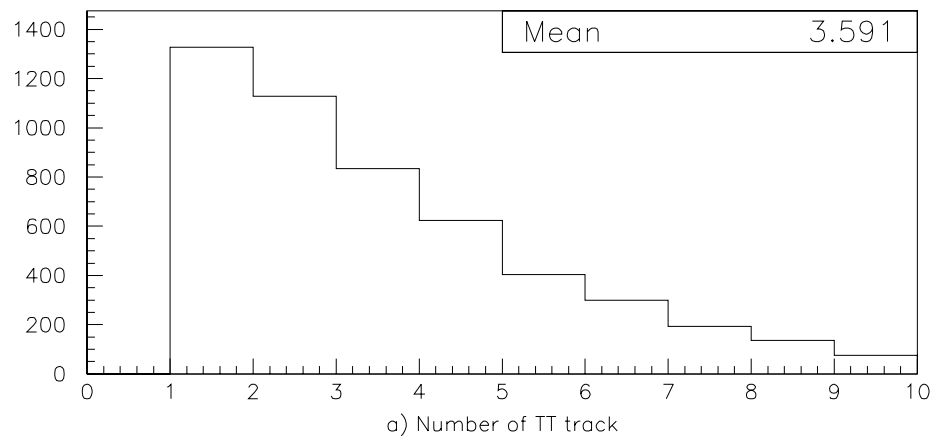


Figure 5.9: a) Number of TT track. b) Number of tracks that stops in fiducial volume and reconstructed at TT and pass the global angle cut

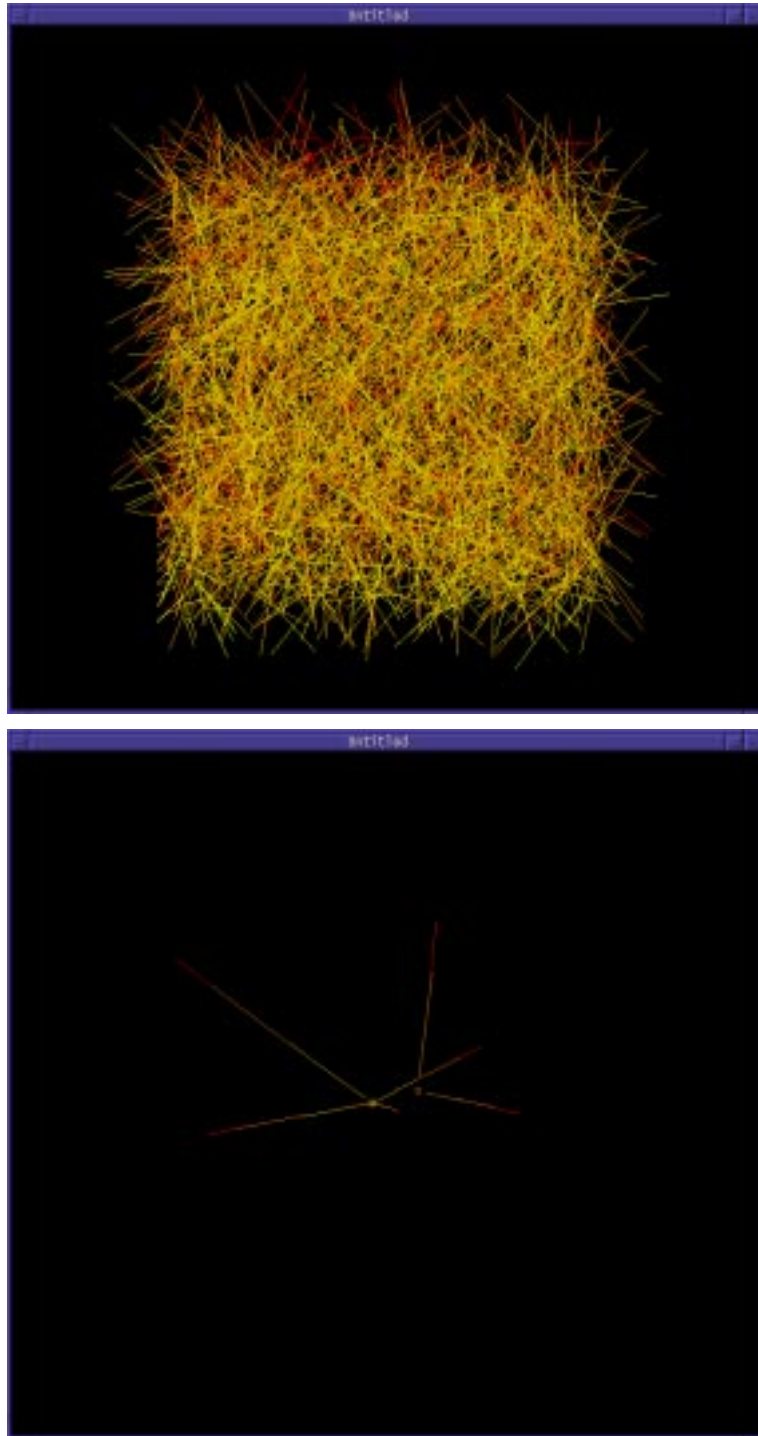


Figure 5.10: Top: All tracks in fiducial volume, bottom: after rejecting passing through and low momentum particles we get "Vee" event

Table 5.2: Data set 96

	11b	11t	12b	12t	15b	15t	16b	16t	Total
# of ν CC	641	845	699	964	764	508	841	878	6140
# of sel. ev. (A)	43	59	63	76	40	21	53	55	410
# of sel. ev. (B)	26	43	33	48	46	18	42	50	306
# of charm cand.	11	17	12	16	16	8	18	25	123

If the track (tracks) are passing through we follow it (them) until primary vertex. If it goes to a primary vertex, we measure track slopes and impact parameter for the possibility of short flight lengths or small angle kinks. If it is passing through the primary vertex plate we do not follow.

A vertex found in the emulsion is tagged as a decay vertex, if it is downstream of the primary vertex, there is no blob and number of decay daughters are consistent with charge conservation. A found kink event is tagged as a charm candidate if there is no trace of recoil or Auger electron at decay point and parent track goes to a primary vertex. Analysis is based on 8 half modules, shown in Figure (5.11) from 1996 and 1997 runs. From 12544 Net-Scan reconstructed neutrino charge current interactions 1058 and 730 events are selected by selection A and B respectively. 273 events are common in both selection samples. Therefore in total 1515 events were checked by eye and 269 decay topologies were observed. Table (5.4) shows the breakdown of decay topologies.

Table 5.3: Data set 97

	81b	81t	82b	82t	85b	85t	86b	Total
# of ν CC	798	994	793	999	903	646	1271	6404
# of sel. ev. (A)	65	114	106	106	85	54	118	648
# of sel. ev. (B)	50	57	55	65	60	40	97	424
# of charm cand.	13	16	20	29	20	12	36	146

Table 5.4: Found charm candidates

Topology	96 data	97 data	Total
	11t,11b,12t,12b	81t,81b,82t,82b	
	15t,15b,16t,16b	85t,85b,86t	
Kink	23	40	63
Trident	32	28	60
5-prong	3	1	4
Vee	52	59	111
4Vee	13	18	31
Total	123	146	269

5.4 Final Sample

We have found 142 D^0 decay candidates among 12544 Net-Scan reconstructed neutrino interactions. In order to suppress fake connections which produce fake vertices we require that the daughter and muon tracks are at least three segments connected. This results in loss of 15 D^0 events:

- in 12 events charm daughter is 2-segment connected,
- in 3 events primary muon is 2-segment connected.

Furthermore, 3 events were lost due to kinematical cuts applied for event location: 2 events due to momentum cut, ($0 < P_\mu < 30 \text{ GeV}$) and one event due to angle cut, ($\theta_\mu < 400 \text{ mrad}$). 2 D^0 candidates were not found in the Data Base because of some technical problem. Finally, we apply $E_{cal} > 4 \text{ GeV}$ cut in order

Table 5.5: D^0 sample used in analysis.

Topology	96 data	97 data	Total
Vee	41	52	93
4Vee	13	16	29

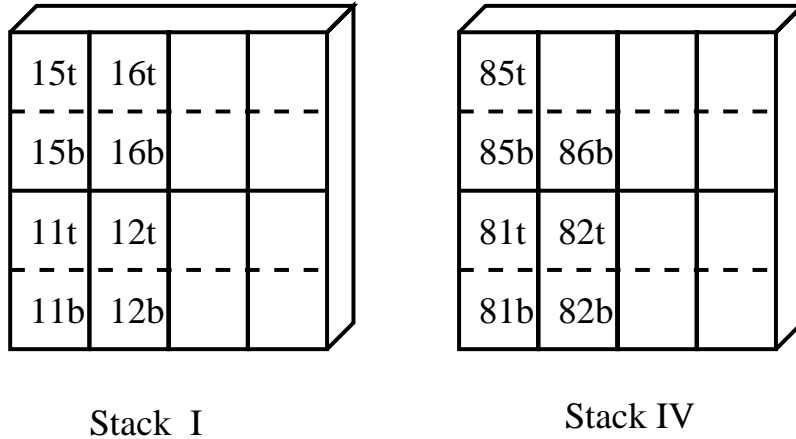


Figure 5.11: The scanned modules for D^0 production rate measurement.

to make DATA/MC ratio flat. By this cut, we do not lose any charm candidates but reconstructed neutrino interaction is reduced to 8028.

Our final sample consists of 122 D^0 decay candidates which includes 93 "Vee" and 29 "4Vee" decay topologies, found in 8028 located ν_μ CC interactions in emulsion. Breakdown of the sample is shown in Table (5.5). In order to estimate what fraction of charmed particles are found, a Monte Carlo (MC) simulation is performed. In the following section main steps of MC simulation will be given.

5.5 MC Simulation

MC simulation with the complete set-up and event reconstruction has been performed in order to estimate efficiencies and numbers of background events.

5.5.1 The MC Sample

As a MC sample, 127K CC (D.I.S.) ν_μ and interaction 3200 CC (Q.E.) ν_μ interaction which were processed with EFICASS 1.10/22 and CHORAL 2.13/22 are mixed according to

$$\frac{\sigma(Q.E.)}{\sigma(D.I.S.)} = 8.5\% \quad (5.1)$$

The number of charmed particles in the MC sample is shown in Table (5.6).

Table 5.6: MC charm sample

	$\mathbf{D^0}$	$\mathbf{D^+}$	$\mathbf{D_s^+}$	$\mathbf{\Lambda_c^+}$
Number	6128	2155	790	739

5.5.2 Net Scanning Efficiency Estimation

The correction factor for ν_μ interactions is obtained from MC simulation using the number of charm events over the number of found charms. Net Scanning

Table 5.7: Applied cuts

	Kink	Trident	Vee	4vee	5-pr
MC sample	1525	1938	4850	1025	135
In emulsion(A)	827	1061	2643	596	86
Located (B)	411	520	1415	285	41
Net Scanning accept.(C)	248	394	1226	258	33
Selection + manual check(D)	144	314	959	229	28
η_{net} (%)	35.0 ± 2.4	60.3 ± 2.1	67.8 ± 1.2	80.3 ± 2.4	68.3 ± 7.2

efficiency is characterized by the following cuts:

- A: Vertex is reconstructed in emulsion, in $142 \times 142 \text{ cm}^2$
- B: Event is located: a negative muon from primary vertex is reconstructed by target tracker, the applied cut is

$$\Delta\theta_{TT} < 3.44\sqrt{(0.00546)^2 + (0.0194\theta)^2}.$$

The muon momentum must be within interval $0 < P_\mu < 30 \text{ GeV}$, and its angle less then 0.4 rad. Primary vertex must the lie in between plates 3-36. Finally a cut on the total energy deposited in the calorimeter is applied: $E_{cal} > 4 \text{ GeV}$.

- C: Net Scanning acceptance: secondary vertex must lie in 2-36 plates and inside the Net Scanning fiducial volume, 14.22 mm^3 centered about primary vertex position. At least one of the decay daughter angle must be in the interval $-0.4 < \theta_{y,z} < 0.4$ rad.
- D: Event must be selected: At least one of decay daughters which is connected in least three plates is reconstructed by the target tracker. The cut on

$$\Delta\theta_{TT} < 3.44\sqrt{(0.00546)^2 + (0.0194\theta)^2},$$

is applied. Impact parameter between the primary vertex and the daughter track is calculated and following cuts are applied depending on the selection type:

$$IP > \sqrt{3^2 + (2\sigma_\theta dx)^2}$$

for selection A and $IP > \sigma_\theta dx$, $3 < IP < 100 \mu\text{m}$ for selection B where dx is vertex depth and

$$\sigma_\theta = \sqrt{(0.00305)^2 + (0.0194\theta)^2}.$$

If the event passes one of IP cuts, it is kept for manual check. To kill e-pairs, kink angle cut is applied: $\Delta\theta_k > 10\text{mrad}$.

- In manual check, a decay is not found if it is very short. From the manual scanning experience, we require that the flight length is longer then $20 \mu\text{m}$ For kink topologies, a kink is not seen if it is very small; we applied a daughter angle dependent cut on kink angle: $\theta_k > 0.1 \times \theta_{SB}$.

Table (5.7) shows Net Scanning efficiency for each topology. For "Vee" and "4Vee" topologies Net Scanning efficiency is estimated to be 68.7 % and 80.3 % respectively.

5.6 Background Estimation

Possible background sources for D^0 decays are mainly, e-pairs and decays of strange particles. In principle both backgrounds can be eliminated. An e-pair can be tagged as D^0 decay if the opening angle is large. In that case, momentum of electrons are very soft, as shown in Figure (5.13). Therefore at least one of them is scattered in few plates. We can eliminate this background by following down the decay daughter which does not match with TT. On the other hand, decays of strange particles are mainly 2-body: K_s^0 decays into $\pi^-\pi^+$ (68.61%) and $\pi^0\pi^0$ (31.39%) and Λ decays into $p\pi^-$ (63.9%) and $n\pi^0$ (31.39%). However, for D^0 decays, two body branching ratio is only $\text{Br}(D^0 \rightarrow K^-\pi^+) = 3.85\%$. Therefore, by doing co-planarity (as shown in Figure (5.12)) analysis we can eliminate background due to K_s^0 and Λ decays.

5.6.1 Electron-pair Check

All "Vee" topologies were studied carefully. In the selection it is required that at least one of the decay daughters is reconstructed at the target tracker. The other partner is checked whether "Vee" topology is D^0 decay or e-pair with big opening angle. From 116 "Vee" topologies, it is found that 13 are dimuon events and 103 are 1μ events. In 59 events of the 1μ sample, both decay daughters are reconstructed by the target tracker and in 44 events, only one daughter is reconstructed by the target tracker. For this sample, first Net Scan data is checked, to see whether the other partner is reconstructed or not. It was seen that in 24 events decay partner is reconstructed by Net Scan data (at least 3-plate connected track). In 18 events, decay partner angle is greater than 0.4 rad. For these, it was checked whether there exist hits in the target tracker corresponding to a track angle or not. We have seen for 17 events there are hits in target tracker. For one case, there were no hits, therefore this event was subtracted from the sample. 8 events which were not reconstructed in target tracker or Net Scan, were followed down and out of these 4 events were tagged as e-pairs (partner was scattered in

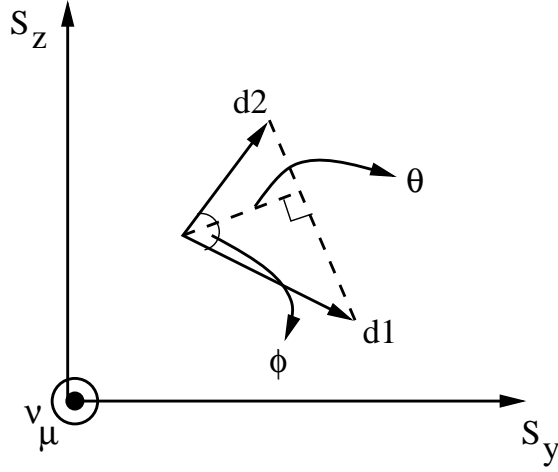


Figure 5.12: Co-planality ckeck.

emulsion). For the other 4 events the partner track was a "straight track", no scattering was seen; therefore these were kept in the sample. After subtracting those 5 "Vee" topologies incompatible with D^0 's as explained above, "Vee" sample was reduced to 111.

5.6.2 Background Due to K_s^0 and Λ Decay

Number of background events due to decays of K_s^0 and Λ are estimated using MC simulation. Since strange particles have long life times, mean flight length is 33.6 cm as shown in Figure 5.14; only K_s^0 and Λ whose momenta are low, decay in the emulsion. On the other hand, when we require Net Scanning and selection conditions, very few of them are retained. I have used about 127K reconstructed ν_μ CC MC events. Decays of K_s^0 and Λ can be background to D^0 decay if the event is located in the emulsion and passed the selection criteria and found in manual check. Expected number of background events can be written as

$$N_{bg}^{K_s^0} = \frac{\sigma(\nu_\mu N \rightarrow K_s^0 \mu^- X)}{\sigma(\nu_\mu N \rightarrow \mu^- X)} \times Br(K_s^0 \rightarrow \pi^- \pi^+) \times \eta_{net} \times \eta_{TT} \times N_{loc}^{CC}$$

$$N_{bg}^{\Lambda} = \frac{\sigma(\nu_\mu N \rightarrow \Lambda \mu^- X)}{\sigma(\nu_\mu N \rightarrow \mu^- X)} \times Br(\Lambda \rightarrow p \pi^-) \times \eta_{net} \times \eta_{TT} \times N_{loc}^{CC}$$

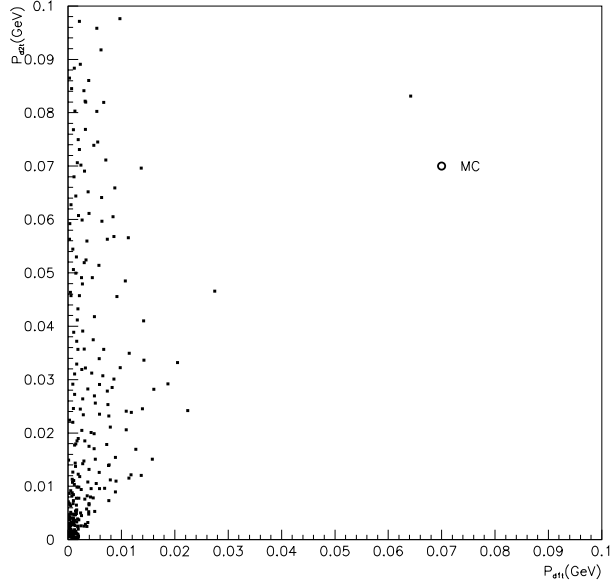


Figure 5.13: Scatter plot of e-pair transverse momenta from MC.

From the MC simulation, number of background events are estimated as

$$N_{bg} = \frac{1.48 \times 10^{-4}}{N_{CC}^{loc}} \quad (5.2)$$

The corresponding number of estimated background events due to K^0 and Λ decay in the present sample as 1.2.

For the "Vee" sample co-planarity check has been done as shown in Figure (5.15). It was seen that 4 events show two body decay topology. This is consistent with predicted number: 4.8 (1.2 (from K^0 and Λ decay)+3.6(from $D^0 \rightarrow K^- \pi^+$)).

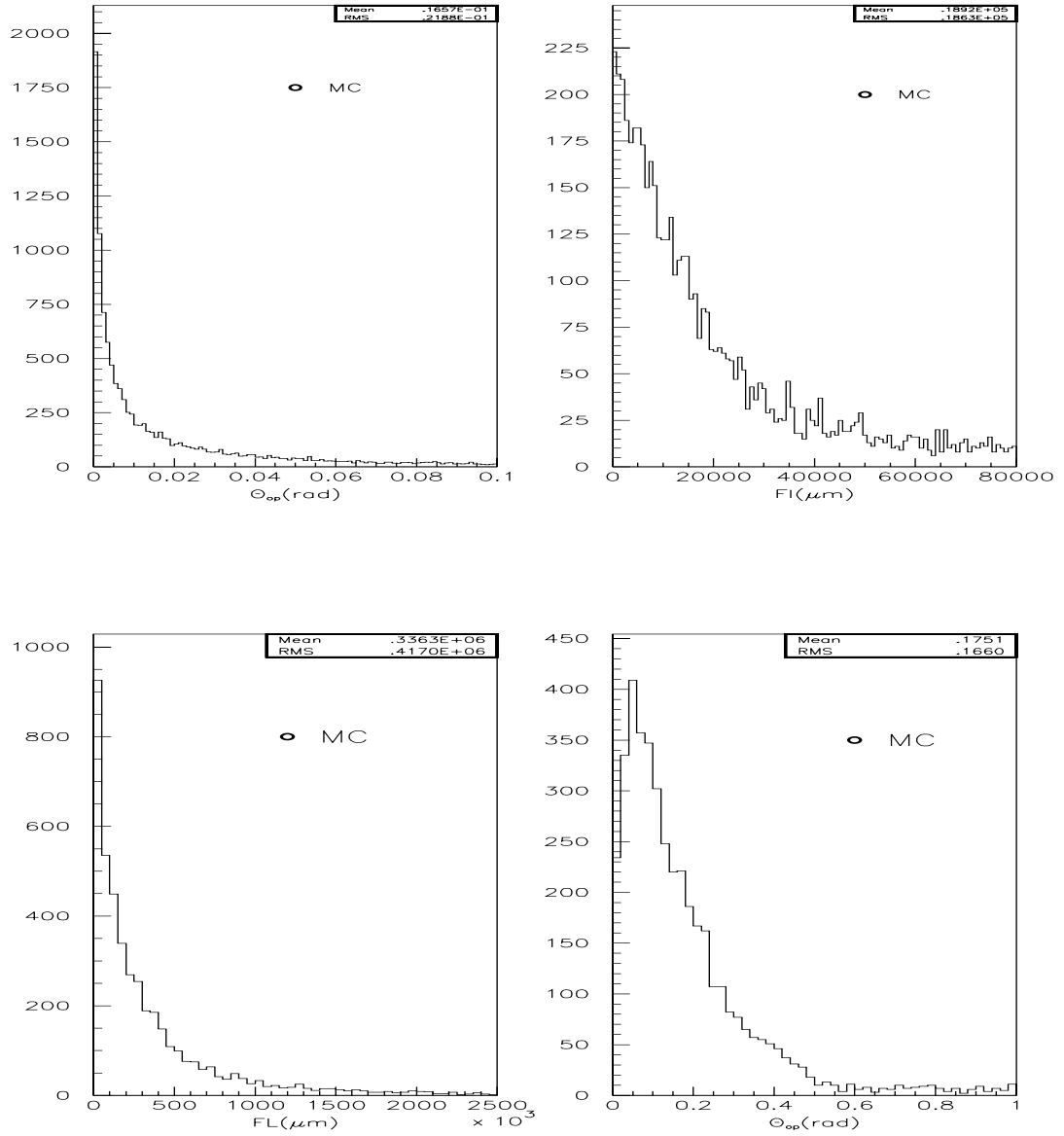


Figure 5.14: Top: e-pair conversion length and opening angle distribution from MC, bottom: K^0 flight length and opening angle distribution from MC.

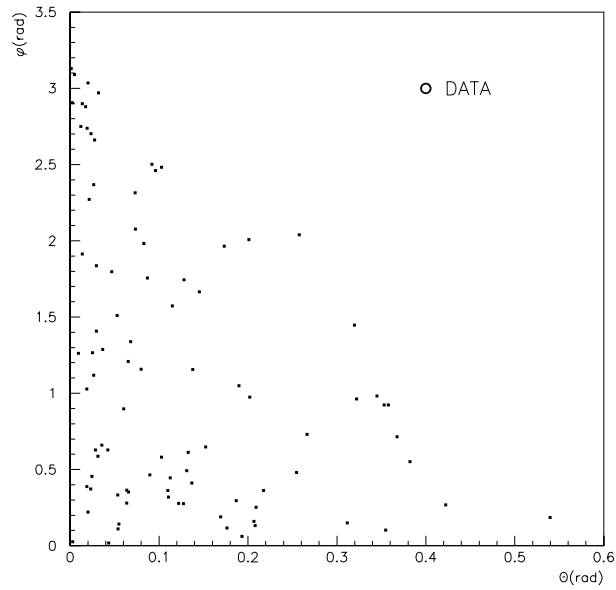
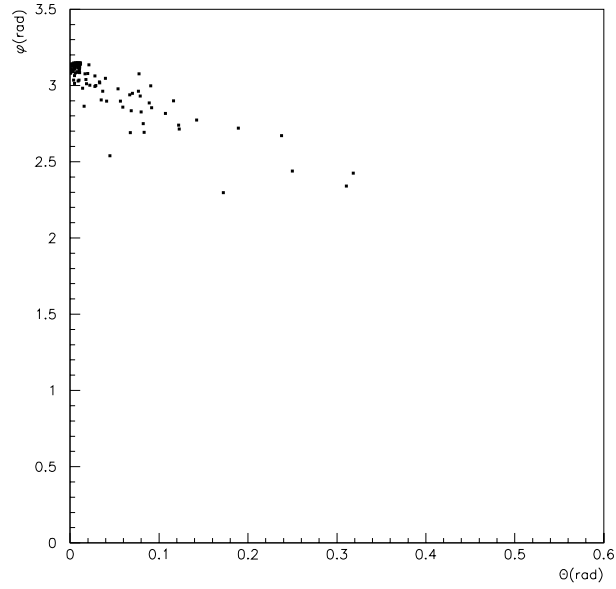


Figure 5.15: Top: ϕ angle vs. dip angle (explained in text) for K^0 from MC simulation, bottom: same distribution for D^0 candidates.

5.7 Systematic Errors

Systematic errors on production rates are due to the reliability of MC and overall TS pulse height cuts (applied while online data taking and in reconstruction programs of Net Scanning). Systematic errors estimated due to MC reliability are obtained from the discrepancy between data and MC simulation result. RMS of discrepancy in DATA/MC ratio is estimated as 7% from plot shown in Figure (5.17).

Systematic uncertainty due to TS pulse height cut was estimated as 5 % [60]. To be conservative, we assume 7 % systematic error due to overall Net Scanning. Therefore total systematic uncertainty on production rate is about 10 %.

5.8 D^0 Production Rates

Once an event is selected and found in emulsion, it is possible to study its production rate. Interaction kinematics are determined using the parameters: i) E_{vis} , total visible energy, calculated by summing up total energy deposited in the calorimeter, energy deposited in the target tracker and the spectrometer muon momentum, ii) x , the fraction of nucleon momentum carried by struck quark and calculated from $x = \frac{Q^2}{2mE_{had}}$ iii) y , fraction of energy carried by the hadronic system and obtained from $y = \frac{E_{had}}{E_{vis}}$, iv) Q^2 , square of four-momentum transfer and calculated from $Q^2 = 4E_{vis}P_{\mu}\sin^2\frac{\theta}{2}$. Data and MC predictions are shown in Figures (5.25) and (5.26).

After estimating correction factors, one can obtain D^0 production rates in terms of variables E_{vis} , Q^2 , x and y . The raw data is corrected using correction factors (shown in Figure (5.18)) obtained from MC simulation. The correction factors and corrected production rates with respect to parameters: E_{vis} , x , y , Q^2 are shown in Figures (5.19), (5.22), (5.23) and (5.24) respectively. The corrected cross section ratio is

$$\frac{\sigma(\nu_{\mu}N \rightarrow D^0\mu^{-}X)}{\sigma(\nu_{\mu}N \rightarrow \mu^{-}X)} = 1.998 \pm 0.223\% \quad (5.3)$$

The error includes both systematic and statistical uncertainties.

5.9 Dimuon Production Rate

We have found 31 dimuon charm events. As a sample we have used 15 $\mu^- \mu^+$ events (6 vee, 1 trident, 7 kink, 1 5-prong) which are characterized by following conditions:

- $\mu^- \mu^+$ event
- Both muons are reconstructed at muon spectrometer. This is required in order to eliminate π/K decays.
- Both muons are three plate connected. This is required to suppress fake connections.

16 events are excluded since in 5 events muon is two plate connected, in 4 events both muons are the same sign, $\mu^- \mu^-$ and in 7 events muon (daughter or primary) is not reconstructed at spectrometer. To determine the actual number of dimuon events corrections are made for Net Scanning efficiencies. These efficiencies are estimated from MC simulation and shown in Table (5.8). The corrected dimuon production rate is

$$\frac{\sigma(\nu_\mu N \rightarrow \mu^- c(c \rightarrow \mu^+ X)X)}{\sigma(\nu_\mu N \rightarrow \mu^- X)} = 0.6670 \pm 0.0898\% \quad (5.4)$$

The error includes both systematic and statistical uncertainties. The visible energy dependence of the dimuon charm production rate is shown in Figure (5.20).

5.10 Comparison with E531 Experiment

Charm production in neutrino interactions was measured by E531 experiment [54, 55, 56, 57] which was installed at Fermilab in order to study charmed particles

Table 5.8: Applied cuts for dimuon charm events.

	Kink	Trident	Vee	4vee
MC sample	2183	1429	3170	102
In emulsion	1205	757	1798	60
Located	406	205	611	17
Net Scanning accept.	245	144	509	15
Selection + manual check	212	127	463	15
$\eta_{net}\%$	52.2 ± 2.5	61.9 ± 4.3	75.8 ± 1.7	88.2 ± 7.8

properties. They found 121 charmed particles over 3855 located neutrino interactions. They have measured charmed particle production cross section in neutrino interaction as

$$\frac{\sigma(\nu_{\mu}N \rightarrow c\mu^{-}X)}{\sigma(\nu_{\mu}N \rightarrow \mu^{-}X)} = 4.9 \pm_{0.6}^{0.7} \% \quad (5.5)$$

and D^0 production cross section as

$$\frac{\sigma(\nu_{\mu}N \rightarrow D^0\mu^{-}X)}{\sigma(\nu_{\mu}N \rightarrow \mu^{-}X)} = 2.19 \pm_{0.35}^{0.39} \% \quad (5.6)$$

using the sample shown in Table (5.9). The energy dependence of D^0 production rate is shown in Figure (5.21). If we compare our result with E531 measurement [57] we see that, both measurements are consistent with each other but our measurement reflects the better precision.

Table 5.9: Found charmed particles in E531 experiment [57]

Charmed Particle	Number
D^0	57
D^+, D_s^+, λ_c^+	63

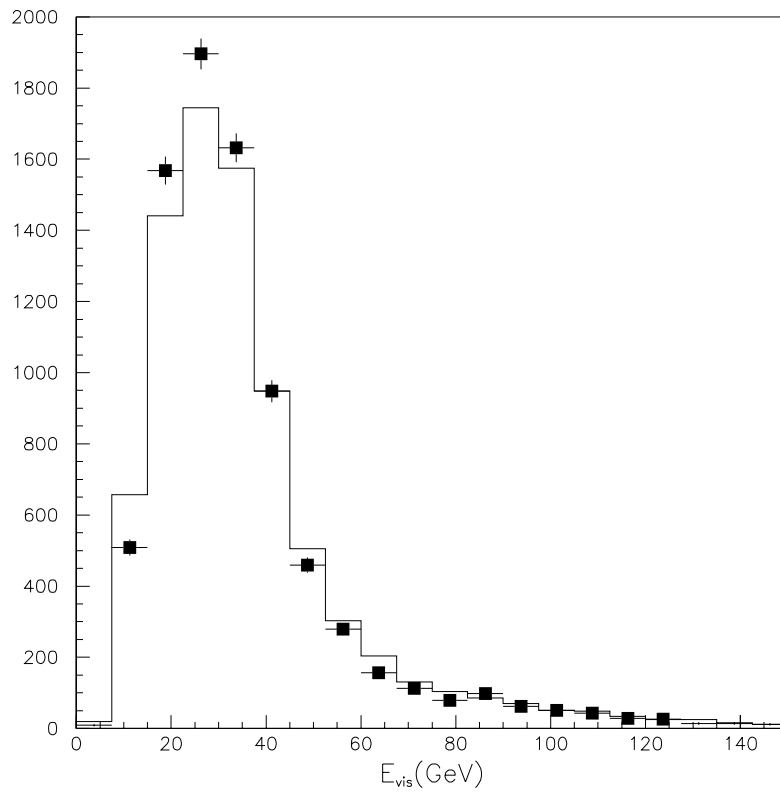


Figure 5.16: Comparison between distributions from data (point) and MC simulation (histogram) for located CC ν_μ events.

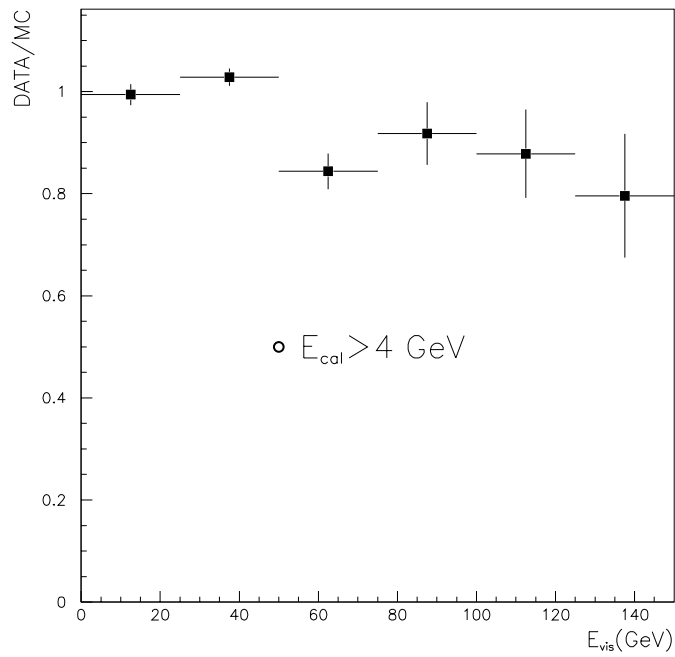
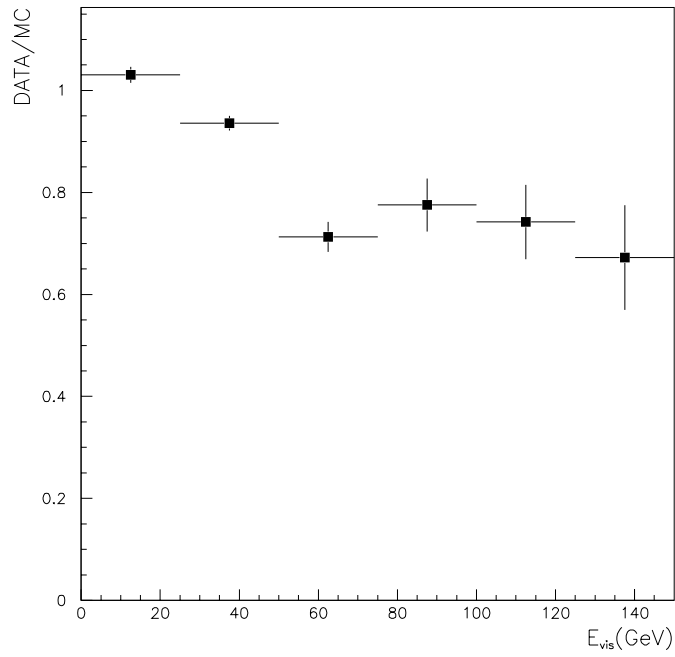


Figure 5.17: Top: DATA/MC ratio for located events without E_{cal} cut, bottom: with $E_{cal} > 4$ GeV cut

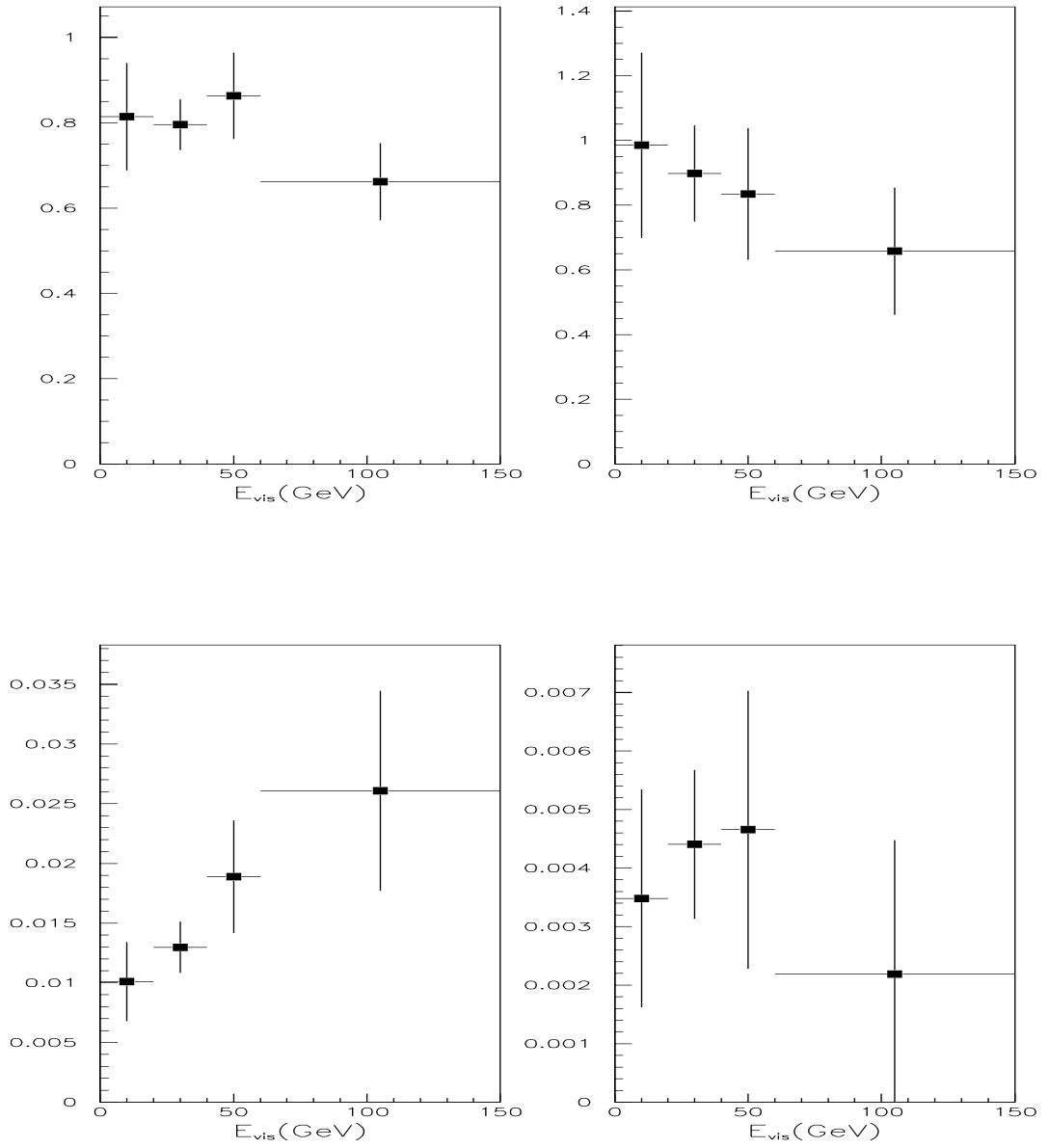


Figure 5.18: Top: $(\text{correction factor})^{-1}$ for "Vee" and "4Vee" bottom: production rate for Vee and 4Vee events.

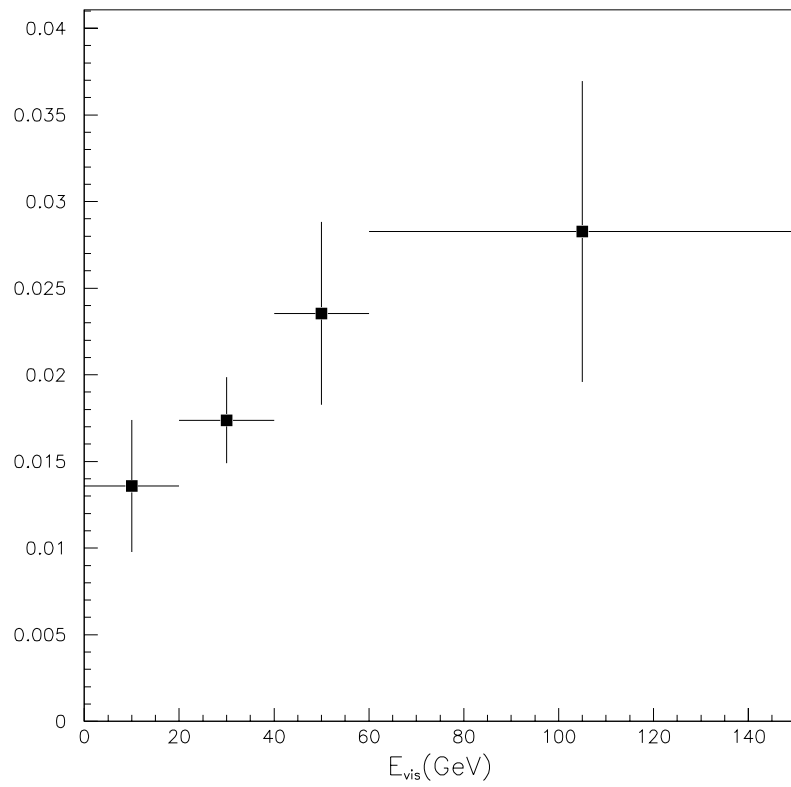


Figure 5.19: D^0 production rate in ν_μ CC interaction.

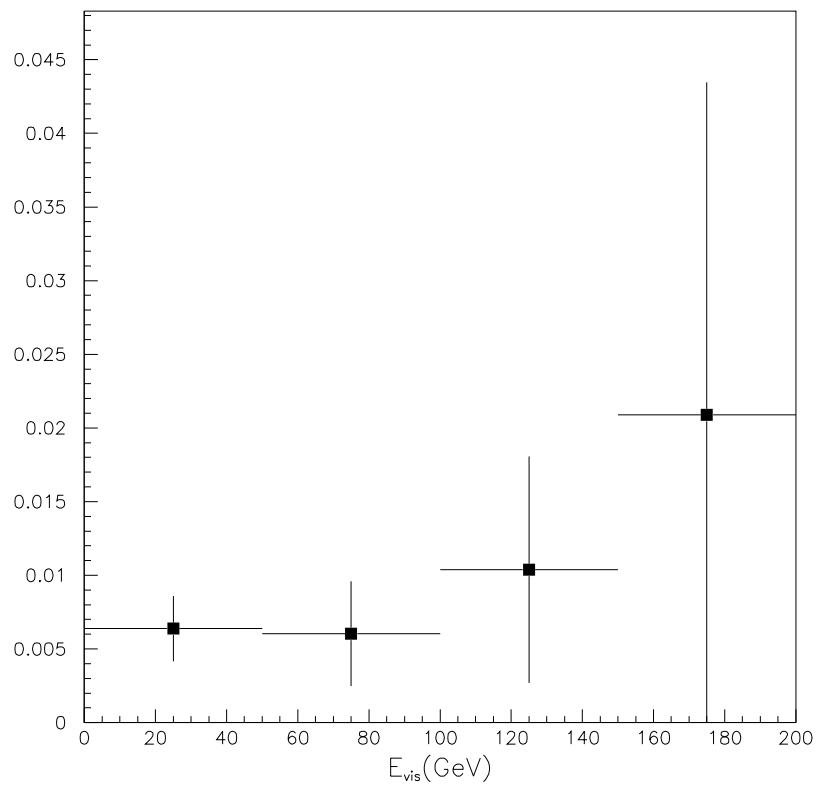


Figure 5.20: Dimuon production rate

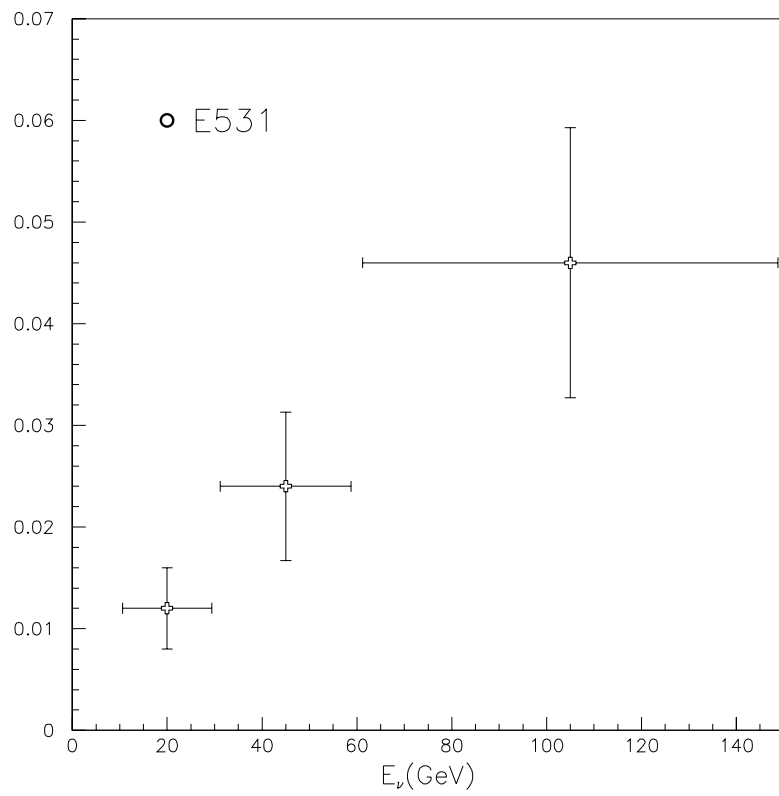


Figure 5.21: D^0 production rate in ν_μ CC interaction from E531 experiment.

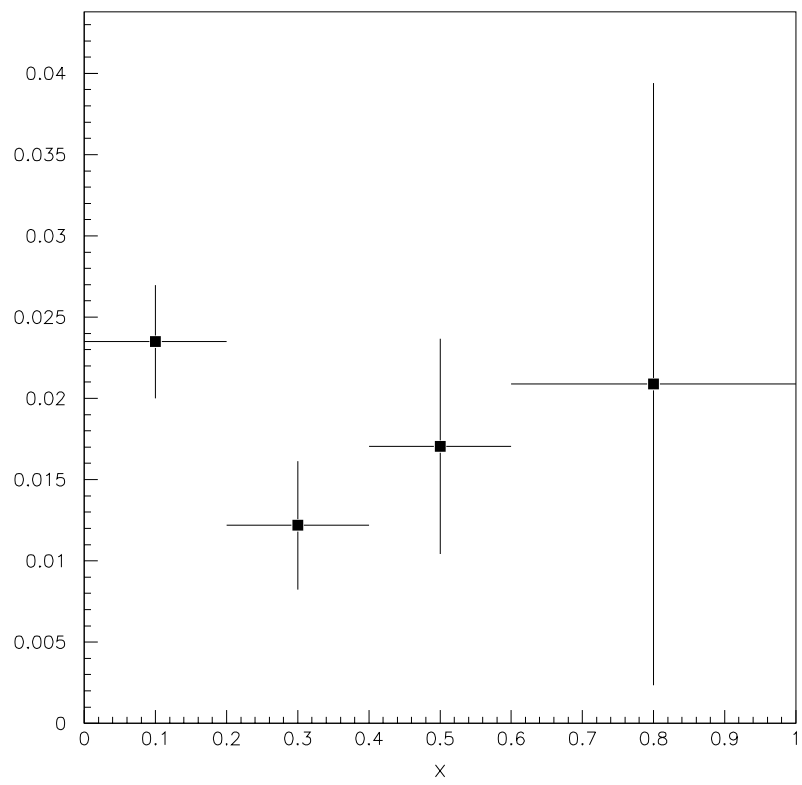


Figure 5.22: Bjorken x dependence of D^0 production rate.

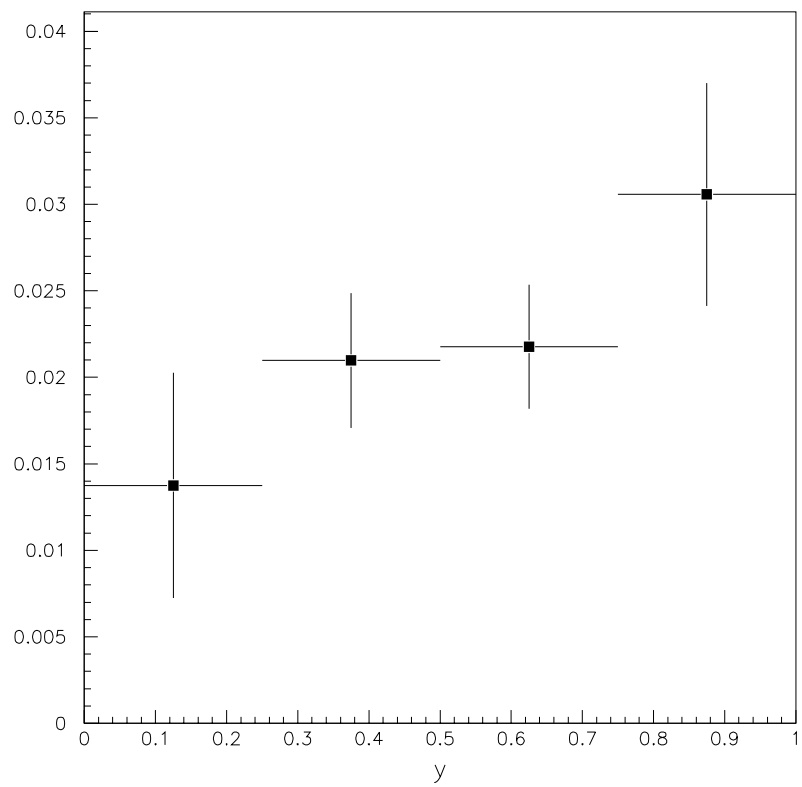


Figure 5.23: Bjorken y dependence of D^0 production rate.

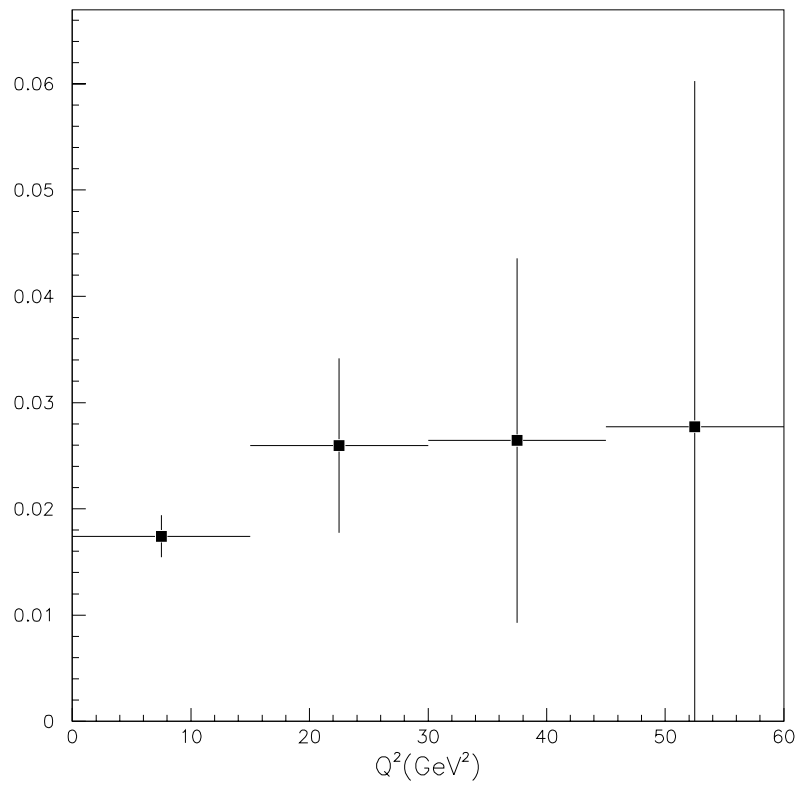


Figure 5.24: Q^2 dependence of D^0 production rate.

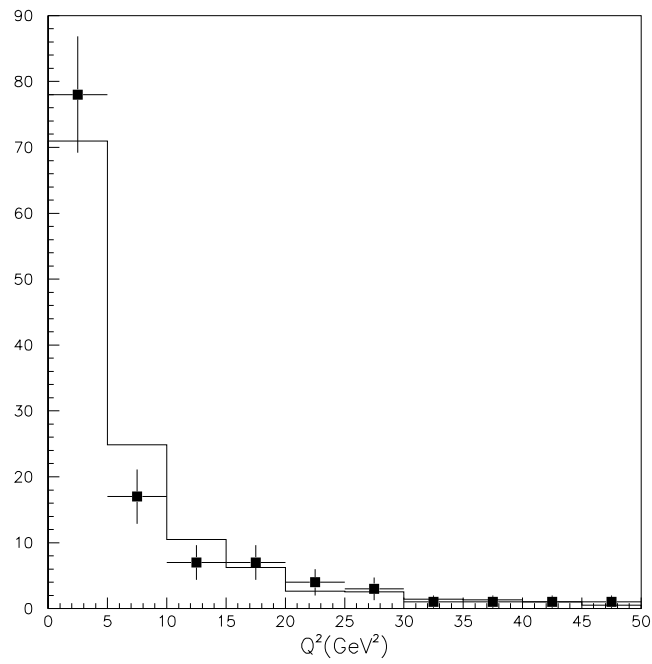
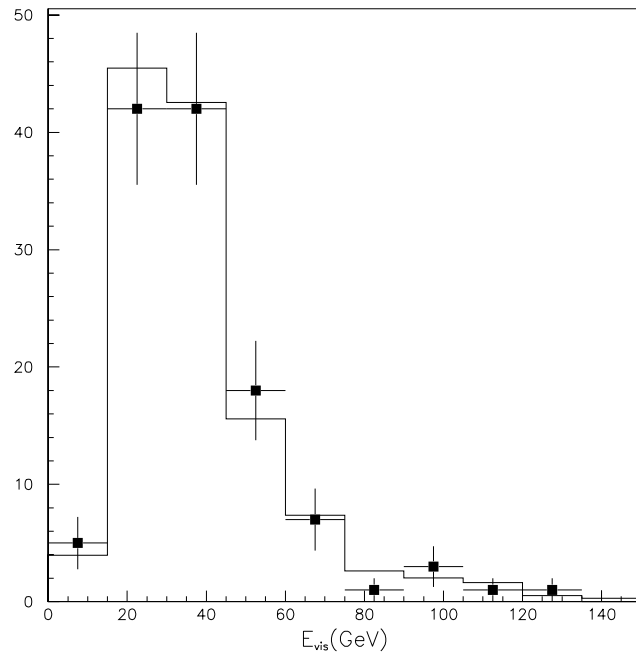


Figure 5.25: Comparison between distributions from the simulation (histograms) and the data (points) for D^0 events top: visible energy, bottom: momentum transfer.

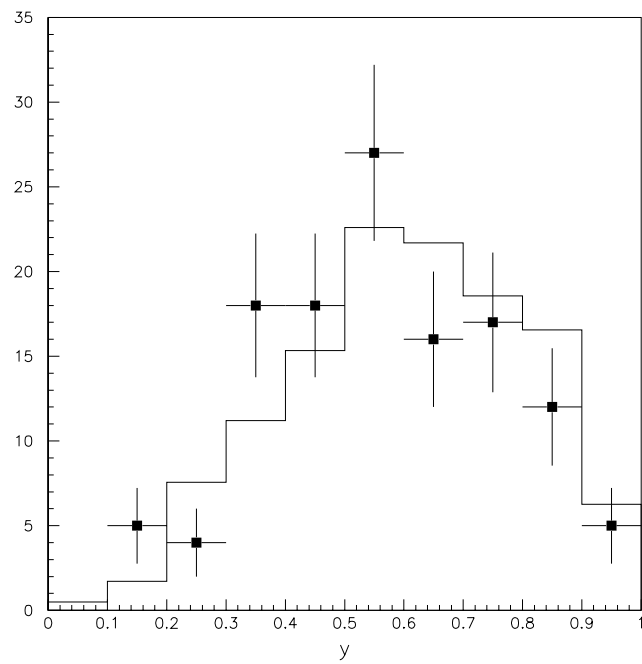
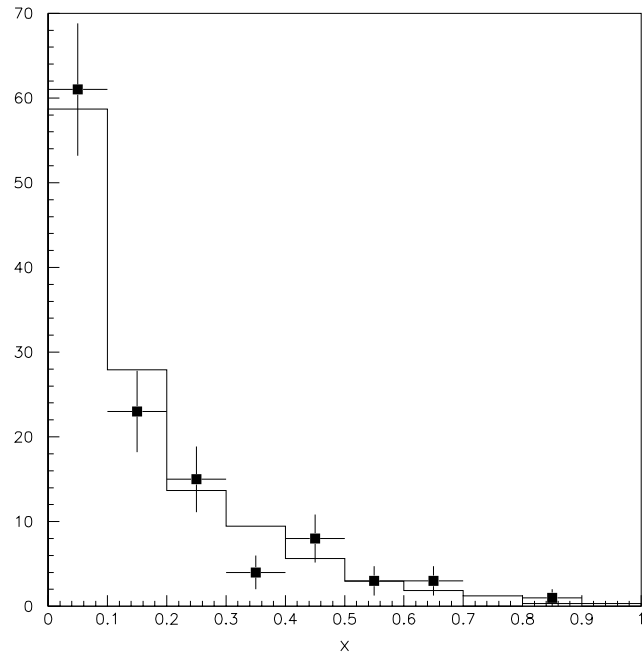


Figure 5.26: Comparison between distributions from the simulation (histograms) and the data (points) for D^0 events top: Bjorken x , bottom: Bjorken y .

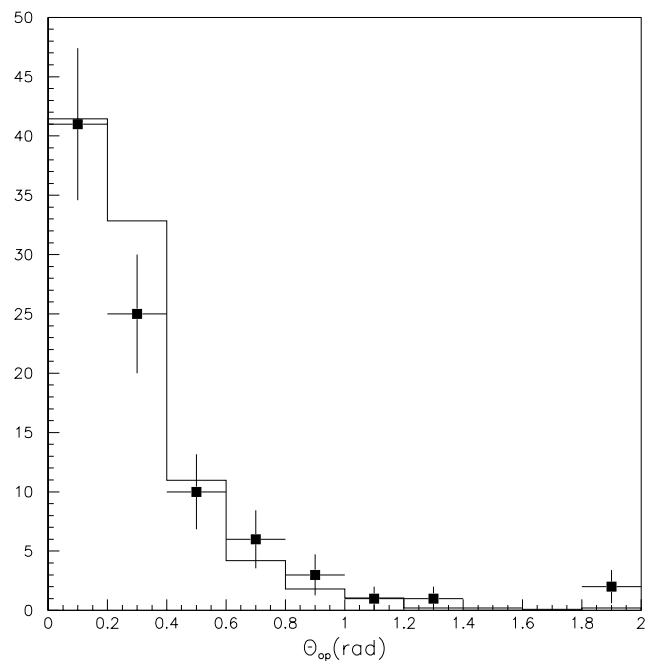
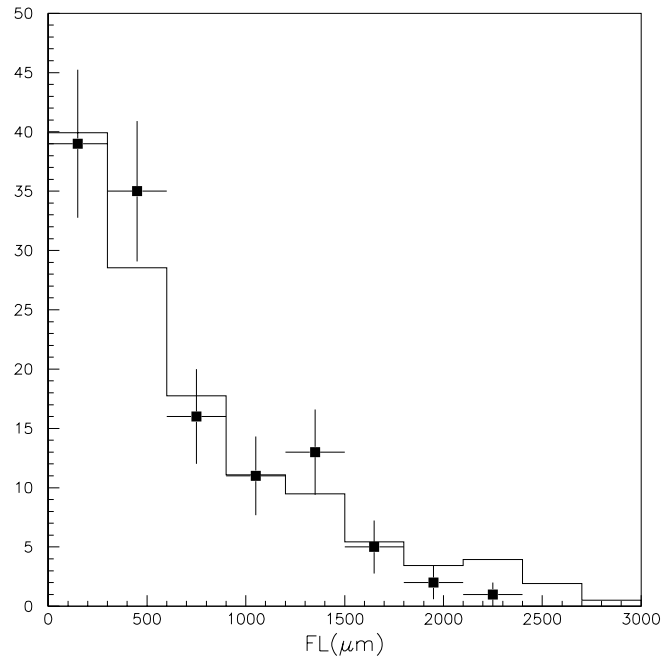


Figure 5.27: Comparison between distributions from the simulation (histograms) and the data (points) for D^0 events top: flight length , bottom: opening angle.

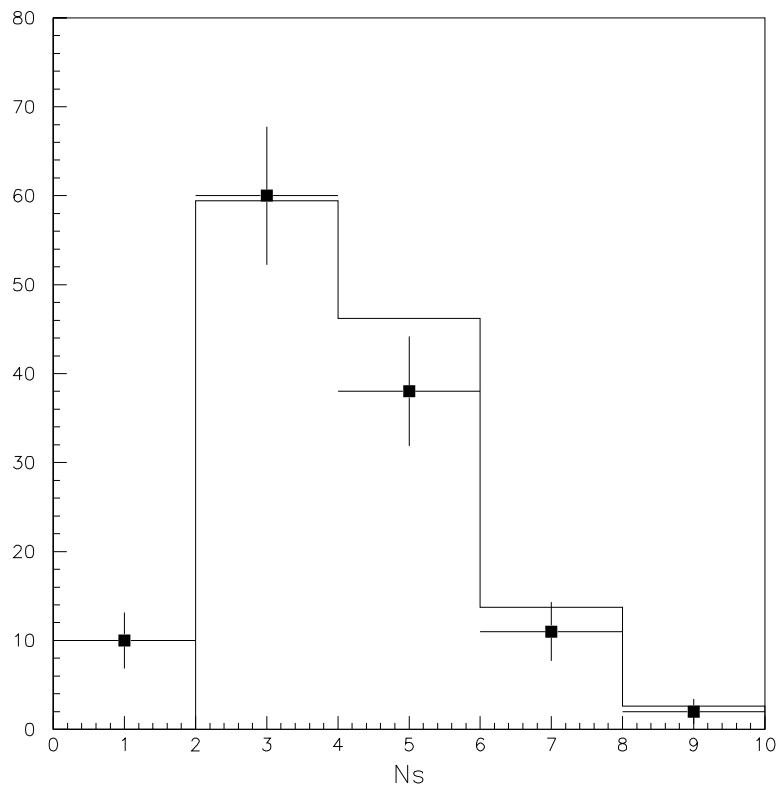


Figure 5.28: Comparison of the number of shower tracks at primary vertex, simulation (histograms) and the data (points) for D^0 events.

CHAPTER 6

CONCLUSION AND SUMMARY OF ANALYSIS

The CHORUS experiment which was designed to search for $\nu_\mu \rightarrow \nu_\tau$ oscillation, was run during years 1994-1997 and collected about 2.3 million triggers corresponding to 5.06×10^{19} protons on target. Of these 458,601 is 1μ and 116,049 is 0μ events. The first phase analysis in which about 143,742 1μ and 11,398 0μ events were located in emulsion, was completed recently. No τ^- candidate has been found and a limit on the probability of the oscillation has been set, $P_{\mu\tau} \leq 3.4 \times 10^{-4}$ at 90 % C.L.

In Ankara, we have performed emulsion scanning, mainly manual check and contributed to the Phase I analysis. The analysis of modules 28b, 28t, 68b, 68t from 1994 and 1995 data has been done. In these modules, 2043 1μ and 352 0μ events are located (location has been done in Nagoya university). These events have been checked by eye in Ankara and no τ^- decay candidate has been found so far. A Monte Carlo simulation has been performed in order to estimate the efficiency of our decay search method. After calculating efficiencies, a limit on $\nu_\mu \rightarrow \nu_\tau$ oscillation has been extracted as

$$P_{\mu\tau} \leq 1.14 \times 10^{-2} \quad (6.1)$$

at 90 % C.L.

The second phase analysis has been started with a new scanning and analysis method, "Net-Scanning", to reach the proposal sensitivity. This method allows the CHORUS to study also charm physics with a large statistics. The Net-Scanning is going on and will be finished in 2 years. The charm analysis presented in this thesis is based on 8 half modules in which 12544 ν_μ CC are reconstructed by Net-Scanning and 269 charmed particle decay candidates have been found. Using

122 D^0 decay candidates (found in 8028 ν_μ CC located interactions in emulsion after all cuts) which is more than two times the number in the E531 sample (57 D^0), D^0 production rate has been obtained

$$\frac{\sigma(\nu_\mu N \rightarrow D^0 \mu^- X)}{\sigma(\nu_\mu N \rightarrow \mu^- X)} = 1.998 \pm 0.223\% \quad (6.2)$$

The result is in agreement with E531 result with better precision.

Using 15 dimuon charm candidates, dimuon production rate is obtained as

$$\frac{\sigma(\nu_\mu N \rightarrow \mu^- c(c \rightarrow \mu^+ X)X)}{\sigma(\nu_\mu N \rightarrow \mu^- X)} = 0.6670 \pm 0.0898\% \quad (6.3)$$

E_{vis}, Q^2, x, y dependence of the D^0 cross section has been obtained.

REFERENCES

- [1] K. Winter, *Neutrino Physics*, Cambridge University Press, Cambridge, 1991.
- [2] C. W. Kim and A. Pevsner, *Neutrino in Physics and Astrophysics*, Harwood Academic Publishers, Pennsylvania, 1993.
- [3] B. Kayser, E. Gibrat-Debu and F. Perrier, *The Physics of Massive Neutrinos*, World Scientific Lecture Notes in Physics, Vol. 25, World Scientific, Singapore, 1989.
- [4] R. N. Mohapatra and P. B. Pal, *Massive Neutrinos in Physics and Astrophysics*, World Scientific Lecture Notes in Physics, Vol. 25, World Scientific, Singapore, 1991.
- [5] I. J. R. Aitchison and A. J. G. Hey, *Gauge Theories in Particle Physics*, USA, 1989.
- [6] B. M. Bilenky and S. G. Mikhov, *Introduction to Feynman Diagrams and Electroweak Interactions Physics*, Editions Frontieres, France, 1994.
- [7] S. M. Bilenky, C. Giunti and W. Grimus, *Progr. in Part and Nucl. Phys.* **43** 1. (1999)
- [8] F. Halzen and A. D. Martin *Quarks and Leptons* John Wiley and Sons (1984).
- [9] W. H. Barkas, *Nuclear Research Emulsion*, Academic Press London (1973).
- [10] E. S. Abers and B. W. Lee, *Phys. Rep.* **9**, 1 (1973).
- [11] S. M. Bilenky and S. Pontecorvo, *Phys. Rep.* **41**, 225 (1978).
- [12] S. M. Bilenky and S. T. Petcov, *Rev. of Mod. Phys.* **58**, 871 (1987).
- [13] S. M. Bilenky, B. Pontecorvo, *Phys. Lett.* **B 102**, 32 (1981).
- [14] E. Fermi *Z. Physik* 88-161 (1934).
- [15] G. Danby et. al., *Phys. Rev. Lett.* **9**, 6 (1962).
- [16] M. Perl et. al., *Phys. Rev. Lett.* **35**, 1489 (1975).
- [17] N. Ellis and M. Neubert, CERN Yellow Report (1995).
- [18] N. Ellis and J.M Russel, CERN Yellow Report (1999).

- [19] S. Glashow, Nucl. Phys. **22**, 579 (1961).
- [20] A. Salam, Phys. Lett. **13**, 168 (1964).
- [21] S. Weinberg, Phys. Rev. Lett. **19**, 1264 (1967).
- [22] P. W. Higgs, Phys. Lett. **12**, 132 (1964).
- [23] B. Kayser, Phys. Rev. **D 26**, 1662 (1982).
- [24] J. F. Nieves, Phys. Rev. **D 26**, 3152 (1982).
- [25] R. E. Shrock, Nucl. phys. **B 206**, 359 (1982).
- [26] R. Barbieri and R. N. Mohapatra, Phys. Lett. **B 218**, 350 (1989).
- [27] B. W. Lee and R. E. Shrock, Phys. Rev. **D 16**, 1444 (1977).
- [28] K. Fujikawa and R. E. Shrock, Phys. Lett. **D 45**, 963 (1980).
- [29] B. M. Pontecorvo, Soviet ZhEFT, **53**, 1717 (1967).
- [30] F. Reines and C. L. Cowan, Phys. Rev. **90**, 492 (1953).
- [31] B. Kayser, Phys. Rev. **D 30**, 1023 (1984).
- [32] B. Kayser, Comments Nucl. Part. Phys. **14**, 64 (1985).
- [33] P. I. KasteV, S. T. Petcov, Phys. Lett. **B 395**, 69 (1997).
- [34] B. Kayser, A. S. Goldhaber, Phys. Rev. **D 28**, 2341 (1983).
- [35] K. Winter, Phys. Lett. **B 346**, 190 (1995).
- [36] T. M. Gould, T.Z. Rothstein, Phys. Lett. **B 333**, 545 (1994).
- [37] B. Kayser, Phys. Rev. **D 24**, 110 (1981).
- [38] T. Nakano Ph.D. Thesis, Nagoya University (1997).
- [39] E. Eskut et. al., CHORUS collaboration submitted to Phys. Lett.
- [40] J. Bruner, CHORUS internal note (1997).
- [41] J. Visschers, CHORUS internal note (1997).
- [42] C. Weinheimer, CHORUS internal note (1997).
- [43] O. Sato, CHORUS internal note (1997).
- [44] M. Canu, CHORUS internal note (1997).

- [45] Y. Obayashi, CHORUS internal note (1997).
- [46] J. Bruner, CHORAL manual.
- [47] M. Komatsu, Nagoya University note (1999).
- [48] Stefania Riccardi, CHORUS internal note (1995).
- [49] M. Güler, M.Sc. Thesis, Middle East Technical University (1997).
- [50] S. Aoki et al., Nucl. Instr. and Meth. **A 447**, 361 (2000).
- [51] S. Aoki et al., Nucl. Instr. and Meth. **B 51**, 466 (1990).
- [52] A. O. Bazarko, CCFR collaboration hep-ex/9406007 (1994).
- [53] F. Dydak et. al., CDHS coll. Phys. Lett. **B, 134** 281 (1984).
- [54] N. Ushida et. al., E531 Collaboration, Phys. Lett. **B, 121** 287 (1983).
- [55] N. Ushida et. al., E531 Collaboration, Phys. Lett. **B, 121** 292 (1982).
- [56] N. Ushida et. al., E531 Collaboration, Phys. Lett. **B, 206** 380 (1988).
- [57] N. Ushida et. al., E531 Collaboration, Phys. Lett. **B,A 206** 375 (1988).
- [58] K. Niwa, Contrib, to the "Snowmass '94" Conference on Particle and Nuclear Astrophysics and Cosmology in the next Millennium, Snowmass, 1994.
- [59] M. V. Donckt Ph.D. Thesis, ULB (1999), Y. Obayashi Ph.D. Thesis Nagoya University (1999), R. G. C. Oldeman Ph.D. Thesis NIKHEF (2000), E. Pesen Ph.D. Thesis Middle East Technical University (1997).
- [60] G. Brooijmans Ph.D. Thesis, Universite catholique de Louvain (1998).
- [61] M. Güler et. al., Opera Proposal (2000).
- [62] A. Rubbia, Proceedings of the Third Workshop on Tau Lepton physics, Montreux, Switzerland 1994 Nucl. Phys. **B** (proc. Suppl.)
- [63] G. Rosa, Proceedings of the Third Workshop on Tau Lepton physics, Montreux, Switzerland 1994 Nucl. Phys. **B** (proc. Suppl.) **40**, 85 (1995).
- [64] CHORUS collab., The CHORUS Experiments to Search for $\nu_\mu \rightarrow \nu_\tau$ Oscillation, CERN-PPE/97-33.
- [65] Particle Data Group, R. Barnett et al., Phys. Rev. **D 50**, 1 (1996).
- [66] F. J. Hasert et al., Phys. Lett. **B 46**, 121 (1973).
- [67] P. B. Pal, Int. of Mod. Phys. **7**, 5387 (1992).

- [68] CHARM II Collab., L. Montanet, Phys. Lett. **B 345**, 115 (1995).
- [69] CHARM II Collab., K. Winter, Phys. Lett. **B 335**, 246 (1994).
- [70] G. Mills (LSND coll.), to appear on the Proc. of the XIX Int. Conf. on Neutrino Physics and Astrophysics, (2000).
- [71] B. Lundberg (DONUT coll.), to appear on the Proc. of the XIX Int. Conf. on Neutrino Physics and Astrophysics, (2000).
- [72] H. Sobel (Super Kamiokande coll.), to appear on the Proc. of the XIX Int. Conf. on Neutrino Physics and Astrophysics, (2000).
- [73] K. Nakamura (K2K coll.), to appear on the Proc. of the XIX Int. Conf. on Neutrino Physics and Astrophysics, (2000).
- [74] T. Man (SOUDAN2 coll.) to appear on the Proc. of the XIX Int. Conf. on Neutrino Physics and Astrophysics, (2000).
- [75] PDG, Eur. Phys. J. **C 3**, 1-794 (1998).

APPENDIX A

INTERESTING EVENTS FOUND IN ANKARA

As explained in chapter 4, 352 0μ , 2043 1μ and 65 2μ events are located in modules 28B, 28T, 68B, 68T. Eye-check of 0μ and 2μ samples are completed. We continue to scan 1μ sample. Until now checking of 1μ 's in the 68B are finished. From that scanned sample we have found 7 interesting decay topologies and 3 secondary interactions. The preliminary analysis of these events are done. In the following, we will discuss them.

A.1 Event 15764430

This event, found in module 28B, is a 2μ event. The event topology is shown in figure A.1. Two shower and one black tracks are emitted from primary vertex which is at the downstream of plate 11. One of the shower track is muon reconstructed at muon spectrometer with a momentum 10.8 GeV. The other shower track shows a kink decay topology at the base of plate 9. The kink daughter is a muon whose momentum is reconstructed in hadron spectrometer as 2.0 GeV. The kink angle and the flight length are measured as 176 mrad and 1314.2 μm . The transverse momentum is

$$P_T = 2.0 \times \sin\theta_k = 352 \text{ MeV}/c \quad (\text{A.1})$$

P_T is very useful parameter in order to identify the decay topology. Table A.7 shows a list of kink decay topologies and corresponding branching ratios and maximum P_T 's associated to decay daughter. Since measured P_T is 352 GeV/c we should give up K^+ and π^+ decays in which maximum P_T 's are 236 MeV/c and

30 MeV/c respectively. Therefore interpretation of this decay is

$$\begin{aligned}\nu_\mu N &\rightarrow \mu^- D^+ X \\ D^+ &\rightarrow \mu^+ \nu_\mu \bar{K}^0 \text{ or} \\ D^+ &\rightarrow \mu^+ \nu_\mu\end{aligned}$$

Assuming this topology we can roughly estimate life time of D^+ as

$$\begin{aligned}\gamma &\sim \frac{1}{\langle \theta \rangle} \sim 5.7 \\ L &= \beta \gamma c t \\ t &\sim 0.8 \times 10^{-12} s\end{aligned}$$

A.2 Event 16553623

This event topology is shown in figure A.2. It is found in module 28B and belong to 2μ sample. From the primary vertex, 4 shower and 11 black tracks are emitted. The primary vertex is at downstream of plate 32. The second vertex is in the same side of the plate 32. This is a short 4-prong decay whose flight length is $51.4\ \mu m$. Two of the primary vertex and three of decay daughter tracks are reconstructed by fiber tracker. Since there is no 4-prong decay of neutral strange particles, the clear interpretation of this event is the following

$$\begin{aligned}\nu_\mu N &\rightarrow D^0 \mu^- \nu_\mu X \\ D^0 &\rightarrow K^- \pi^+ \pi^+ \pi^-\end{aligned}$$

A.3 Event 20401968

The event showing Vee decay topology is shown on figure A.3. This event was found in module 28B, belongs to 2μ sample. Four shower and 5 black tracks come

out from the primary vertex which is at downstream of plate 31. The second vertex is found at the same side the plate 31. The flight length and opening angle are measured as $104 \mu m$ and 204 mrad respectively. Since the one of the decay daughter is muon with a momentum $2.2 \text{ GeV}/c$, the interpretation of this event is clear

$$\begin{aligned}\nu_\mu N &\rightarrow D^0 \mu^- X \\ D^0 &\rightarrow \mu^+ K^- \nu_\mu\end{aligned}$$

We can say this is a ν_μ CC production of D^0 and subsequent decay of D^0 to $\mu^+ K^- \nu_\mu$.

A.4 Event 27913325

This is 2μ event which was found in module 68B and shown in figure A.4. The primary vertex, located at upstream of plate 14, has 2 shower and 4 black tracks. One of shower track is muon with a momentum $-4.9 \text{ GeV}/c$ which is reconstructed at muon spectrometer. The other shower track shows kink topology at downstream of the same plate. Therefore it is a short kink. The kink angle and the flight length are measured as 55 mrad and $173 \mu m$. The transverse momentum, P_T is $121 \text{ MeV}/c$. That P_T allows also K^+ decay into π^+ . On the other hand the flight length is very short w.r.t. mean flight length of K^+ . Therefore the interpretation for this decay is

$$\begin{aligned}\nu_\mu N &\rightarrow \mu^- D^+ X \\ D^+ &\rightarrow \mu^+ \nu_\mu \bar{K}^0 \text{ or} \\ D^+ &\rightarrow \mu^+ \nu_\mu\end{aligned}$$

The approximate life time is $t \sim 3.17 \times 10^{-14} s$.

A.5 Event 33800256

One of the interesting events showing a trident decay topology which was found in the module 68T belongs to 0μ sample. The event decay topology is shown in figure A.5. Three tracks are come out from primary vertex point which is at downstream of the plate 7. The decay vertex is at downstream of plate 6. Two tracks from primary vertex and all the decay daughters are reconstructed by fiber tracker. The flight length is measured as $761 \mu m$. The electronic data information is checked and no muon is seen in the event. Therefore this event can be a candidate for τ^- decay.

$$\begin{aligned}\nu_\tau N &\rightarrow \tau^- X \\ \tau^- &\rightarrow \pi^- \pi^+ \pi^- \nu_\tau\end{aligned}$$

or this can be a NC charm production,

$$\begin{aligned}\nu_\mu N &\rightarrow D^+ \nu_\mu X \\ D^+ &\rightarrow K^+ \pi^- \pi^+ \quad or \\ D^+ &\rightarrow K^+ \pi^- \pi^+ \pi^0 \quad or \\ D^+ &\rightarrow K^+ \pi^- \pi^+ \bar{K}^0\end{aligned}$$

There exist one more possibility for this event: ν_e CC charm production

$$\begin{aligned}\nu_e N &\rightarrow D^+ e X \\ D^+ &\rightarrow K^+ \pi^- \pi^+ \quad or \\ D^+ &\rightarrow K^+ \pi^- \pi^+ \pi^0 \quad or \\ D^+ &\rightarrow K^+ \pi^- \pi^+ \bar{K}^0\end{aligned}$$

Since there are several possibilities for this event more study must be done in order to give clearer interpretation.

A.6 Event 34081069

One of the 1 μ events showing the decay topology is shown in figure A.6. There are 3 shower and 2 black tracks at primary vertex which is at downstream of the plate 27. One of the shower track from primary vertex shows a trident decay topology at same side of the plate 27. One of the decay daughter tracks and 2 of the primary tracks are reconstructed by fiber tracker. The flight length is measured as 108.0 μm . Since flight length is short w.r.t mean flight length of the strange particles, we can give the following interpretation for this event

$$\begin{aligned}\nu_\mu N &\rightarrow \mu^- D^+ X \\ D^+ &\rightarrow K^- \pi^+ \pi^+ \text{ or} \\ D^+ &\rightarrow K^- \pi^+ \pi^+ \pi^0 \text{ or} \\ D^+ &\rightarrow K^- \pi^+ \pi^+ \bar{K}^0\end{aligned}$$

A.7 Event 34361592

This is the first event showing decay topology observed in Ankara. It is a 2 μ event which was found in module 68B and is shown in figure A.7. There are 8 shower and 9 black tracks at the primary vertex which is downstream of plate 31. One of the shower tracks shows kink decay topology at downstream side plate 25. The daughter is μ^+ with a momentum 2.6 GeV/c reconstructed at muon spectrometer. The kink angle and the flight length are measured as 120 mrad and 4865 μm respectively. The P_T is 504 MeV/c. This value of P_T exclude the possibility of strange particle and pion decay topologies whose maximum P_T 's are less than 504 MeV/c. Therefore the most probable interpretation for this event is

$$\begin{aligned}\nu_\mu N &\rightarrow \mu^- D^+ X \\ D^+ &\rightarrow \mu^+ \nu_\mu \bar{K}^0 \text{ or} \\ D^+ &\rightarrow \mu^+ \nu_\mu\end{aligned}$$

If we assume these topologies we can roughly estimate life time of D^+ as $t \sim 1.95 \times 10^{-12} s$.

Table A.1: Kink decay Topology of K^+ , π^+ and D^+ and corresponding Branching ratios and maximum transverse momentum.

Kink topology	Branching ratio	Maximum P_T(MeV/c)
$K^+ \rightarrow \mu^+ \nu_\mu$	63.5%	236
$K^+ \rightarrow \pi^0 \mu^+ \nu_\mu$	3.8%	215
$\pi^+ \rightarrow \mu^+ \nu_\mu$	99.98 %	30
$D^+ \rightarrow \mu^+ \nu_\mu \bar{K}^0$	7.0 %	868
$D^+ \rightarrow \mu^+ \nu_\mu$	$< 7.2 \times 10^{-4}$	932

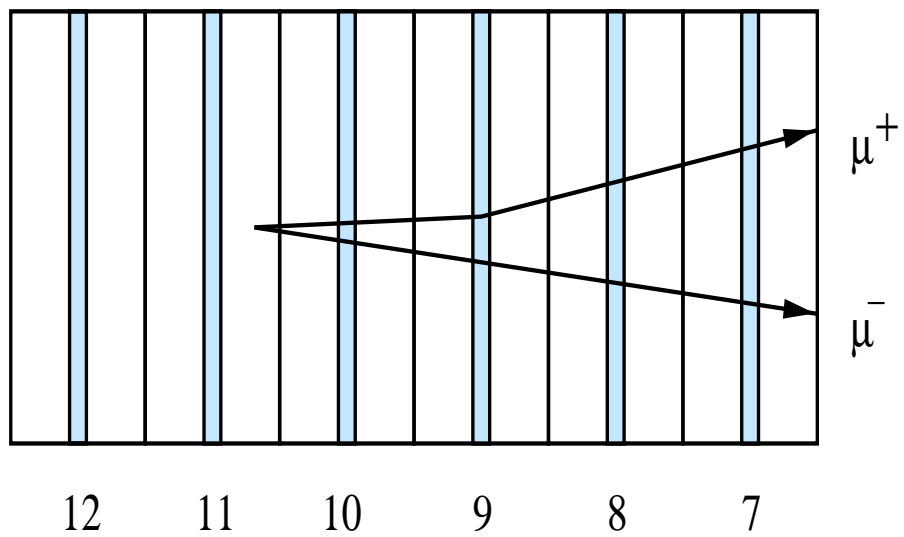
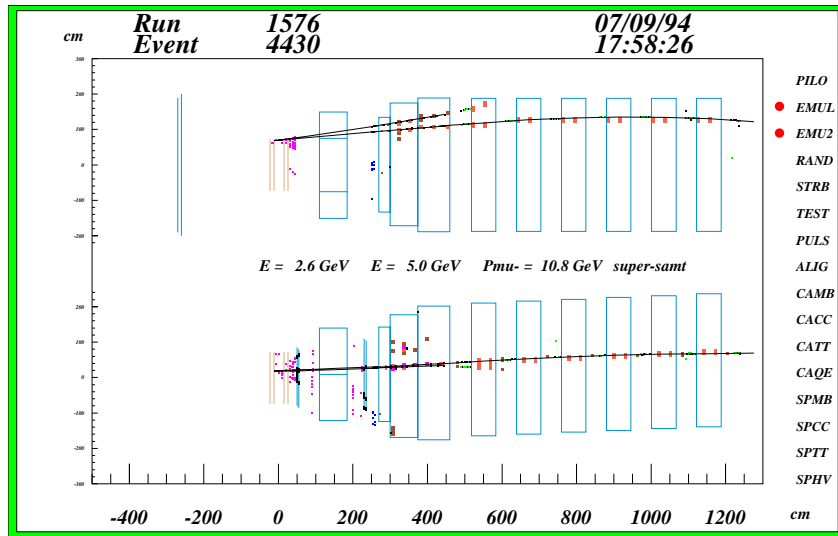


Figure A.1: Event 15764430, Kink Topology

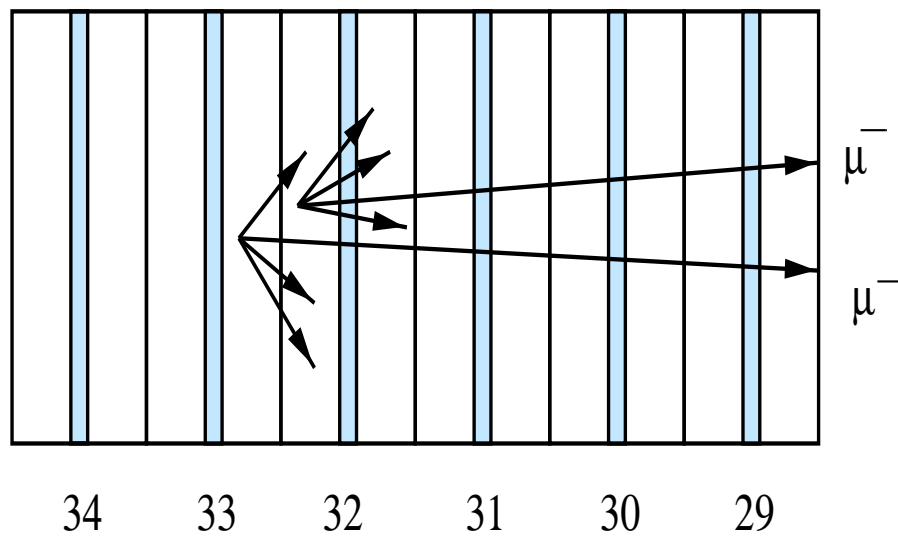
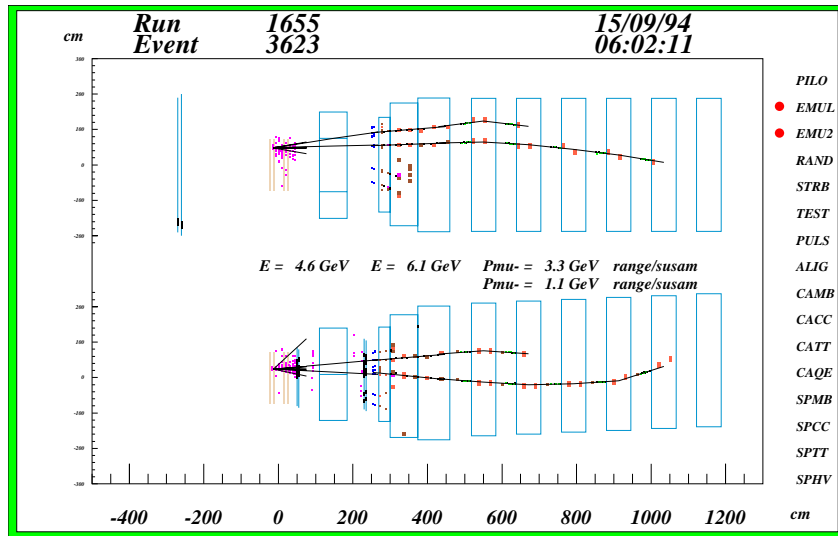


Figure A.2: Event 16553623, 4Vee Topology

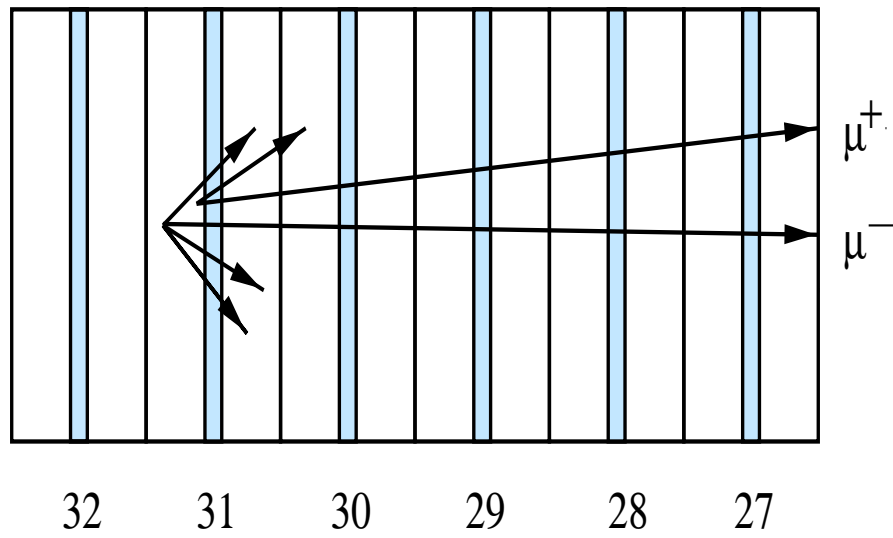
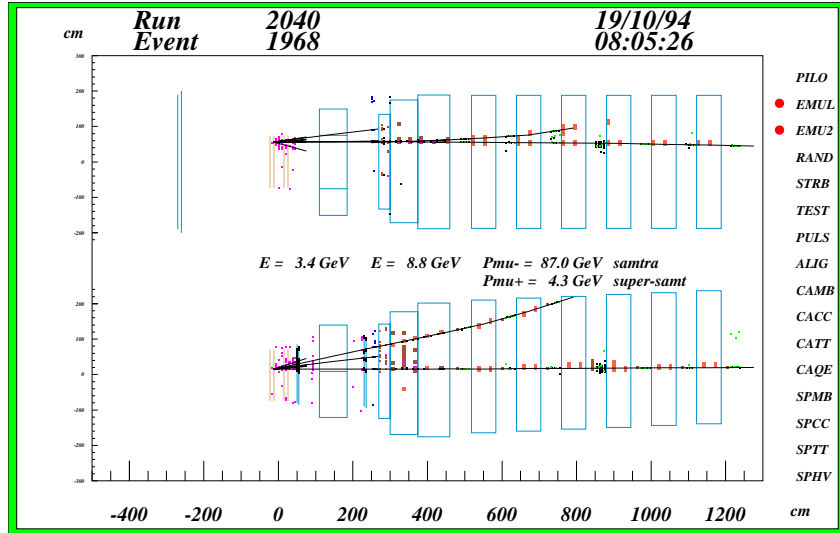


Figure A.3: Event 20401968, Vee Topology

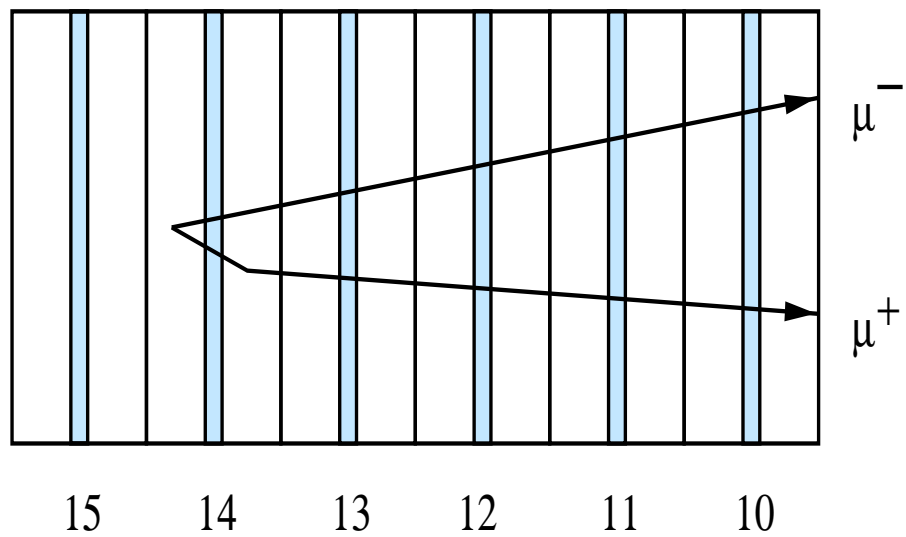
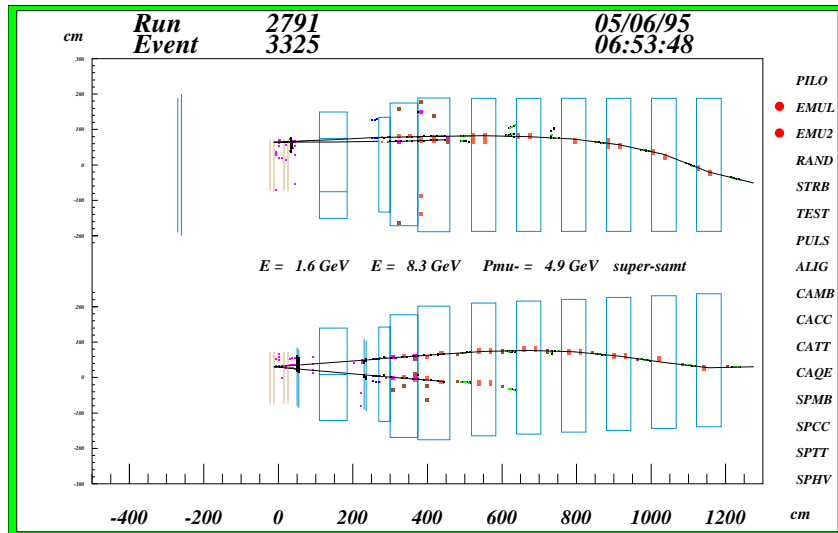


Figure A.4: Event 27913325, Kink Topology

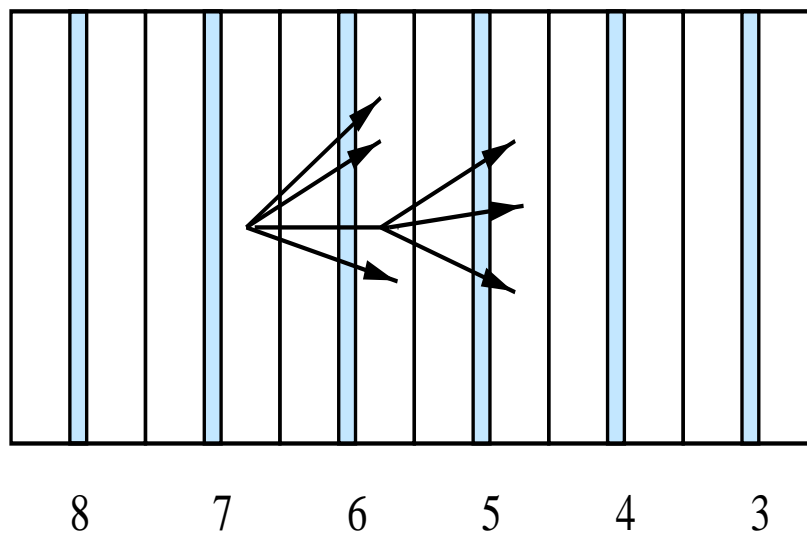
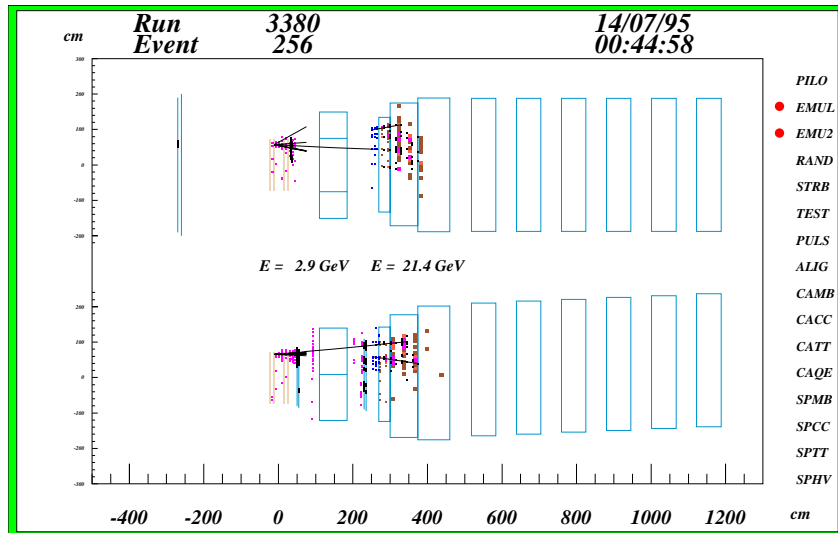


Figure A.5: Event 33800256, Trident Topology

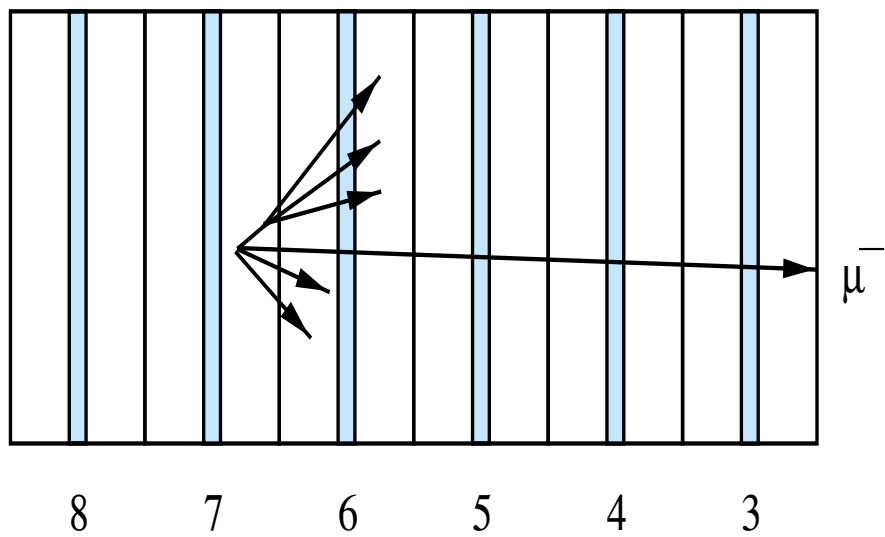
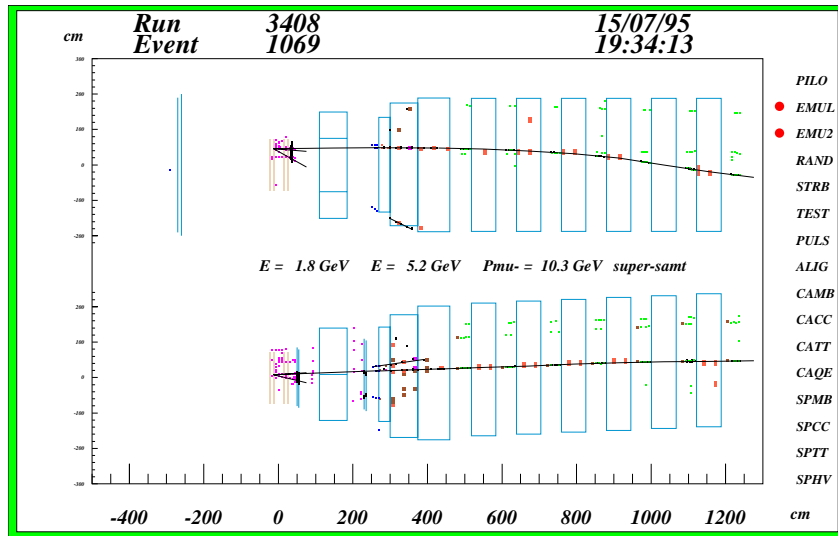


Figure A.6: Event 34081069, Trident Topology

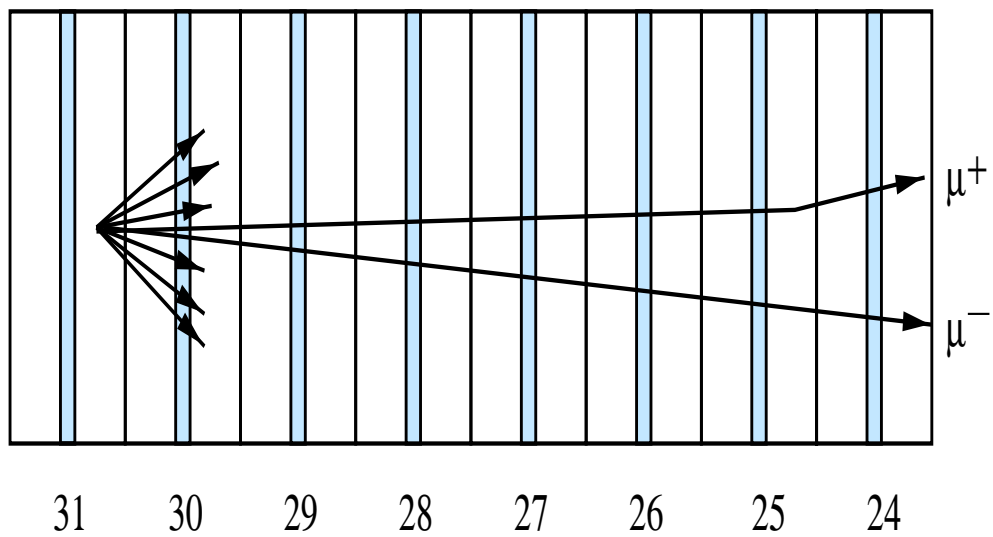
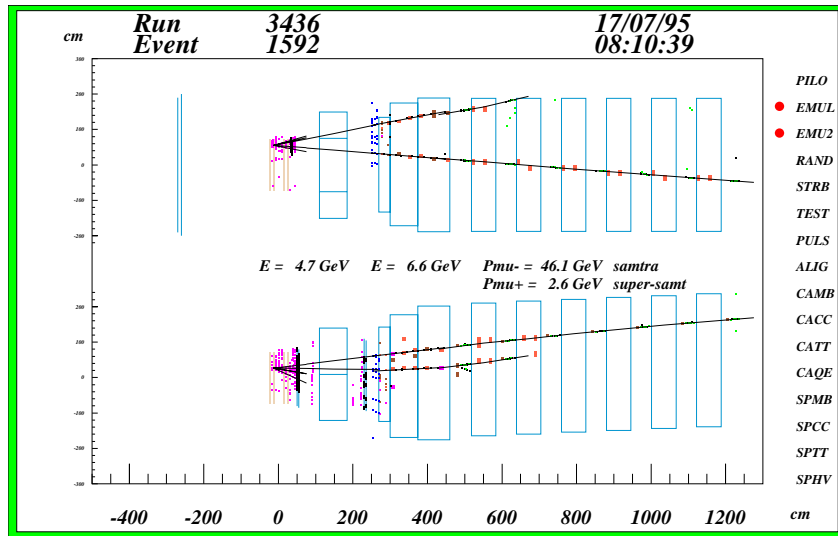


Figure A.7: Event 34361069, Kink Topology